The Astrophysical Journal, 937:116 (37pp), 2022 October 1 https://doi.org/10.3847/1538-4357/ac88cd

Comprehensive Analysis of the Neutrino Process in Core-collapsing Supernovae

Heamin Ko[1], Dukjae Jang[2], Myung-Ki Cheoun[1,3,4], Motohiko Kusakabe[3,4], Hirokazu Sasaki[4,5,6], Xingqun Yao[3], Toshitaka Kajino[3,4,5], Takehito Hayakawa[7,8], Masaomi Ono[9], Toshihiko Kawano[6], and Grant J. Mathews[3,4,10]
[1] Department of Physics and OMEG Institute, Soongsil University, Seoul 07040, Republic of Korea; cheoun@ssu.ac.kr
[2] Center for Relativistic Laser Science, Institute for Basic Science (IBS), Gwangju 61005, Republic of Korea
[3] School of Physics and International Research Center for Big-Bang Cosmology and Element Genesis, Beihang University, Beijing 100083, People's Republic of China
[4] National Astronomical Observatory of Japan, Mitaka, Tokyo 181-8588, Japan
[5] Graduate School of Science, The University of Tokyo, Bunkyo-ku, Tokyo 113-0033, Japan
[6] Theoretical Division, Los Alamos National Laboratory, Los Alamos, NM 87545, USA
[7] National Institutes for Quantum and Radiological Science and Technology, 2-4 Shirakata, Tokai, Naka, Ibaraki 319-1106, Japan
[8] Institute of Laser Engineering, Osaka University, Suita, Osaka 565-0871, Japan
[9] Kyushu University, Hakozaki, Fukuoka 812-8581, Japan
[10] Department of Physics, Center for Astrophysics, University of Notre Dame, Notre Dame, IN 46556, USA
Received 2022 April 24; revised 2022 August 5; accepted 2022 August 9; published 2022 October 4

Abstract

We investigate the neutrino flavor change effects due to neutrino self-interaction and shock wave propagation, as well as the matter effects on the neutrino process in core-collapsing supernovae (CCSNe). For the hydrodynamics, we use two models: a simple thermal bomb model and a specified hydrodynamics model for SN1987A. For the presupernova model, we take an updated model, adjusted to explain SN1987A, which employs recent developments in the (n, γ) reaction rates for nuclei near the stability line ($A \sim 100$). As for the neutrino luminosity, we adopt two different models: equivalent neutrino luminosity and nonequivalent luminosity models. The latter is taken from a synthetic analysis of CCSN simulation data, which quantitatively presented the results obtained by various neutrino transport models. Relevant neutrino-induced reaction rates are calculated using a shell model for light nuclei and a quasiparticle random phase approximation model for heavy nuclei. For each model, we present abundances of the light nuclei (^{7}Li, ^{7}Be, ^{11}B, and ^{11}C) and the heavy nuclei (^{92}Nb, ^{98}Tc, ^{138}La, and ^{180}Ta) produced by the neutrino process. The light nuclei abundances turn out to be sensitive to the Mikheyev–Smirnov–Wolfenstein (MSW) region around O-Ne-Mg layer while the heavy nuclei are mainly produced prior to the MSW region. Through detailed analyses, we find that neutrino self-interaction becomes a key ingredient, in addition to the MSW effect, for understanding the neutrino process and the relevant nuclear abundances. The normal mass hierarchy is shown to be more compatible with the meteorite data. The main nuclear reactions for each nucleus are also investigated in detail.

Unified Astronomy Thesaurus concepts: Supernova neutrinos (1666); Neutrino oscillations (1104); Explosive nucleosynthesis (503); Neutrino masses (1102); Core-collapse supernovae (304)

1. Introduction

The observation of a supernova (SN) in 1987 (SN1987A) has been considered as the brightest SN to be seen with naked eyes at the closest distance from the Earth. A few hours before the optical observation, the SN was predicted by the detection of neutrinos, which is the first record of neutrino detection from extrasolar objects (Schaeffer et al. 1987). The Kamiokande and Irvine–Michigan–Brookhaven detectors measured 8–11 neutrino events with Cherenkov detectors (Bionta et al. 1987; Hirata et al. 1987), while the Mont Blanc Underground Neutrino Observatory found five events from the neutrino burst using a liquid scintillation detector (Aglietta et al. 1987). The detection made it possible to point out that the location of the SN1987A event was in our satellite galaxy, the Large Magellanic Cloud.

Ever since SN1987A was observed, the explosion mechanism in massive stars has been extensively studied (Janka 2012). The development of simulations for SN1987A enabled evaluations of the SN mass and light curve (Woosley 1988; Shigeyama & Nomoto 1990), and various presupernova (pre-SN) models and explosive nucleosynthesis have subsequently been investigated (Hashimoto 1995). In particular, using the neutrino detections from core-collapsing SNe (CCSNe), the neutrino process (ν-process) in explosive nucleosynthesis has been considered to trace the origins of several elements that remain unexplained by traditional nuclear processes (Woosley et al. 1990; Kajino et al. 2014). Table 1 tabulates the nuclides that are thought to be produced mainly in the ν-process, which we closely examine in this paper.

In general, it is known that the heavy elements within $70 \lesssim A \lesssim 209$ are produced by the rapid neutron capture process (r-process; Burbidge et al. 1957; Kajino et al. 2014). However, since the heavy elements in Table 1 are surrounded by stable nuclei in the nuclear chart, they are blocked by the relevant nuclear reactions, such as neutron capture or $\beta^{\pm}$ decay. Consequently, the origins of those nuclei cannot be sufficiently explained by the r-process. However, the stable nuclei in Table 1 exist in our solar system, being contained in primitive meteorites (Lodders et al. 2009). For example, the existence of the short-lived unstable isotope ^{92}Nb in the solar system's formation has been verified from the isotropic anomaly in ^{92}Zr,

Table 1
The Main Elements Produced by the ν-process and Related References

Element	Related References
^{7}Li	(Woosley et al. 1990), (Yoshida et al. 2004), (Yoshida et al. 2005), (Yoshida et al. 2006), (Yoshida et al. 2008), (Suzuki & Kajino 2013), (Kusakabe et al. 2019)
^{11}B	(Woosley et al. 1990), (Yoshida et al. 2004), (Yoshida et al. 2005), (Yoshida et al. 2006), (Yoshida et al. 2008), (Nakamura et al. 2010), (Austin et al. 2011), (Suzuki & Kajino 2013), (Kusakabe et al. 2019)
^{19}F	(Woosley et al. 1990), (Sieverding et al. 2018), (Olive & Vangioni 2019)
^{93}Nb	(Hayakawa et al. 2013)
^{98}Tc	(Hayakawa et al. 2018)
^{138}La	(Woosley et al. 1990), (Sieverding et al. 2018), (Heger et al. 2005),(Hayakawa et al. 2008), (Byelikov et al. 2007), (Rauscher et al. 2013), (Kajino et al. 2014), (Kheswa et al. 2015) (Lahkar et al. 2017)
^{180}Ta	(Woosley et al. 1990), (Heger et al. 2005), (Byelikov et al. 2007), (Hayakawa et al. 2010), (Rauscher et al. 2013), (Kajino et al. 2014) (Lahkar et al. 2017), (Malatji et al. 2019)

to which ^{92}Nb decays (Harper 1996; Münker et al. 2000; Sanloup et al. 2000; Haba et al. 2021). To explain the meteorite data, another production mechanism for the nuclides—such as the ν-process—has been necessary. In the study of the ν-process, neutrino properties and stellar environments play vital roles in determining the neutrino oscillation behavior, which is critical for studying the process, as argued below.

First, neutrino mixing parameters, such as squared mass differences and mixing angles, significantly affect the neutrino oscillation in CCSN environments. The neutrino oscillation experiments do not measure the absolute masses of neutrinos, but the squared mass differences defined by Δm_{ij}^2, where i, $j = 1$, 2, and 3 in the mass eigenstates. Also, the mixing angles of θ_{12}, θ_{23}, and θ_{13}, which are deeply related to the neutrino oscillation behavior, have been measured by various experiments (Olive & Particle Data Group 2014). However, in spite of the challenging experiments, the problem regarding the neutrino mass hierarchy (MH) has remained unsolved. Although it has been reported that the inverted hierarchy (IH) is disfavored, with a 93% confidence level (NOνA Collaboration et al. 2017), precise verification as to whether the neutrino mass follows the normal hierarchy (NH; $m_1 < m_2 < m_3$) or the IH ($m_3 < m_1 < m_2$) is still required.

Second, during a CCSN explosion, neutrinos pass through matter composed of protons, neutrons, charged leptons, neutrinos, and nuclides. In the propagation, the neutrinos scatter with the background particles through the weak interaction (Nötzold & Raffelt 1988) resulting from the charged-current (CC) and neutral-current (NC) interactions. Since both interactions would affect the time evolution of the neutrino flavors, the neutrino oscillation behavior differs from the case in free space. The effective potential describing the interaction of the propagating neutrinos depends on the matter density, so that the hydrodynamics models become important in the CCSN ν-process. In this paper, we compare the results of the ν-process from two different hydrodynamics models, and discuss how the models change the behavior of the neutrino oscillation and affect the nucleosynthesis.

Third, the neutrino emission mechanism in the CCSN significantly impacts on the neutrino flux. The neutrinos in the CCSN are trapped for a few seconds, until the dynamical timescale of the core collapse becomes longer than the neutrino diffusion timescale (Janka 2017). After this trapping, the explosion generates the emission of a huge number of neutrinos. Near the proto-neutron star, due to the emitted high-density neutrino gas, the self-interaction (SI) among the neutrinos should be considered (Pantaleone 1992; Samuel 1993; Sigl & Raffelt 1993; Qian & Fuller 1995; Fuller & Qian 2006; Duan et al. 2006). By the SI, the neutrino flux in the CCSN could be changed, and would impact on the ν-process (Ko et al. 2020), as well as the νp-process (Sasaki et al. 2017), and also the neutrino signals from the CCSN (Wu et al. 2015). Such a collective neutrino flavor conversion derived from the neutrino's SI (ν-SI) is distinct from the conventional neutrino-matter effects, in that the background neutrinos provide a nonlinear contribution, due to the mixed neutrino states represented by an off-diagonal term. The SI effects can be suppressed when the electron background is more dominant than the neutrino background near the proto-neutron star (Dasgupta et al. 2010; Chakraborty et al. 2011; Duan & Friedland 2011). This suppression depends on the neutrino decoupling model (Abbar et al. 2019).

Finally, one of the main concerns in the neutrino physics for CCSNe is the shape of the statistical distribution of the neutrinos. During the neutrino decoupling from a proto-neutron star, various collision processes—such as neutrino elastic scattering on nucleons ($\nu N - N\nu$), nucleon–nucleon bremsstrahlung (NN–$NN\nu\bar{\nu}$), and leptonic processes ($\nu e - e\nu$, $e^+e^- - \nu\bar{\nu}$)—result in the neutrino spectra deviating from the Fermi–Dirac (FD) distribution (Raffelt 2001; Keil et al. 2003). Because muon-type and tau-type neutrinos (ν_μ and ν_τ) only interact through the NC interaction, being weaker than CC interactions, they are decoupled earlier than electron-type neutrinos (ν_e), and consequently they have different temperatures. The decoupling temperature and the neutrino distribution function are also crucial to determining their flux, which affects the neutrino-induced reaction rates. In principle, the exact decoupling process should be investigated by the neutrino transport equation, because it has significant effects on the CCSN ν-process and the CCSN explosion. As a cornerstone, O'Connor et al. (2018) showed the consistent agreement of the results from six different neutrino transport models for an SN simulation. As a further step, we expect that multidimensional neutrino transport simulations will be performed in the near future.

Based on the neutrino properties and related explosion models, the CCSN ν-process has been investigated in detail. Furthermore, by comparing the calculated results with the observed solar abundance, one may find the contribution of the SN ν-process to the solar system material. For instance, it is known that the stable nuclides, such as ^{7}Li and ^{11}B, are meaningfully produced by the ν-process, while ^{6}Li and ^{10}B are produced in insignificant amounts (Fields et al. 2000; Mathews et al. 2012). For a short-lived unstable nuclide such as ^{98}Tc, one can use the estimated abundance as a cosmic chronometer

to predict the epoch when SNe flow in our solar system (Hayakawa et al. 2013, 2018). Besides, a comparison between the estimated abundances and the observed meteoritic data may provide a clue to the neutrino temperature in the CCSN explosion (Yoshida et al. 2005).

In this paper, we investigate how the CCSN ν-process is affected by the various neutrino properties and CCSN models that are currently available, and we discuss some questions remaining about the CCSN ν-process and future works. For this purpose, we organize this paper as follows. In Section 2, we explain the effects of different SN hydrodynamics models on the CCSN ν-process. After establishing the hydrodynamics models, in Section 3 we review the neutrino oscillation features in the CCSN environment. Section 4 covers the formulae of the nuclear reaction rates for the nucleosynthesis in the CCSN explosion. The results of the synthesized elements are presented in Section 5. Finally, a discussion and summary are presented in Section 6. Detailed formulae for the calculations, and numerical results of some updated nuclear reactions, are summarized in Appendices A, B, and C, respectively. Each of the contributions of the main nuclear reactions to each nuclear abundance are provided in detail in Appendix D. All of the equations in this paper follow the natural units, i.e., $\hbar = c = 1$.

2. Neutrino Oscillation in CCSNe

In the CCSN explosion, the propagating neutrinos interact with the leptonic background through CC or NC reactions. Although various lepton components are interacting with neutrinos in CCSN environments, because of their too-high threshold energies or small numbers of background leptons, only the net electron composed of electrons and positrons—as a background component—contributes to the neutrino oscillation through the CC reaction. Hence, we consider the matter effect only with varying electron density, which is known as the Mikheyev–Smirnov–Wolfenstein (MSW) effect (Mikheev & Smirnov 1986). When dealing with the electron density as the background, which of the hydrodynamics models of SN explosion that we choose is important. In this section, using two kinds of SN hydrodynamics models, we discuss the MSW effects on the neutrino oscillation in CCSN environments.

2.1. The MSW Effect in SN1987A

The typical CCSN environment constrains the particle momenta scale within the MeV range, while the gauge bosons in the standard weak interaction have masses of 100 GeV scale mass. Because of the low-energy environments, we treat the weak interaction of the neutrinos with a point-like coupling scheme. By taking the thermal average of the electron background and the charge neutrality condition, we obtain the following total Hamiltonian for CC interaction, which is decomposed into the vacuum term and the MSW matter potential:

$$\begin{aligned} H_{\rm total} &= H_{\rm vacuum} + \mathcal{V}_{\nu_e e} \\ &= U\,{\rm diag}\left(0, \frac{\Delta m^2_{21}}{2E_\nu}, \frac{|\Delta m^2_{31}|}{2E_\nu}\right)U^\dagger \\ &\quad + {\rm diag}(\sqrt{2}\,G_F n_e, 0, 0), \end{aligned} \tag{1}$$

where U is the Pontecorvo–Maki–Nakagawa–Sakata unitary mixing matrix, the values of Δm^2_{ij} are adopted from the Olive & Particle Data Group (2014), and E_ν denotes the neutrino energy. n_e stands for the net electron density. The detailed derivation of the Hamiltonian is succinctly summarized in Appendix A. Note that the effective potential for the NC interactions contributing to all flavors is not included in the matter Hamiltonian, because it is absorbed into a phase shift (Giunti & Chung 2007). By solving the Schrödinger-like equation with the total Hamiltonian, we obtain the neutrino flavor change probability. As seen in the Hamiltonian, the neutrino oscillation probability depends on n_e, which implies the importance of the chosen hydrodynamics models. In the next subsection, we introduce two kinds of hydrodynamics models to describe the time evolution of the neutrino flavors.

2.1.1. Profiles of the SN1987A Model

SN1987A has been verified as an explosion of a blue supergiant star, Sk–69 202, in the Large Magellanic Cloud, which has been estimated to have had a (19 ± 3) solar mass ($M_\odot$) in the main sequence, following the analysis of the light curve, with the metallicity being given as $Z \sim Z_\odot/4$ (Woosley 1988). Among the various explosive models satisfying the given conditions (Janka 2012), for the pre-SN model we adopt the initial density and temperature profiles from Kikuchi et al. (2015), whose results are similar to those of Shigeyama & Nomoto (1990). For the hydrodynamics models, we exploit the model in Kusakabe et al. (2019), based on the blcode,[11] with an explosion energy of 10^{51} erg. To discuss the effects of the hydrodynamics models, we introduce another model, used in Hayakawa et al. (2018), which was gleaned from the pre-SN model of Blinnikov et al. (2000), and has also been used in Hayakawa et al. (2013; 2018), and Ko et al. (2020). We call the former and latter models the "KCK19" (Kusakabe et al. 2019) and "HKC18" (Blinnikov et al. 2000) models, respectively. The HKC18 model turns out to have an inconsistency with the adopted pre-SN model. A detailed explanation of this inconsistency between the hydrodynamics model and pre-SN model is given in Section 5.

In the Lagrange mass coordinate, Figures 1, 2, and 3 show the results of the time-evolving density, temperature, and radius, from about 0 to 7 s, respectively, for the two different hydrodynamics models. The upper and lower panels of the figures illustrate the results for the HKC18 model and the KCK19 model, respectively. The different evolutions of the density affect the neutrino oscillation probability through the change of the effective potential in $\mathcal{V}_{\nu_e e}$. Also, the change of temperature is deeply involved with the thermonuclear reaction rates affecting the explosive nucleosynthesis, as explained in Sections 4 and 5.

2.1.2. Neutrino Flavor Change Probability

For the given density profile, we solve the Schrödinger-like equation with the total Hamiltonian in Equation (1). As a result, we obtain the neutrino flavor change probability from α to β, denoted by $P_{\alpha\beta}$, in CCSN environments. Figure 4 shows the survival probability of ν_e and $\bar{\nu}_e$ at $t = 0$ as a function of the Lagrange mass coordinate for $E_\nu = 15$ MeV. The four panels show that the $P_{\alpha\beta}$ depends on the neutrino MH and the hydrodynamics model. The differences between the

[11] https://stellarcollapse.org/index.php/SNEC.html

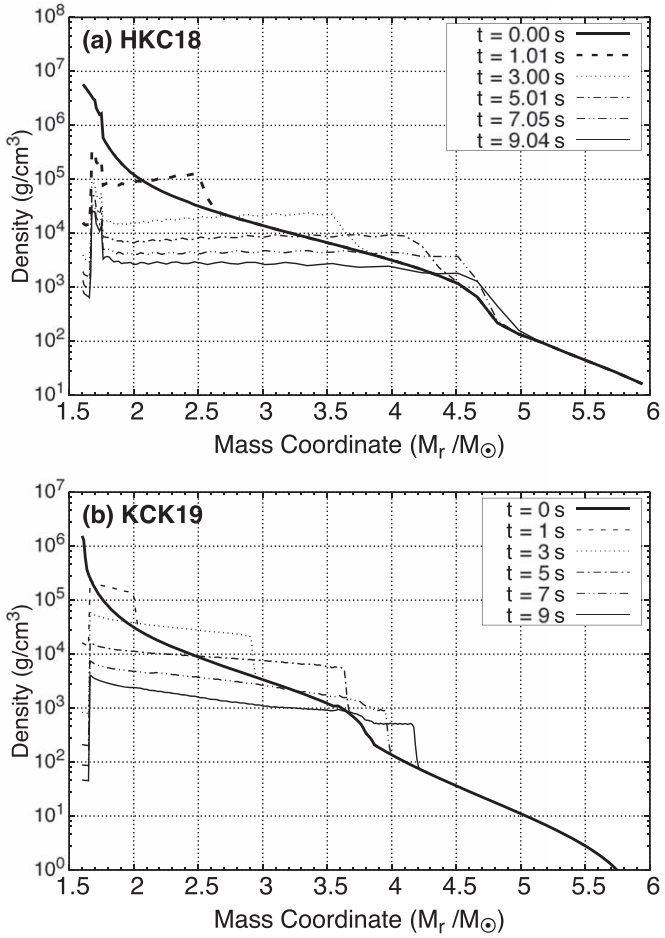

Figure 1. Time-evolving density profiles in the Lagrange mass coordinate. The upper and lower panels show the HKC18 (Blinnikov et al. 2000) and KCK19 (Kusakabe et al. 2019) hydrodynamics models, respectively. The time range is taken from about 0 to 7 s.

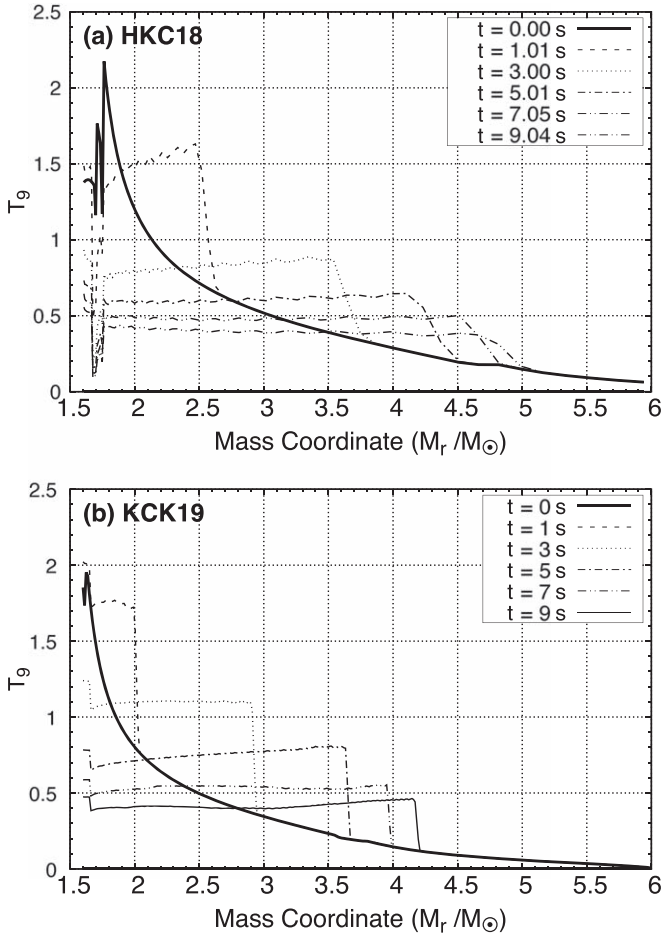

Figure 2. Time-evolving temperature profiles as a function of the Lagrange mass coordinate. The upper and lower panels show the same models as in Figure 1, respectively. The temperature unit is taken as $T_9 = T/(10^9\ \mathrm{K})$.

hydrodynamics models are shown in the left and right panels, while those between the MH are distinguished by the top and bottom panels.

In all the panels of Figure 4, there are regions where the neutrino flavor probability changes drastically. During the neutrino propagation from the neutrino sphere, as the matter density decreases, the value of the vacuum oscillation term becomes comparable to the matter potential term in a specific region. As a result, the maximal neutrino flavor change is induced, which is called the MSW resonance. Specifically, when the vacuum term is the same as the matter potential term, i.e., $\sqrt{2}\,G_F n_e = \cos 2\theta \Delta m^2/(2E_\nu)$, the MSW resonance occurs at the density

$$\rho_{res} = \frac{\cos 2\theta_{ij} |\Delta m^2_{ji}|}{2\sqrt{2}\,G_F Y_e E_\nu N_A}. \quad (2)$$

Here, we approximately take the electron fraction as $Y_e = 0.5$.

If we compare the left and right panels in Figure 4, we can note that the resonance region depends on the hydrodynamics model. The left panels, adopting the HKC18 model, indicate the resonance region as $M_r \sim 4.6 M_\odot$, while the right panels, for the KCK19 model, indicate a different resonance region, at $M_r \sim 3.7 M_\odot$. This is because the density satisfying the resonance ($\sim 10^3\ \mathrm{g\,cm^{-3}}$) appears in different regions (see Figure 1).

The upper and lower panels of Figure 4 show the different resonance patterns due to the neutrino MH. The difference stems from the value of the density-dependent Δm^2_{31} involved in the resonance density. As a result, for the NH case, the resonance leads the average of the initial ν_μ and ν_τ spectra to the final spectra of ν_e. On the other hand, for the IH case, the resonance of the antineutrinos occurring on the inner side drives the average of the initial $\bar{\nu}_\mu$ and $\bar{\nu}_\tau$ spectra to be the final spectra of $\bar{\nu}_e$.

2.2. The Shock Wave Propagation Effect

Another noteworthy point is that the temperature and density are increased when the shock passes the stellar region. The shock propagation drastically changes the density in a specific region and time, which is related to the matter Hamiltonian. However, in the adiabatic approximation that is usually adopted in quantum mechanics, quantum states gradually vary if the external conditions act slowly enough. Therefore, we should weigh the adiabatic condition for the neutrino oscillation—to verify whether the quantum states of the neutrinos react to the drastic change of the background by the shock propagation or not.

For the time evolution of the neutrino flavors, if the energy gap between mass eigenstates is given as ΔE, it would satisfy

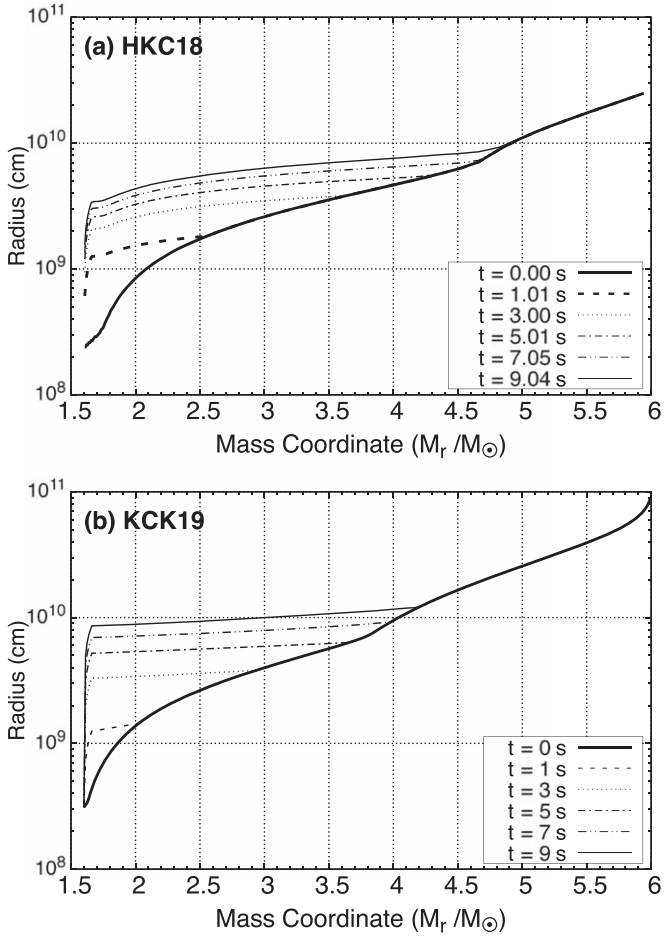

Figure 3. Time-evolving radius profiles as a function of the Lagrange mass coordinate. The upper and lower panels show the same models as in Figure 1, respectively.

the following condition:

$$\Delta E \times \Delta t \ll \hbar, \tag{3}$$

where $\Delta t = \Delta r = \frac{\delta n_e}{n_e}(n_e / \frac{dn_e}{dr})$ is the time gap for the transition. Figure 5 shows the eigenstates for 15 MeV neutrino energy. In the adiabatic process, the diagonalized states are gradually changed and the resonance occurs when the mass eigenvalues of each state are close to each other, while a rapid external variation, such as a shock, can make the transition between the states a nonadiabatic process.

The flip probability for the linear density case is given as (Dighe & Smirnov 2000)

$$P_f = \exp\left(-\frac{\pi}{2}\gamma\right), \tag{4}$$

where the adiabatic parameter γ is defined as (Kuo & Pantaleone 1989)

$$\gamma = \frac{\Delta m_{ij}^2}{2E_\nu}\frac{\sin^2 2\theta_{ij}}{\cos 2\theta_{ij}}\frac{n_e}{dn_e/dr}. \tag{5}$$

For $\gamma \gg 1$, P_f goes to zero, indicating that there is no transition between eigenstates, which corresponds to the adiabatic condition. On the other hand, for $\gamma \lesssim 1$, we expect a considerable flip probability, which implies a nonadiabatic condition.

We investigate the flavor change probabilities for the three active neutrino flavors from the shock propagation effect. It was found that the first resonance occurs at $M_r \sim 1.6 M_\odot$, owing to shock propagation. The resonance pattern is distinct from that shown in Figure 4. The adiabatic parameter has a value of $\gamma \approx 1.63 - 4.8$ at the resonance region, where the flip probability is approximately evaluated as 8×10^{-2}–5×10^{-4}.

Within the shock propagation effect, snapshots of the flavor change probabilities are shown in Figure 6. Starting with the first resonance at $M_r \simeq 1.65\ M_\odot$, the next resonance occurs at the region of $M_r \simeq 3.3\ M_\odot$. Due to the second resonance, the ν_e energy spectra return to the initial flux. After that, the last resonance appears at $M_r \sim 4.7 M_\odot$. The multiple resonances from the shock propagation change the neutrino flux and affect the yields of the ν-process. We discuss the yields of the nucleosynthesis, including the shock effect, in Section 5.

3. Neutrino SI

Near the neutrino sphere, the neutrinos trapped by dense matter formed via gravitational collapse stream violently, so that the neutrino number densities are high enough for their SI during emission to be considered (Janka et al. 2007). The considerable neutrino background causes the NC interaction to be comparable to the vacuum or electron matter potential for all neutrino flavors (Sigl & Raffelt 1993; Duan et al. 2006, 2011). The Hamiltonian density for the neutrino–neutrino interaction is written as (Pantaleone 1992; Samuel 1993)

$$\mathcal{H}_{\nu\nu}^{\rm NC}(x) = \frac{G_F}{\sqrt{2}}\sum_{\alpha,\beta,\gamma,\eta}(\delta_{\alpha\gamma}\delta_{\beta\eta} + \delta_{\alpha\eta}\delta_{\beta\gamma}(1 - \delta_{\alpha\beta})) \times [\bar{\nu}_{\gamma L}(x)\gamma^\mu \nu_{\alpha L}(x)][\bar{\nu}_{\eta L}(x)\gamma^\mu \nu_{\beta L}(x)], \tag{6}$$

where δ denotes the Kronecker delta describing the diagonal and momentum exchange interactions in Figure 7(a), and its subindexes of α, β, γ, and η stand for the neutrino flavors. By adopting the mean-field approximation to the background neutrinos, we obtain the following background potential with three momenta $\boldsymbol{q}$ (See Appendix B):

$$\hat{\mathcal{V}}_{\nu\nu} = \sqrt{2}G_F\frac{1}{V}\sum_{\boldsymbol{pq}}\frac{[a_{\nu_\beta}^\dagger(\boldsymbol{p})a_{\nu_\alpha}(\boldsymbol{p}) - b_{\nu_\alpha}^\dagger(\boldsymbol{p})b_{\nu_\beta}(\boldsymbol{p})]}{2E_p V} \times(1 - \hat{\boldsymbol{p}}\cdot\hat{\boldsymbol{q}})[f_{\rm dist}(t,\boldsymbol{q})\rho_{\beta\alpha}(t,\boldsymbol{q}) - \bar{f}_{\rm dist}(t,\boldsymbol{q})\bar{\rho}_{\beta\alpha}(t,\boldsymbol{q})], \tag{7}$$

where $\hat{\boldsymbol{p}}$ is the momentum direction of the propagating neutrino. The factor of $(1 - \hat{\boldsymbol{p}}\cdot\hat{\boldsymbol{q}})$ stems from the weak current interaction, which prevents the scattering in the same trajectory (Pehlivan et al. 2011). $f_{\rm dist}$ ($\bar{f}_{\rm dist}$) and $\hat{\rho}$ ($\bar{\rho}$) are the normalized distribution and the density matrix for neutrinos (antineutrinos), respectively.

Diagrams of the diagonal and exchange interactions giving rise to the potential are shown in Figure 7(b). The diagonal term, as a linear contribution, is related to the number density of the neutrinos. As an example, $f_{\rm dist}(t,\boldsymbol{q})\rho_{ee}(t,\boldsymbol{q})/V$ means the ν_e distribution being affected by the flavor change probability ρ_{ee}, whose summation over $\boldsymbol{q}$ leads to the number density of ν_e. In particular, the momentum exchange interactions, which act as the off-diagonal terms and are initially set to be zero, affect the neutrino flavor transformations. The dominant off-diagonal

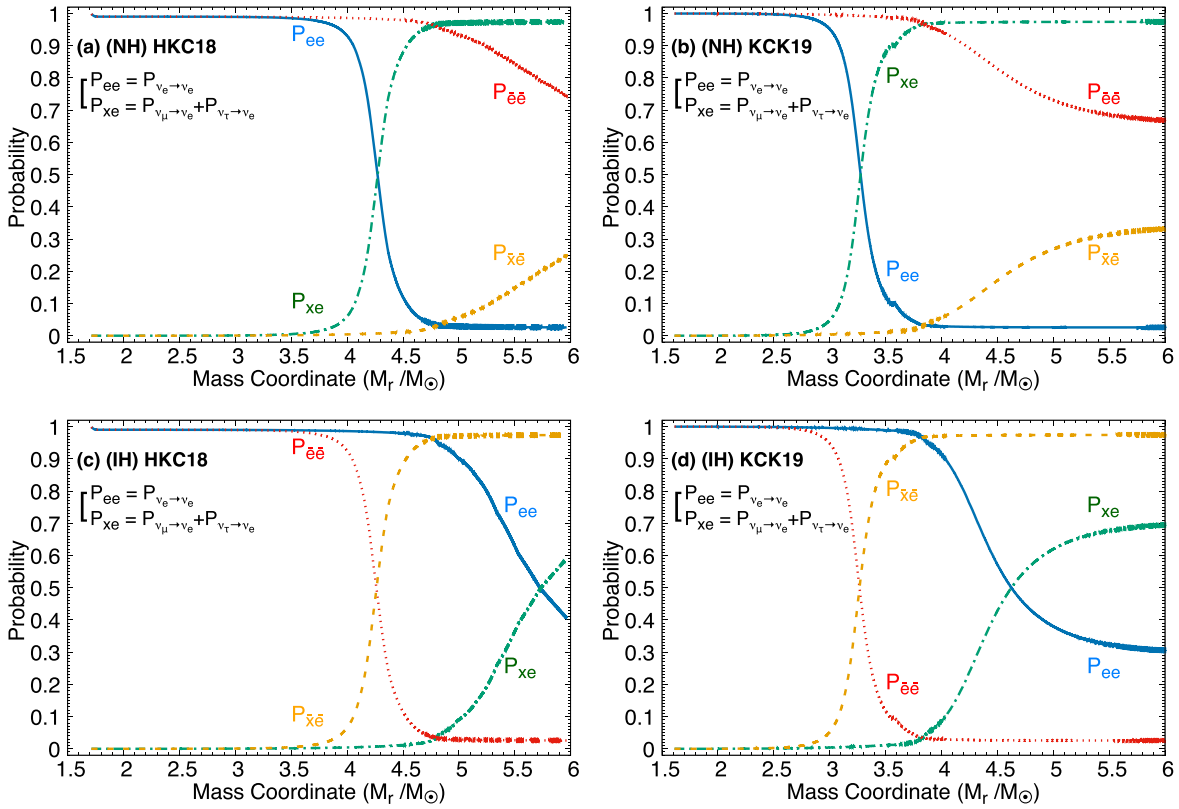

Figure 4. Flavor change probability for ν_e with neutrino energy $E_\nu = 15$ MeV, calculated at $t = 0$. The left and right panels adopt the HKC18 (Blinnikov et al. 2000) and KCK19 (Kusakabe et al. 2019) hydrodynamics models, respectively. The upper and lower panels correspond to the NH and IH, respectively.

potential, known as the Background Dominate Solution, was studied in Fuller & Qian (2006).

$\sum_{\boldsymbol{q}} f_{\rm dist}(t, \boldsymbol{q})/V$ in Equation (7) is the local neutrino number density denoted by $\int dn_\nu$. To determine the dn_ν, as a neutrino emission model, we adopt the neutrino bulb model (Duan et al. 2006), assuming a uniform and half-isotropic neutrino emission (Chakraborty et al. 2011), and obtain dn_ν as follows:

$$dn_{\nu_\eta} = \frac{1}{\pi R_\nu^2} \frac{L_{\nu_\eta}}{\langle E_{\nu_\eta}\rangle} f_{FD}(E_q, T_{\nu_\eta}) E_q^2 dE_q d\Omega_q, \tag{8}$$

where R_ν, L_{ν_η}, and $\langle E_{\nu_\eta}\rangle$ are the neutrino sphere radius, the neutrino luminosity, and the averaged neutrino energy for η flavor, respectively. We take the normalized distribution function of the neutrinos as the FD distribution with zero chemical potential, i.e., $f_{FD}(E_q, T_{\nu_\eta}) \equiv (4\pi T_{\nu_\eta}^3 F_2(0))^{-1} (\exp(E_q/T_{\nu_\eta}) + 1)^{-1}$, where $F_2(0)$ is 1.80309. The solid angle part is given by the z-axis symmetry as $\int (1 - \hat{\boldsymbol{p}} \cdot \hat{\boldsymbol{q}}) d\Omega_{\boldsymbol{q}} = 2\pi \int_0^\theta (1 - \cos\theta_p \cos\theta_q) \sin\theta_q d\theta_q$ (Appendix B). In the single-angle approximation, since θ_p is neglected, the integration of the angular term becomes $(1 - \cos\theta)^2/2$. The maximum θ is the tangential direction at the neutrino emission point and satisfies the relation of $\sin\theta_{\rm max} = R_\nu/r$. Although the single-angle approximation may be proper in the early universe, satisfying the isotropic and homogeneous conditions (Kostelecký & Samuel 1994), it is not enough to describe the decoupling of neutrinos near the SN core, as explained in Duan et al. (2011). Hence, in this study, we perform a multi-angle calculation involving the θ_p.

When we consider the broken azimuthal symmetry (Banerjee et al. 2011; Raffelt et al. 2013), the azimuthal angle (ϕ_q) dependent term is not negligible in the factor of $(1 - \hat{\boldsymbol{p}} \cdot \hat{\boldsymbol{q}})$. Therefore, in the accretion phase, the violation of the azimuthal symmetry results in multi-azimuthal angle instability (Chakraborty & Mirizzi 2014) and fast ν-flavor conversion (Abbar et al. 2019; see also Dasgupta et al. 2008 for the effects of nonspherical geometry). That is, such a realistic SN model brings about neutrino emission not predicted in the symmetric model.

However, the ν-process is more significantly affected by the neutrino cooling phase—occurring over a long neutrino emission time—rather than the burst and accretion phases, as explained in Section 3.2. Although the asymmetric models can also affect the neutrino cooling phase, there have not been appropriate models to apply to the ν-process. Moreover, the asymmetry requires the description of the ν-process by 3D hydrodynamics models, which is beyond the scope of the present study. Hence, we leave the effects of asymmetric neutrino emission on the ν-process to future work. As the CCSN model, we adopt a 1D spherical symmetric model with the multi-angle effect for the collective neutrino oscillation.

In setting up the model, we solve the following equations of motion for the neutrino density matrices with the three-flavor multi-angle calculation (Sasaki et al. 2017):

$$\cos\theta_p \frac{d}{dr}\rho(r, E_p, \theta_p) = -i[H_{\rm Vacuum} + \mathcal{V}_\nu,\ \rho(r, E_p, \theta_p)], \tag{9}$$

$$\cos\theta_p \frac{d}{dr}\bar{\rho}(r, E_p, \theta_p) = -i[-H_{\rm Vacuum} + \mathcal{V}_\nu,\ \bar{\rho}(r, E_p, \theta_p)], \tag{10}$$

$$\mathcal{V}_\nu = \mathcal{V}_{\nu_e e} + \mathcal{V}_{\nu\nu}, \tag{11}$$

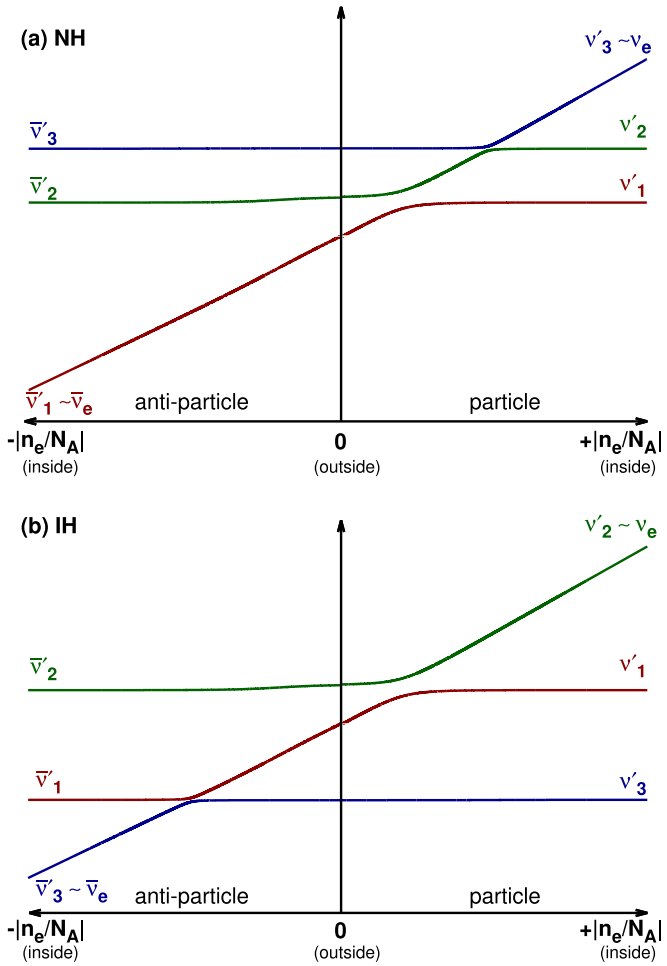

Figure 5. The eigenvalues of the matter states according to the electron number density per N_A for $E_\nu = 15$ MeV. The upper and lower panels show the results calculated in the NH and IH schemes, respectively.

where $H_{\rm Vacuum}$ and $\mathcal{V}_{\nu_e e}$ are the vacuum term and the MSW matter potential, respectively, in Equation (1), and $\mathcal{V}_{\nu\nu}$ is the potential for the neutrino SI (ν-SI) in Equation (B6).

The study of the collective neutrino oscillation requires the lepton density profiles from near the neutrino sphere to outside. For the baryon matter density, from $r = 10$ km to around 2000 km, we adopt the empirical parameterization of the shock density profile (Fogli et al. 2003). For $t > 1$ s, the density profile is given as

$$\rho_b(r, t) = 10 \times (10^{14}\,\mathrm{g\,cm^{-3}})\left(\frac{1\,\mathrm{km}}{r}\right)^{2.4} \times \exp\left[\left(0.28 - 0.69\ln\left(\frac{x_s}{1\,\mathrm{km}}\right)\right)\left(\sin^{-1}\left(1 - \frac{r}{x_s}\right)\right)^{1.1}\right], \quad (12)$$

where the shock front position is defined by $x_s(t) = x_s^0 + v_s t + 0.5 a_s t^2$, with $x_s^0 \simeq -4.6 \times 10^3$ km, $v_s \simeq 11.3 \times 10^3\,\mathrm{km\,s^{-1}}$, and $a_s \simeq 0.2 \times 10^3\,\mathrm{km\,s^{-2}}$. For $t \leqslant 1$ s, we use $\rho_b(r, t) = 10^{14}(\mathrm{g\,cm^{-3}})(1\,\mathrm{km}/r)^{2.4}$. The electron number density is given in the same way, i.e., $n_e(r, t) = \rho_b(r, t) Y_e N_A$.

Compared to the electron density, the neutrino number density obtained by the integration of Equation (8) relies not only on the radius, but also on the neutrino luminosity and averaged energy. Within the single-angle approximation without flavor mixing between the neutrinos, the neutrino density is given as follows (See Equation (B7)):

$$n_\nu(r) \approx (2\pi R_\nu^2)^{-1}(1 - \sqrt{1 - (R_\nu/r)^2})^2 \times [L_{\nu_e}/\langle E_{\nu_e}\rangle - L_{\bar\nu_e}\langle E_{\bar\nu_e}\rangle]. \quad (13)$$

Figure 8 shows the lepton and neutrino number densities estimated by the above equation, which are similar to the results in Duan et al. (2006). This figure implies that the n_ν and n_e are sufficient to consider the ν-SI. Furthermore, the valuable change of the neutrino flux by the SI would affect the ν-process. Here, we note that the density hinges on the SN simulation model. For example, Chakraborty et al. (2011) exploited the SN simulation of Fischer et al. (2010), where the neutrino sphere blows up to about 100 km during the accretion phase and drops to about 30 km at the cooling phase. Consequently, the neutrino flux is much smaller than the present case, where the neutrino sphere is assumed to be about 10 km. Moreover, the electron density in Chakraborty et al. (2011) is larger than that evaluated by Fogli et al. (2003) adopted in this calculation. In this perspective, the small neutrino sphere radius of ∼10 km and the simple fast-decreasing power-law density profile proportional to $r^{-2.4}$ in the present work may not be compatible with those typically seen during the accretion phase of SN simulations. A smaller neutrino density and a higher electron density than in the present work may lead to the suppression of the neutrino collective motion during the accretion phase in the SN simulations. The relevant uncertainty during the accretion phase is discussed quantitatively in the conclusion.

To determine the neutrino number density with SI effects, we study two kinds of neutrino luminosities and averaged energies. The first one is flavor-independent neutrino luminosity, i.e., each neutrino has an equivalent luminosity. In this model, with the FD distribution, the averaged energy is determined by $\langle E_\nu\rangle = 3.1514\,T_\nu$, and we take the temperatures constrained from the ^{11}B abundance (Yoshida et al. 2005). In the second model, we take the parameters for the luminosity obtained from the SN simulation results.

3.1. Equivalent (EQ) Luminosity Model

The first case is the equivalent neutrino luminosity, which is given as (Yoshida et al. 2004)

$$L_{\nu_\alpha}(t) = \frac{1}{6}\frac{E_\nu}{\tau_\nu}\exp\left(-\frac{t - r}{\tau_\nu}\right)\Theta(t - r), \quad (14)$$

where we take the total explosion energy $E_\nu = 3 \times 10^{53}$ erg and the decay time of luminosity $\tau_\nu = 3$ s. The quantities t and r are the time after explosion and the radius from the core, respectively. The exponential decay form of the luminosity stands for the cooling phase, in which most of the neutrino energy is brought out (Woosley et al. 1990; Heger et al. 2005; Raffelt 2012; Sieverding et al. 2019). Θ is the Heaviside step function, which makes the luminosity zero before the arrival of the neutrinos at the position r. In this EQ model, we assume the FD distribution, with $T_{\nu_e} = 3.2$ MeV, $T_{\bar\nu_e} = 5$ MeV, and $T_{\nu_{\mu,\tau},\bar\nu_{\mu,\tau}} = 6$ MeV.

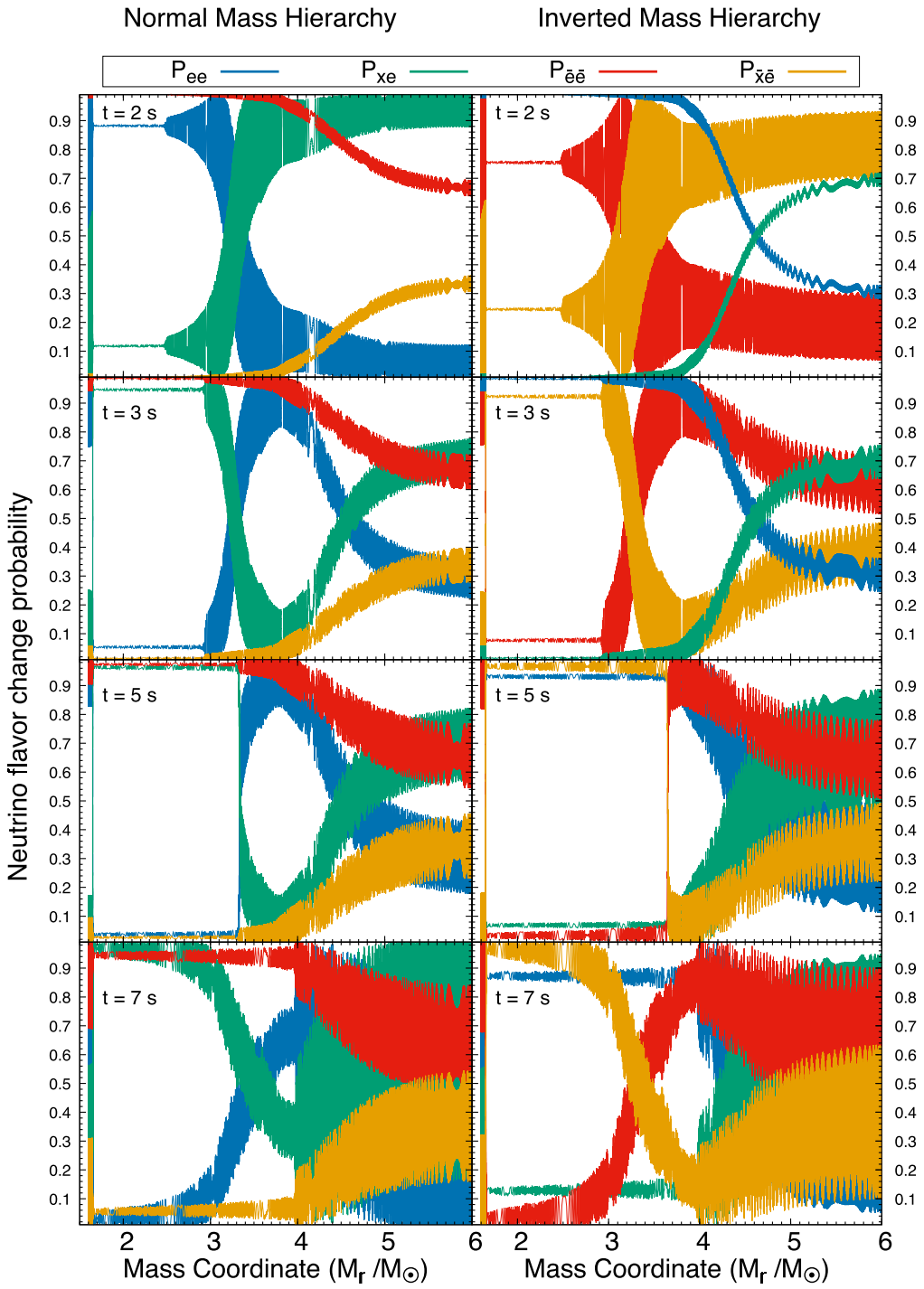

Figure 6. The flavor change probabilities, including the shock propagation effect, in the KCK19 model (Kusakabe et al. 2019) at $t = 2$, 3, 5, and 7 s for $E_\nu = 15$ MeV. The labels denote the probabilities as in Figure 4, i.e., $P_{ee} = P_{\nu_e \to \nu_e}$ and $P_{xe} = P_{\nu_\mu \to \nu_e} + P_{\nu_\tau \to \nu_e}$. The left and right panels correspond to the NH and IH, respectively.

By adopting this model, the differential neutrino flux is given as

$$\phi'(t, r; E_\nu, T_{\nu_\alpha}) \equiv \frac{d}{dE_\nu}\phi(t, r; E_\nu, T_{\nu_\alpha})$$
$$= \frac{L_{\nu_\alpha}(t)}{4\pi r^2}\frac{1}{T_{\nu_\alpha}^4 F_3(0)}\frac{E_\nu^2}{\exp(E_\nu/T_{\nu_\alpha}) + 1}\langle \rho_{\alpha\alpha}(r; E_\nu)\rangle, \quad (15)$$

where $F_3(0) = 5.6882$ in the Fermi integration and $\langle \rho_{\alpha\alpha}(r; \epsilon_\nu)\rangle$ is the angular averaged neutrino density matrix of ν_α from Equation (9).

For IH, Figure 9 shows the neutrino spectra obtained by $4\pi r^2 \phi'(r, E_\nu, T_{\nu_\alpha})$ at $t = 1$ s in Equation (15). At $r = 10$ km, we take the spectra as the FD distribution. As shown in Figure 9, over the $E_\nu = 17$ MeV region, the ν_e is distributed more than the others before the SI occurs. This enhanced high-energy tail

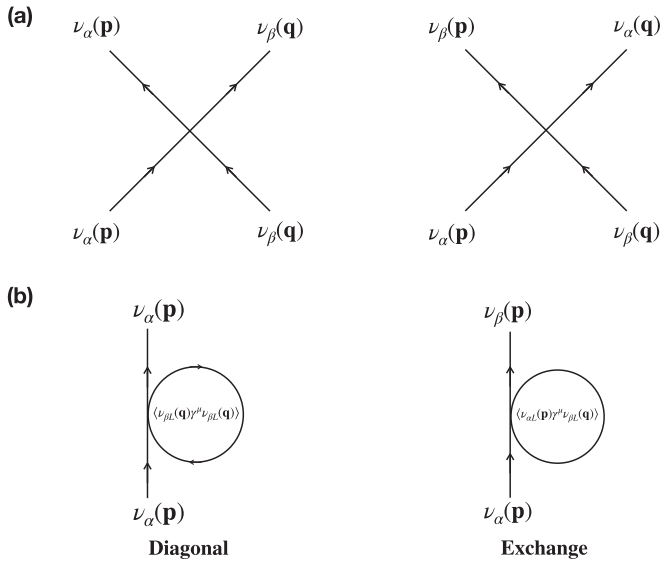

Figure 7. (a) The ν–ν interaction diagrams. The left and right diagrams correspond to the diagonal and exchange terms, respectively. (b) The mean-field approximation for the four-fermion interaction of the diagonal and exchange terms in panel (a).

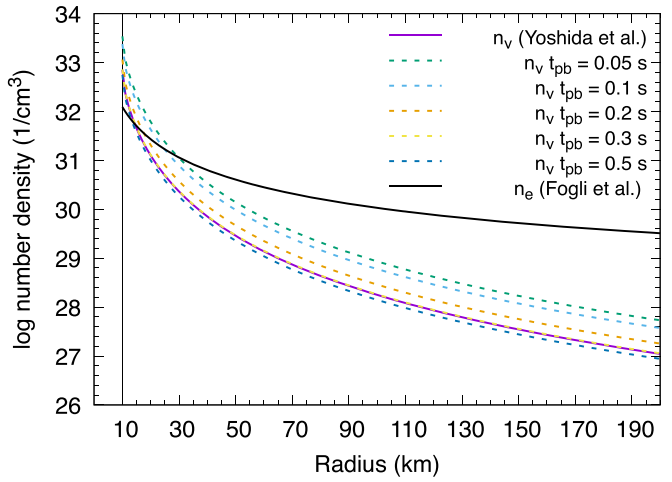

Figure 8. The number density of electrons and electro-neutrinos. Each dashed line stands for the number density at the post-bounce times $t_{pb} = 0.05$, 0.1, 0.2, 0.3, and 0.5 s, as labeled.

originates from the reduced ν_μ and ν_τ distributions, so that the total number of the neutrinos is conserved. On the other hand, $\bar{\nu}_e$ changes from $\bar{\nu}_\mu$ and $\bar{\nu}_\tau$, similar to the MSW resonance effect. For NH, the SI effect is suppressed and, consequently, there is no difference compared to the case without the SI term.

3.2. Nonequivalent (NEQ) Luminosity Model

The neutrino luminosity of each flavor may have different epochs in CCSNe explosions, which are classified into three phases by neutrino signals (Fischer et al. 2010; Raffelt 2012): the burst, accretion, and cooling phases. In the present study, we ignore the ν_e burst phase, in which the prompt deleptonization process of the electrons occurs at the post-bounce time $t_{pb} \sim 0.01$ s. The shock propagation from the inner core drives the dissociation of heavy nuclei into protons and neutrons. Consequently, the electron captures ($e^- + p \rightarrow n + \nu_e$) produces the ν_e burst.

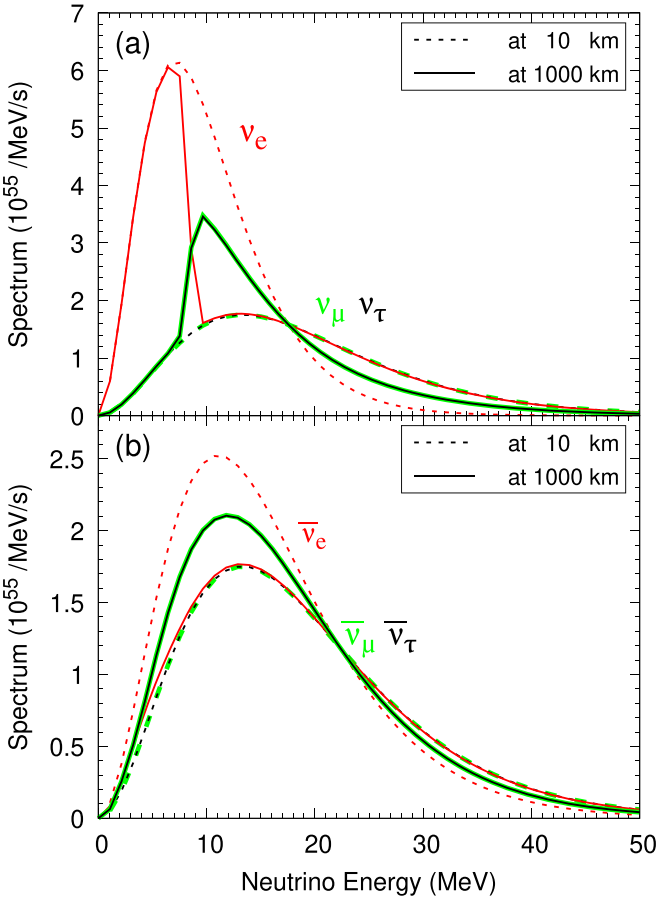

Figure 9. The neutrino spectra ($\equiv 4\pi r^2 \phi'$) with SI effects for IH. The upper and lower panels show the ν and $\bar{\nu}$ cases, respectively.

The sensitivity of the ν_e burst phase on the ν-process was studied by varying the electron neutrino luminosity in Sieverding et al. (2019). According to the study, however, the yields of the synthesized elements in the ν-process increase maximally only up to 20% for ^{138}La and 5% for ^{11}B when an FD distribution is adopted. The other elements of ^{7}Li, ^{15}N, ^{19}F, and ^{180}Ta increase by less than about 1%. Hence, in our study, we only consider the cooling phase presumed by the exponential decay (Woosley et al. 1990; Yoshida et al. 2004; Heger et al. 2005; Sieverding et al. 2019) and a partial accretion phase, when the shock wave stagnates due to the falling materials and deposits its energies.

To investigate the accretion phase before $t_{pb} \simeq 1$ s, we take the SN simulation data in O'Connor et al. (2018). This study compared the results of six individual SN simulation models performed by different study groups and showed the consistency of the CCSN explosion mechanism. We take the neutrino luminosities and averaged energies by selecting five post-bounce times, i.e., 0.05, 0.1, 0.2, 0.3, and 0.5 s. These time-dependent data are necessary not only for the neutrino propagation, but also for the calculation of the ν-process. For simplicity, we set the time interval between the five selected times as the numbers in the eighth column of Table 2 and use the step function form shown in Figure 10. As mentioned already, we ignore the ν_e burst in the $0.00 < t_{pb} < 0.05$ region in O'Connor et al. (2018). We treat the luminosities after 0.5 s in the cooling phase as the exponential decay, i.e., $L_\nu(t) = L_\nu(500\ \mathrm{ms}) \times \exp(-(t - r)/\tau_\nu)\Theta(t - r)$.

Table 2
Neutrino Luminosity Data at Given Time Intervals Taken from O'Connor et al. (2018)

Time (s)	L_{ν_e}	$L_{\bar{\nu}_e}$ (10^{52} erg s^{-1})	L_{ν_x}	$\langle E_{\nu_e}\rangle$	$\langle E_{\bar{\nu}_e}\rangle$ (MeV)	$\langle E_{\nu_x}\rangle$	Interval Section (ms)
0.05	6.5 (4.1)[a]	6.0 (3.8)	3.6 (2.3)	9.3	12.2	16.5	0–75
0.1	7.2 (4.5)	7.2 (4.5)	3.6 (2.3)	10.5	13.3	16.5	75–150
0.2	6.5 (4.1)	6.5 (4.1)	2.7 (1.7)	13.3	15.5	16.5	150–250
0.3	4.3 (2.7)	4.3 (2.7)	1.7 (1.1)	14.2	16.6	16.5	250–350
0.5	4.0 (2.5)	4.0 (2.5)	1.3 (0.8)	16.0	18.5	16.5	350–500[b]

Notes.
[a] The values in parentheses mean (10^{58} MeV s^{-1}) units.
[b] After 500 ms, the exponential decay, $\exp(-(t-r)/\tau_\nu)$, is assumed.

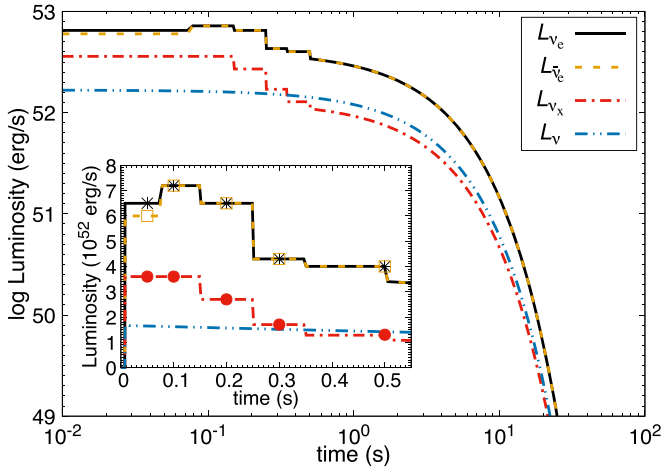

Figure 10. The neutrino luminosities for each flavor: ν_e, $\bar{\nu}_e$, and $\nu_x(=\nu_\mu, \nu_\tau, \bar{\nu}_\mu$ and $\bar{\nu}_\tau)$ in the region of $M_r \sim 1.6 M_\odot$ (corresponding to $r \approx 2300$ km). The inset shows an enlarged figure of the x- and y-axes. The yellow line denotes the luminosity calculated by Equation (14) and the others are adopted from Table 2.

Using the parameters in Table 2, we solve the equation of motion for neutrinos described in Equation (9). Figures 11 and 12 show snapshots of the neutrino spectra at the denoted times. Contrary to the EQ model, in the NEQ model, we find that the neutrino SI affects the neutrino spectra for both MH cases.

For the NH case, neutrinos propagating from the neutrino sphere ($r \simeq 10$ km) interact with the background neutrinos. Considering the neutrino SI with Equation (9), we get the neutrino spectra. From $r = 10$ km to $r = 2000$ km, the ν-SI affects each neutrino flavor spectrum, and after $r = 2000$ km the ν-SI does not contribute to the neutrino spectra. Hence, we compare the spectra at $r = 10$ km and $r = 2000$ km (Figure 11).

At $t = 50$ ms and $t = 100$ ms, the spectra of ν_e and $\nu_x(x = \mu$ and $\tau)$ intersect at $E_\nu \sim 20$ MeV and 23 MeV, respectively. After these cross points, the high-energy tail of the ν_e spectra is enhanced, while the spectra in the $E_\nu < 5$ MeV region are same. As a result, the first and second panels of Figure 11 disclose that the comparable luminosity of ν_x forces the high-energy tail of the ν_e spectra. Also, this trend is seen in the case of the antineutrinos. On the other hand, at the next time steps of $t = 200$, 300, and 500 ms, although the averaged energy of ν_x becomes higher than at the previous time steps, the spectra of ν_e are reduced from the initial spectra, owing to the lower luminosity of ν_x.

In the case of IH, the neutrino spectra are shown for $r = 10$ km and $r = 1000$ km in Figure 12. The spectra are not changed after $r = 1000$ km. Similar to the EQ model, the IH case shows that the spectra at $t = 50$ ms and 100 ms are split in the low-energy region. Although this behavior is similar to the EQ model, the difference occurs in the high-energy tail. Analogous to the previous NH case, at $t = 50$ ms and $t = 100$ ms, the spectra of ν_e increase at $E_\nu = 20$ MeV and $E_\nu = 23$ MeV, respectively. Furthermore, at the region of $E_\nu > 7$ MeV, the ν_e spectra change to ν_x. This change is distinct from the previous NH case involving only a partial change in that energy region. Also, although the spectra at $t = 200$, 300, and 500 ms indicate the splitting of the spectra, the ν_e spectra are lower than their initial spectra. This is because the luminosity is too low at that time, as in the NH case. On the other hand, the $\bar{\nu}_e$ is fully changed to the $\bar{\nu}_x$ over the whole region. Consequently, the spectra are the same as the initial $\bar{\nu}_x$ spectra shown in the right panels of Figure 12.

4. Explosive Nucleosynthesis

The stellar temperature ranging from 10^6 K to 10^9 K is high enough that thermonuclear reactions operate and become the main input of the nucleosynthesis. We perform a network calculation containing about 38,000 nuclear reactions for 3080 nuclides up to the ^{232}Fr isotopes by taking the result of the SN1987A progenitor model. After the helium and carbon burning, as well as the weak s-process, of the progenitor model, we make an explosion described by hydrodynamics, from which the time evolution of the abundances is considered. The initially emitted neutrinos react with nuclides generated in the pre-SN phase during the CCSN explosion. After a few seconds, the shock propagation from the core arrives at each layer and increases the density, radius, and temperature affecting the nucleosynthesis. This section addresses the thermonuclear reaction formulae for the explosive nucleosynthesis.

4.1. Thermonuclear Reactions

For the nuclear reactions in stellar environments, assuming that the reacting nuclei stay in local thermal equilibrium, we use thermal averaged reaction rates with the Maxwell–Boltzmann distribution (Angulo et al. 1999). The standard reaction rates are taken from the JINA REACLIB database

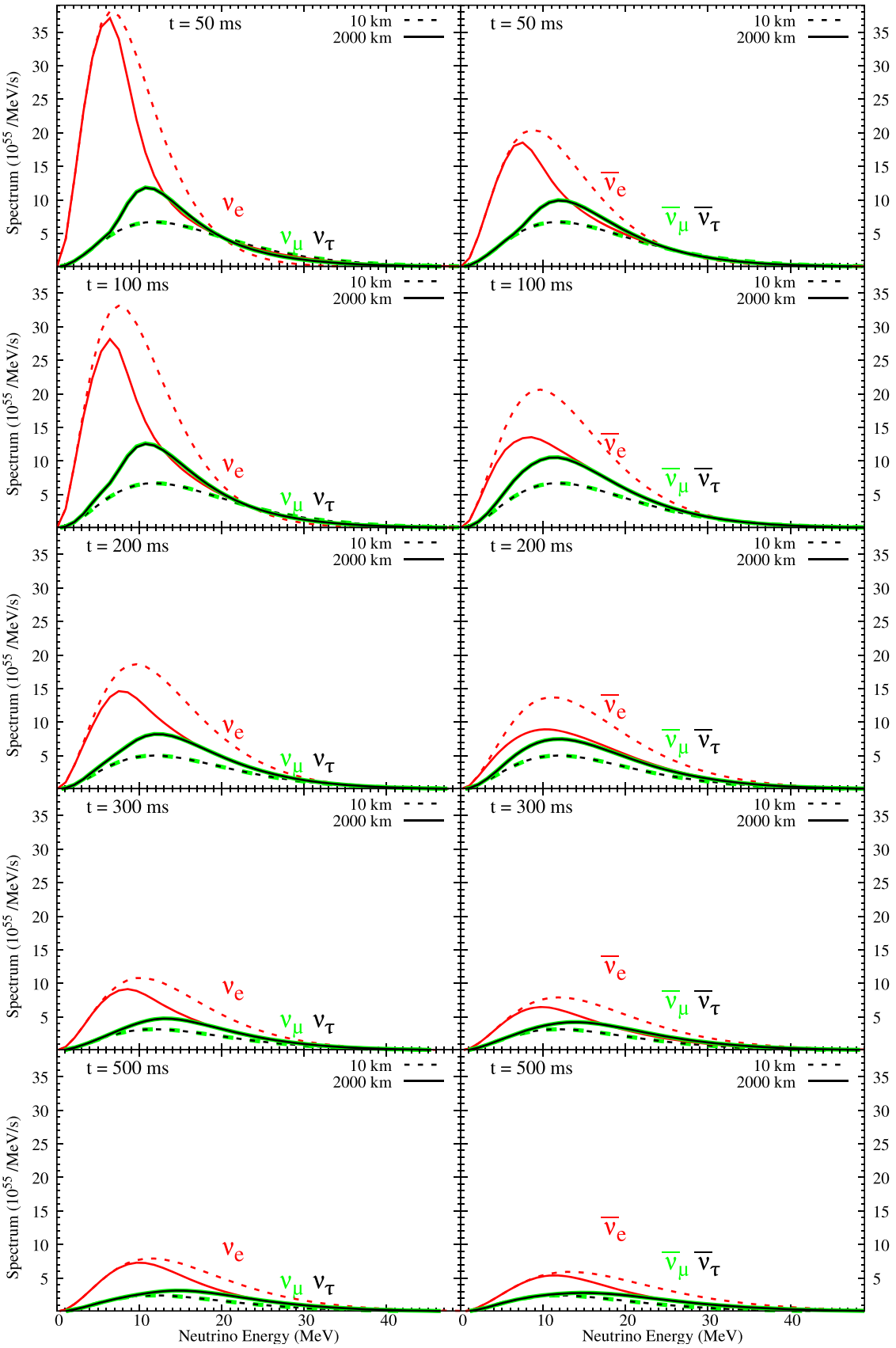

Figure 11. The neutrino spectra including neutrino SI at $t = 50$, 100, 200, 300, and 500 ms for the NH case. The dashed and solid lines denote the spectra at $r = 10$ km and 2000 km, respectively. The red, green, and black lines denote ν_e, ν_μ, and ν_τ.

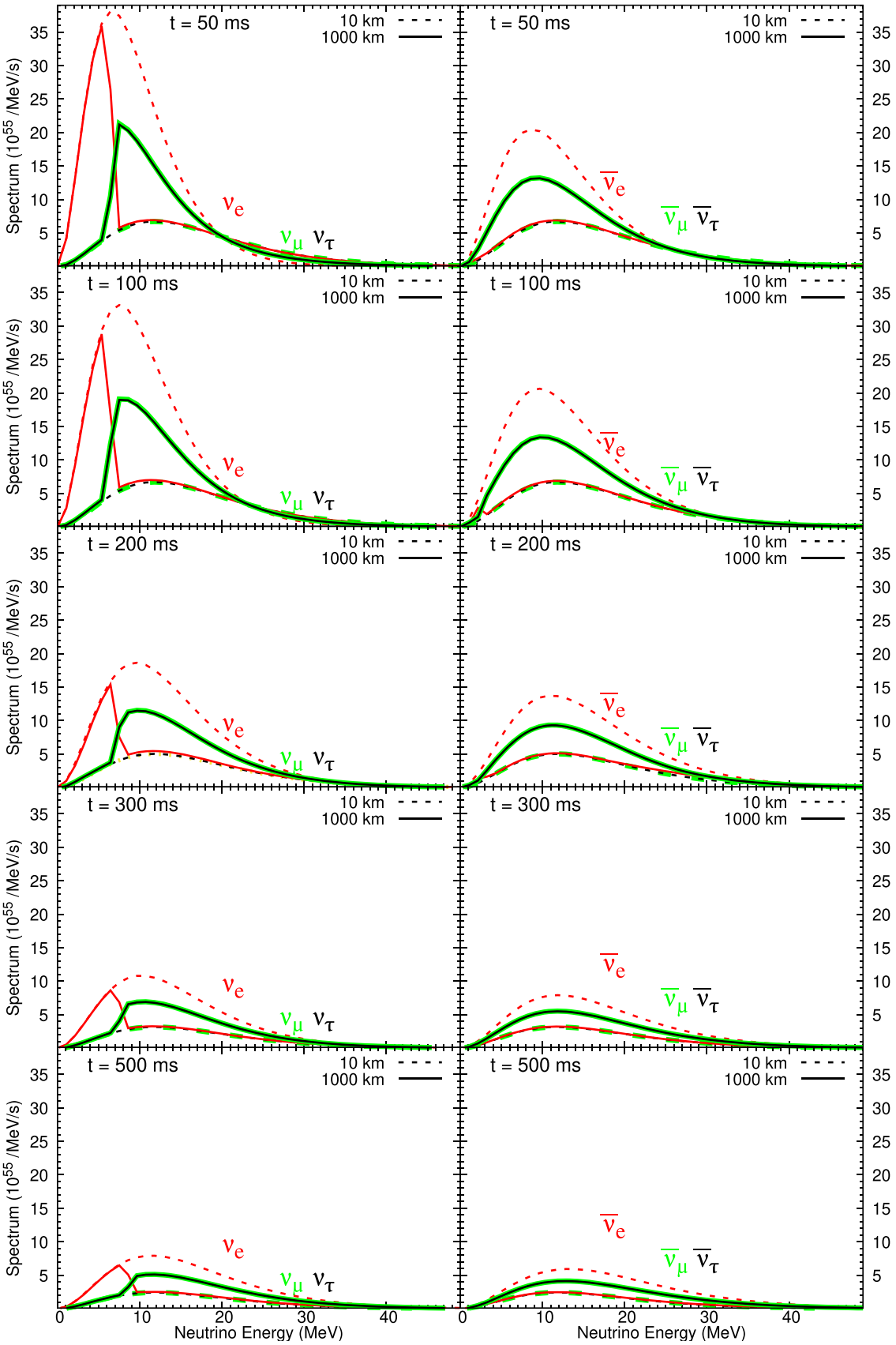

Figure 12. The same as Figure 11, but for the IH case at 10 km and 1000 km.

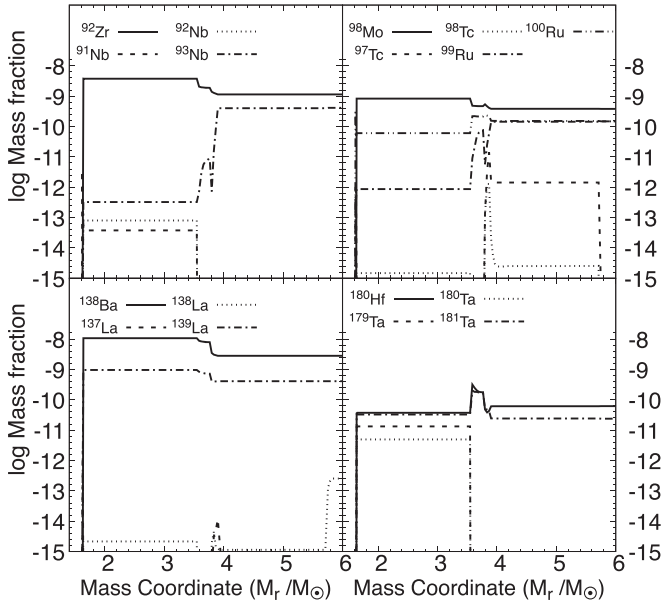

Figure 13. The logarithmic nuclear mass fractions in the pre-SN model used in the present work (Kikuchi et al. 2015).

(Cyburt et al. 2010). Based on the averaged reaction rates, the time evolution of the abundance Y_i, defined as $Y_i = N_i/(\rho_b N_A)$ with the baryon density ρ_b and the number density N_i for a species i, is described in terms of forward (+) and reverse (–) reactions, as follows:

$$\begin{aligned}\frac{dY_i}{dt} = &+Y_j\lambda_{j,i} - Y_i\lambda_{i,k} \\ &+ Y_m Y_n(\rho_b N_A)\langle\sigma v\rangle_{mn,i} - Y_i Y_o(\rho_b N_A)\langle\sigma v\rangle_{io,p} \\ &+ Y_q Y_r Y_s(\rho_b N_A)^2\langle qrs\rangle_i \\ &- Y_i Y_t Y_u(\rho_b N_A)^2\langle itu\rangle_v \\ &+ Y_w Y_x Y_y Y_z(\rho_b N_A)^3\langle wxyz\rangle_i \\ &- Y_i Y_a Y_b Y_c(\rho_b N_A)^3\langle iabc\rangle_d, \end{aligned} \quad (16)$$

where $\langle\sigma v\rangle_{ij,k}$ is the thermal average of the product of the cross section for $i + j \rightarrow k$ and relative velocity v. For the case including identical particles, to avoid double counting, the coefficients of 1/2! (for an identical pair among three species) or 1/3! (for all identical particles) are multiplied. $\langle qrs\rangle_i$ ($\mathrm{cm}^6\ \mathrm{s}^{-1}$) is the three-body reaction rate, and $\langle wxyz\rangle_i$ ($\mathrm{cm}^9\ \mathrm{s}^{-1}$) is the four-body reaction rate.

The yields of the explosive nucleosynthesis are determined by this equation, and therefore what we adopt for the reaction rates is important. In the present work, in addition to the JINA REACLIB database, we adopt modified neutron capture and neutrino-induced reaction rates (See Appendix C).

4.1.1. Neutron Capture (n, γ) Reaction Rate

Neutron capture reactions are important for producing heavy elements in neutron-rich environments via the *r*- and *s*-processes (Burbidge et al. 1957). Around $A \sim 100$, we utilize the neutron capture reaction rates calculated by the Monte Carlo method for the particle emission from the compound nucleus based on the Hauser–Feshbach statistical model (Angulo et al. 1999; Kawano et al. 2010). A comparison between the adopted reaction rates and those in the JINA database is shown in Figure 18. For those nuclei in the present calculation, the partition functions for the excited states are taken into account. The (n, γ) reactions and their reverse reactions are displayed in Figures 18 and 19, respectively, in Appendix C. In particular, the increased temperature and density from the shock propagation effect are relevant to the photodisintegration reactions in the region inside $M_r \sim 2M_\odot$.

4.1.2. Neutrino-induced Reaction Rates

The weak interaction of neutrinos is feeble compared to other interactions. However, in the CCSN environment, the neutrino-induced reactions are considerable, because of the high neutrino fluxes, and crucially affect the yields of the nucleosynthesis. The thermal averaged neutrino reaction rate for ν_α is given as

$$\lambda_{\nu_\alpha}(t, r) = \frac{1}{4\pi r^2}\sum_{\beta=e,\mu,\tau}\left[\frac{L_{\nu_\beta}(t)}{F_3(0)T_{\nu_\beta}^4} \times \int \frac{E_\nu^2\sigma_{\nu_\alpha}(E_\nu)\langle\rho_{\alpha\alpha}(r_c; E_\nu)\rangle P_{\nu_\beta\nu_\alpha}(r; E_\nu)}{\exp(E_\nu/T_{\nu_\beta}) + 1}dE_\nu\right], \quad (17)$$

where L_{ν_β} is the luminosity and T_{ν_β} is the temperature of ν_β. The cutoff radius r_c is set as 1000 km or 2000 km, where ν-SI is no longer effective. The cross section σ_{ν_α} between a nucleus and a neutrino depends on the nuclear structure model and is an important input for determining the neutrino-induced reaction rate.

In order to obtain the cross sections between the nucleus and neutrinos, there are two kinds of approach—the nuclear shell model (SM) and quasiparticle random phase approximation (QRPA). Compared to the SM, QRPA is advantageous, because the Bardeen–Cooper–Schrieffer theory can be used for the nuclear ground state, making it possible to perform efficient calculations of the nuclear excitations of the medium and heavy nuclei. Despite this efficiency, the results for the SM and QRPA do not show any significant differences within the error bar (Yoshida et al. 2008; Cheoun et al. 2010; Suzuki & Kajino 2013). For ^{4}He and ^{12}C, we take the cross sections from the SM from Yoshida et al. (2008); for nuclei of ^{13}C to ^{80}Kr, we take them from stellar nucleosynthesis data (Hoffmann and Woosley 1992); and for the heavy elements of ^{92}Nb, ^{98}Tc, ^{138}La, and ^{180}Ta, we take them from the QRPA from Cheoun et al. (2010, 2012). Numerical results of the neutrino-induced reactions by the QRPA for the heavy elements are tabulated in Tables 8 and 9 in Appendix C. Also, main neutrino-induced reactions relevant to the nuclei produced by the neutrino process are summarized in Table 10 in Appendix D.

5. Nuclear Abundances from the ν-Process

In this section, with the nuclear reaction rates described in the previous section, we analyze the elements that are prominently produced by neutrino-induced reactions during CCSN explosion. The main factors of the CCSN ν-process are the pre-SN seed abundances, the number densities of electrons and neutrinos, and the shock propagation during the explosion. As seed elements for the CCSN ν-process, we adopt the pre-SN model, including modified neutron capture rates for $A \sim 100$ nuclei (Kawano et al. 2010), which are shown in Figure 13. Based on the pre-SN model, we discuss the production mechanism for the SN ν-process elements in three different

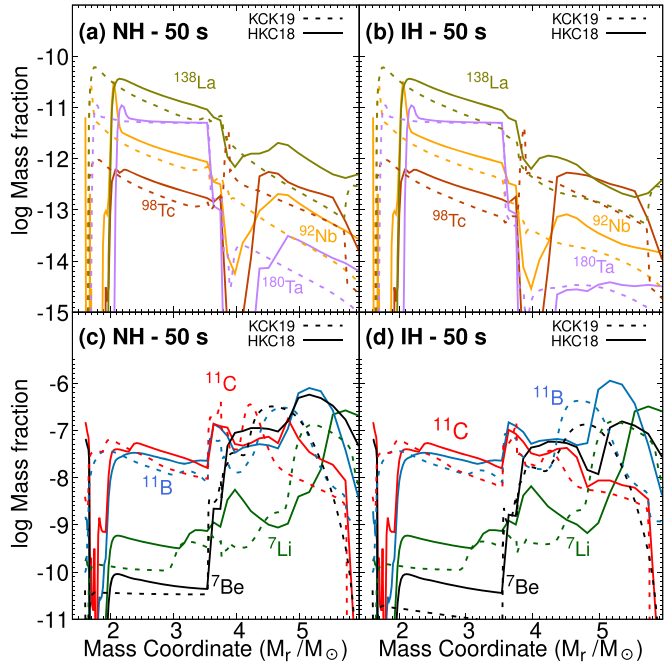

Figure 14. Logarithmic mass fractions of heavy nuclei: ^{92}Nb, ^{98}Tc, ^{138}La, and ^{180}Ta vs. the mass coordinate. Panels (a) and (b) correspond to the yields for NH and IH, respectively. Panels (c) and (d) denote light nuclei: ^{7}Li, ^{7}Be, ^{11}B, and ^{11}C. The dashed and solid lines, respectively, stand for the results from the hydrodynamics of the HKC18 and KCK19 models. All results are the nuclear abundances synthesized about 50 s following the CCSN explosion.

aspects: effects of hydrodynamics, shock propagation, and neutrino collective oscillation from the ν-SI. Since the neutrino oscillation behavior depends on the neutrino MH, we also investigate each model with the two kinds of neutrino MH. Consequently, 12 models are studied for the yields of the ν-process elements.

5.1. Hydrodynamics Dependence

First, we discuss the effects of different hydrodynamics models on the CCSN ν-process yields. For the hydrodynamics models, we take the two different models described in Section 2, i.e., HKC18 and KCK19. As explained in the previous section, the different temperature and baryon density profiles affect the thermonuclear reaction rates and neutrino oscillation behavior during the SN explosion. Figure 14 shows the synthesized abundances of heavy (^{92}Nb, ^{98}Tc, ^{138}La, and ^{180}Ta) and light nuclei (^{7}Li, ^{7}Be, ^{11}B, and ^{11}C) from the two models. One may confirm that the heavy (apart from ^{98}Tc) and light nuclei are, respectively, mainly produced in the O–Ne–Mg layer ($1.6M_\odot \lesssim M_r \lesssim 3.7M_\odot$) and the He layer ($3.9M_\odot \lesssim M_r \lesssim 6M_\odot$), irrespective of the adopted hydrodynamics.

5.1.1. Heavy Elements Synthesis

The main reactions producing the heavy elements are neutrino CC reactions. Neutrinos propagating from the SN core react with seed nuclei in the pre-SN model (see Figure 13). The main reactions producing ^{92}Nb and ^{138}La are ^{92}Zr(ν_e, e^-)^{92}Nb and ^{138}Ba(ν_e, e^-)^{138}La, respectively (see Figures 24 and 26 in Appendix D). Since the neutrino flux decreases with an increasing radius from the core, the rates of the main reactions related to those abundances decrease. As a result, the yields of ^{92}Nb and ^{138}La decrease from the flat abundance pattern of the adopted pre-SN model due to the neutrino reactions as they go outward. The main production reactions of ^{180}Ta are ^{179}Ta (n, γ) ^{180}Ta and ^{180}Hf (ν_e, e^-) ^{180}Ta, as shown in Figure 27. However, the preexisting abundance of ^{180}Ta in the pre-SN phase is larger than the production from the nearby seed nuclei during the SN explosion, so the ν-process has only a minor effect on ^{180}Ta production in the present models.

On the other hand, the ^{98}Tc nuclei are evenly produced over the whole region by reactions of ^{98}Mo(ν_e, e^-)^{98} Tc (inner region; $M_r \lesssim 4M_\odot$) and ^{97}Tc(n, γ)^{98} Tc (outer region; $M_r \gtrsim 4M_\odot$) (see Figure 25). Also, unlike other heavy elements, the CC reactions induced by $\bar{\nu}_e$ maximally contribute about 12% and 8% in the HKC18 and KCK19 models, respectively. The present results of the HKC18 model differ a bit from our those of previous study in Hayakawa et al. (2018). This is because the abundance of the seed nucleus, ^{97}Tc, is a bit larger in the current pre-SN phase (Figure 13).

In Figure 14, a valley appears around the region of $M_r \sim 4M_\odot$ in the HKC18 model, but it disappears in the KCK19 model. In this region, the neutron capture rates are important not only for production, but also for destruction. The major production of ^{98}Tc is from ^{97}Tc (n, γ)^{98} Tc, and the destruction comes from ^{98}Tc (n, γ)^{99} Tc. The valley arises from the density discrepancy between the HKC18 and KCK19 models (Figure 2). The density in the HKC18 case is one order of magnitude higher than in the KCK19 case, until the shock passes. As a result, the ^{98}Tc is more heavily destroyed by the reaction ^{98}Tc (n, γ)^{99} Tc.

Another discrepancy between the hydrodynamics appears at $M_r \sim 2M_\odot$, where the threshold positions of the producing elements are different. This fact arises from the coincidence between the hydrodynamics and pre-SN models. The pre-SN calculation gives the initial elemental abundances in each region. According to Figures 1 and 2, however, the initial density and temperature of HKC18 are higher than those of the pre-SN model adopted in the KCK19 model. Consequently, the higher density and temperature profiles in HKC18 increase most of the reaction rates, especially the photodisintegration rate, which forms the valley in this region.

The trends of the ν-process yields are similar in the both hydrodynamics models, aside from the valley and photodisintegration region, while the total abundances of ^{92}Nb, ^{98}Tc, and ^{138}La differ by about less than 13%, as shown in Table 4. In our previous studies, Hayakawa et al. (2018) and Ko et al. (2020), the hydrodynamics of HKC18 were used. However, it was found that there was a discrepancy of the density profile between the HKC18 model and the adopted pre-SN model, which spawned the discontinuities of the physical quantities as a function of time. In order to be consistent with the pre-SN model (Kikuchi et al. 2015), in this paper we exploit the KCK19 model for more systematic investigations, because the two models are consistent with each other. In the last two lines of Table 4, we compare the results with the previous results from HKC18.

5.1.2. Light Elements Synthesis

The light elements, ^{7}Li and ^{7}Be, are mostly synthesized in the outer region, while ^{11}B and ^{11}C are produced over the whole region. In the inner region ($M_r < 4M_\odot$), the light elements are produced by the neutrino reaction, and outside the

region alpha capture reactions at the He layer mainly contribute to the production of light elements. The hydrodynamics models also affect the synthesis of light elements by changing the ν-process environment.

First, the dependence on hydrodynamics stems from the radius profiles (Figure 3). As seen in Equation (17), the neutrino reaction rate is inversely proportional to the squared radius. The discrepancy of the radius profiles, $R_{KCK19} > R_{HKC18}$, makes the neutrino reaction rates different. As a consequence, the results of KCK19 show lower abundances than those of the HKC18 model in the O–Ne–Mg layer, as shown in Figures 14(c) and (d).

Second, the different density profiles in the He layer also affect the nucleosynthesis. Within the same neutrino oscillation parameters, the discrepancy of the density profiles causes the different MSW regions, which result in the change of the ν-induced reaction rates. The change of the MSW region due to the hydrodynamics models is closely related to the synthesis of the light elements—especially for ^{7}Be and ^{11}C (Kusakabe et al. 2019).

Third, the temperature profiles are also important for determining the alpha capture reactions, as well as their destruction rates. Higher temperatures imply higher reaction rates, for both production and destruction. For example, for ^{11}B, in the region of $4.5 < M_r/M_\odot < 5$, the temperature profile of the HKC18 model is higher than that of the KCK19 model, but the abundance of ^{11}B does not follow the temperature pattern. This is because the higher temperature more heavily stimulates the destruction of ^{11}B. For a detailed analysis of the light elements, we should investigate the main reactions of the elements for a given hydrodynamics condition, which is discussed in the Subsection 5.2.2.

5.2. Shock Propagation Effect

As delineated in Section 2, the matter potential related to the MSW resonance is determined by the electron density. During the explosion, the matter density is changed by the shock propagation, and the neutrino oscillation probability subsequently varies (Figure 6) and affects the neutrino reaction rates. We refer to this effect here as the "shock effect."

The ν-process elements are sensitive to the neutrino flavor distribution and luminosity. For example, for $E_\nu = 15$ MeV, multiple resonances occur at $t \sim 3s$ in Figure 6 (Ko et al. 2019). At $t = 3s$, the neutrino luminosity is about 0.37 times smaller than the initial luminosity (Equation (14)). Then a competition may occur between the luminosity and flavor change probabilities in the neutrino reaction rate. The neutrino luminosity decreases over time, resulting in a decrease in the reaction rates. However, a decrease in the CC reaction rate can be partially compensated for by the effect of the flavor change to ν_e caused by the shock propagation. Hereafter, we adopt the KCK19 hydrodynamics for the forthcoming results.

5.2.1. Heavy Elements Synthesis

Since the heavy elements are mainly produced by the CC reactions, it is important to estimate the quantity of ν_e as a function of the mass coordinate. The multiple resonances caused by the shock promote the flavor change from ν_μ and ν_τ to ν_e. This change of the neutrino flavor transition region is more significant for the NH case than the IH case.

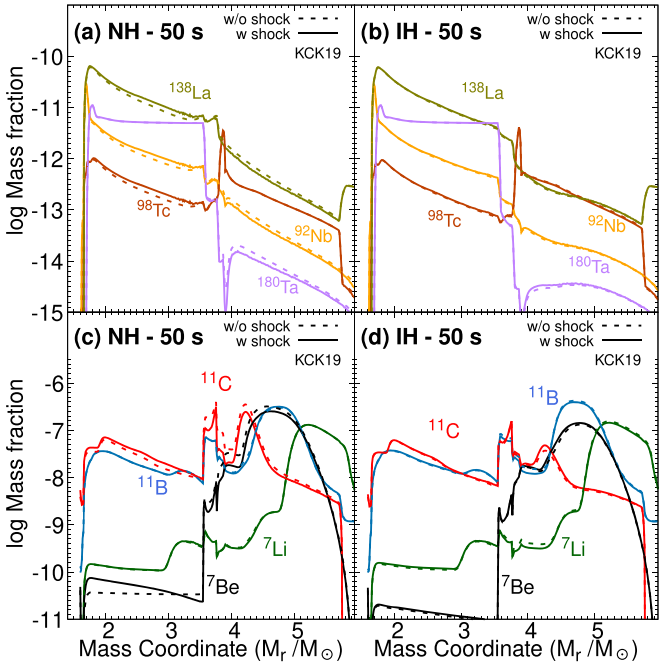

Figure 15. Logarithmic mass fractions of the heavy and light elements at 50 s after the core bounce over the mass coordinate for the shock effect. Panels (a) and (b) show the heavy elements, while panels (c) and (d) show the light elements. In each panel, the solid and dashed lines denote the cases with and without shock effect, respectively.

Figure 15(a) shows the production of heavy elements for the NH case. The resonance in the inner region increases the CC reaction rates. Therefore, in the region $M_r \sim 1.6$–$3.9M_\odot$, the abundances of the heavy elements—except for ^{180}Ta—increase due to the shock propagation. However, by the second resonances at $M_r \sim 3.7M_\odot$, the distribution of ν_e returns to its initial distribution. Consequently, the shock effect only enhances the production of heavy elements within $M_r \sim 1.6$–$3.9M_\odot$. Specifically, the shock propagation enhances the abundances of ^{92}Nb, ^{98}Tc, and ^{138}La by about 9%, 8%, and 11%, respectively. For the IH case, the shock effect has relatively less impact on the yields, that is, the abundances are maximally increased by about 1%, as shown in Figure 15(b).

5.2.2. Light Elements Synthesis

The production mechanism of the light elements has been studied by Kusakabe et al. (2019). We briefly review the main production reactions of the light elements and investigate the shock effect. Table 10 and Figures 20–23 in Appendix D show the relevant nuclear reactions. In Figures 15(c) and (d), around the region of $M_r \sim 1.6$–$3.9M_\odot$, the NC reaction in the $^{12}\mathrm{C} + \nu$ reactions mainly produces ^{11}B and ^{11}C. Since all flavors contribute to the NC reaction, the neutrino oscillation probability does not affect the reaction rate. Therefore, in this region, the production of ^{11}B and ^{11}C is independent of the shock propagation and MH. The various channels in the $^{12}\mathrm{C} + \nu$ reactions are explained in detail in Table 3.

On the other hand, in the region of $M_r \sim 3.9$–$6M_\odot$, most of the ^{11}B and ^{11}C are produced by alpha capture reactions of ^{7}Li and ^{7}Be, respectively. The dominant production processes for ^{7}Li are ^{4}He $(\nu, \nu' p)^3$ H $(\alpha, \gamma)^7$ Li and ^{4}He $(\bar{\nu}_e, e^+ n)^3$ H $(\alpha, \gamma)^7$ Li, and ^{7}Be is mainly produced by ^{4}He $(\nu, \nu' n)^3$ He $(\alpha, \gamma)^7$ Be and ^{4}He $(\nu_e, e^- p)^3$ He $(\alpha, \gamma)^7$ Be. The contribution of each

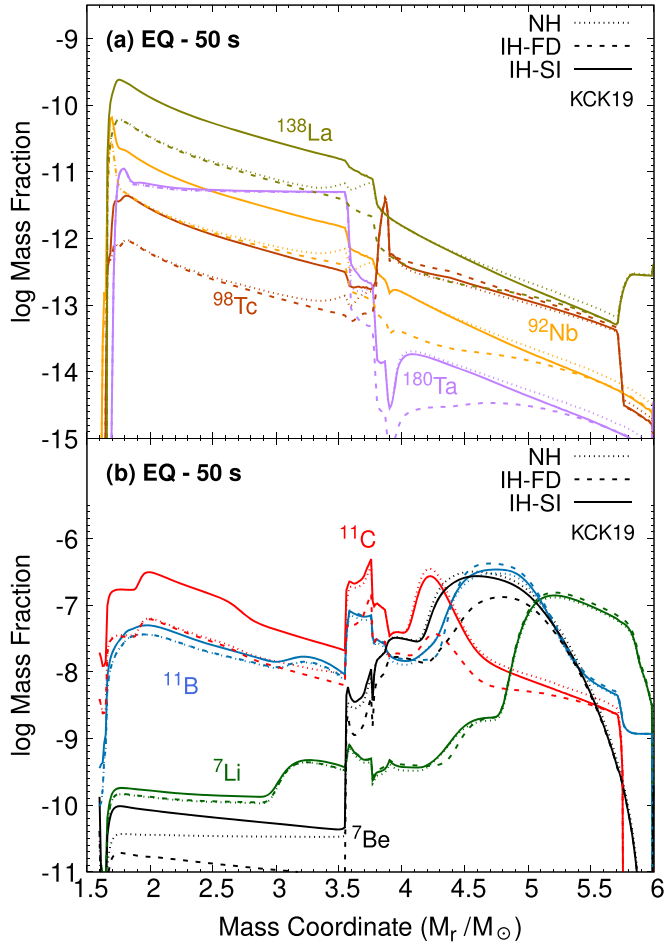

Figure 16. Logarithms of mass fractions of heavy (a) and light (b) elements over the mass coordinate. The solid and dashed lines denote the cases with and without ν-SI, respectively. The dotted line represents the NH case. All results are shown 50 s after the CCSN explosion. The results for the NH case are given without the SI effect.

reaction is succinctly presented in Figures 20 and 21 as well as Appendix D.

In the NH case, as shown in Figure 6, the $\bar{\nu}_e$ distribution with the shock propagation is similar to that without considering the shock. Therefore, the ^{7}Li and ^{11}B abundances are also not affected by the shock effect. The increments of ^{7}Li and ^{11}B are 0.04% and 2.7%, respectively. On the other hand, the ^{7}Be and ^{11}C abundances are more sensitive to the shock effect, and those abundances decrease by 22% and 21%, respectively. In the case of IH, because the distribution of ν_e is rarely varied, the shock effect is relatively small, and the change tendency is the opposite. The decreases of ^{7}Li and ^{11}B are 6.7% and 5.7%, and the increases of ^{7}Be and ^{11}C are 9.8% and 6.1%, respectively.

5.3. Collective Neutrino Oscillation Effect

As described in Section 3, the ν-SI affects the neutrino reaction rates through the change of the neutrino spectra. For the ν-SI, we investigate the ν-process with two different neutrino luminosity models—the EQ and NEQ luminosity models—explained in Section 3. Note that we do not simultaneously consider the shock effect in this section, to understand only the ν-SI effect. The shock effects are less than 11% for the heavy elements and 22% for the light elements, as discussed in the last section.

Table 3
Main Production Channels for ^{11}C and ^{7} Be in the Range $2M_\odot \lesssim M_r \lesssim 4M_\odot$

Element	Main Reactions with ν-SI
^{11}C	^{12}C $(\nu_e, e^-)^{12}$ N $(\gamma, p)^{11}$ C
	^{12}C $(\nu_e, e^-)^{12}$ N*, N$^* \rightarrow {}^{11}$C + p
^{7}Be	^{12}C $(\nu_e, \nu_e a)^7$ Be; $a = (\alpha + n, 3p + 2n, ..)$
	^{12}C $(\nu_e, e^-)^{12}$ N, ^{12}N $\rightarrow {}^8$B + a; $a = (\alpha, 2p + 2n, ...)$

5.3.1. EQ Luminosity

In the EQ luminosity model, each neutrino luminosity exponentially decreases with time, owing to a flavor-dependent temperature. As shown in Figure 9, ν_e and $\bar{\nu}_e$ have high-energy tails in their distributions, which can increase the CC reaction rates. As a result, Figure 16(a) shows that the ν-SI effects increase the synthesis of the heavy elements for both the NH and IH cases. Since the ν-SI effect on the neutrino spectra is not so significant for the NH case, we only show the results without the ν-SI. The SI increases the abundances of ^{92}Nb, ^{98}Tc, and ^{138}La by factors of 3.6, 2.7, and 4, respectively. The ^{180}Ta abundance is rarely changed, due to its high initial abundance (see Figure 13). We also find that there is only a small difference between the results for the NH and IH schemes due to the MSW effect on the outer region.

Figure 16(b) shows three cases of light element abundances. For the NH case and the IH with FD distribution (IH-FD) case, the key NC reactions in the inner region are the same as those explained in Section 5.2.2. In the case of IH including the ν-SI, the main reactions for producing the light elements are changed to the CC reaction.

The ν-SI effects on the light elements are explained as follows. Before undergoing the MSW resonance, $2M_\odot \lesssim M_r \lesssim 4M_\odot$, the production of all light elements is increased by the ν-SI, whose main reaction is changed from NC to CC reactions for ^{12}C, as tabulated in Table 3. As the spectra of ν_e increase in the higher-energy tails, the CC reactions in Table 3 become significant. In particular, the ^{7}Be and ^{11}C abundances are increased by 2.1 and 4.3 times, respectively, in this region, for the IH case. The abundances of ^{7}Li and ^{11}B are increased by 7% and 15%, which are small compared to ^{7}Be and ^{11}C.

5.3.2. NEQ Luminosity

Hereafter, we investigate the ν-SI effects with the NEQ luminosity model described in Table 2 and Figure 10, with KCK19 hydrodynamics. In this model, the luminosities of ν_e and $\bar{\nu}_e$ are higher than those of the EQ model. The higher luminosity activates related neutrino reactions. Hence, the abundances of both the heavy and light elements, which are shown in Figure 17, are larger than those in the EQ model. Note that the index of "NEQ-FD" means the "NEQ luminosity with Fermi–Dirac distribution."

On the other hand, the abundances of the heavy elements are reduced by the ν-SI, regardless of the MH, which is opposite to the trend in the EQ luminosity model. The heavy element synthesis is mostly affected by the cooling phase (exponential decay time), due to its longer duration of neutrino emission than the other explosion phases. The spectral change due to the

ν-SI at $t \gtrsim 0.5$ s from ν_e to ν_μ and ν_τ (and vice versa) decreases the ν_e number distribution, which is shown in the lowermost panels of Figures 11 and 12, and reduces the production of the heavy elements.

Here, we note the difference in abundance according to the MH. Unlike the EQ model, the NH case undergoes spectral change (Figure 11), after which the number of ν_e is more than the numbers of the other flavors in the beginning at $r = 10$ km. However, after the ν-SI interaction, ν_e turns into ν_μ and ν_τ, while the inverse flavor change does not sufficiently compensate for the initial ν_e number. Consequently, the production of the heavy elements decreases due to the reduction of the CC reaction rates.

In the IH case, the tendency of the spectra is similar to that of the EQ luminosity case in Figure 12. Despite these similarities, the flavor change cannot increase the neutrino CC reaction rate, because ν_μ and ν_τ have lower initial luminosities than ν_e at $t \gtrsim 200$ ms. Considering the spectra above $E_\nu \sim 10$ MeV, the NH case has larger ν_e number distribution than the IH case. As a result, the heavy element abundance in the NH case is larger than that in the IH case, due to the ν-SI.

Another interesting aspect of the heavy element synthesis is the competition of the ν-SI and the outer-region MSW effect. The elements decrease in both the NH and IH cases inside the MSW region. On the other hand, outside the MSW region, the elements increase due to ν-SI in the NH cases, because the ν_e number distribution is higher in the SI cases than the FD case, due to the exchange of the ν_e and ν_x spectra. However, in the IH case, the spectra are not fully exchanged. As shown in Figure 4(d), for $E_\nu = 15$ MeV, the electron neutrino spectrum is a mixture of about 30% ν_e and about 70% ν_x after the MSW resonance. Consequently, the ν_e spectrum in the FD case has a larger number distribution than that in the SI case.

For the light elements, the production of ^{11}B and ^{7}Li in the inner region, where NC reactions predominantly contribute, is less affected by the change of spectra. But for the ^{11}C and ^{7}Be synthesis, both the CC and NC reactions are important. As shown in Figures 17(c) and (d), when the NEQ luminosity model is adopted, the outermost peak of ^{11}C is affected, although it is subdominant in both the NH and IH cases. Since ^{11}C decays into ^{11}B, ^{11}B can be produced over the whole region.

In the $M_r \gtrsim 4M_\odot$ region (Figure 17), there is a novel feature, as the trends of the solid and dotted lines are opposite to each other. Namely, the MH dependence clearly appears. For the NH case in Figure 17(c), we find the increase of the ^{11}C and ^{7}Be abundances and the decrease of the ^{11}B and ^{7}Li abundances due to ν-SI. In this region, the neutrinos pass the MSW resonance region, and the ν_e spectra for the NEQ-FD and NEQ-SI cases follow the dashed and solid lines of the ν_μ and ν_τ spectra in Figure 11, respectively. As a result, the ν_e CC reaction rate is greater for NEQ-SI than for NEQ-FD. The flavor change of $\bar{\nu}_e$ partially occurs due to the MSW effect.

On the other hand, for the IH case, the $\bar{\nu}_e$ is fully converted to $\bar{\nu}_x$ by considering the ν-SI, and the subsequent MSW resonance converts the $\bar{\nu}_x$ back to $\bar{\nu}_e$. Therefore, the initial $\bar{\nu}_e$ spectrum recovers in the outer region. Due to the abundant $\bar{\nu}_e$, the abundances of ^{7}Li and ^{11}B increase compared to NEQ-FD, as shown in Figure 17(d). We note that the closer to the initial $\bar{\nu}_e$ spectrum, the more the abundances that are produced.

Finally, we summarize the whole yields as the masses integrated from $M_r \sim 1.6M_\odot$ to $\sim 6.0M_\odot$ at 50 s in Table 4. First, we discuss the dependence on the MH. For the light elements in HKC18 and KCK19, the MSW effects appear explicitly, regardless of the hydrodynamics model, if we note the increase (decrease) of the ^{7}Li and ^{11}B (^{7}Be and ^{11}C) abundances in the IH case compared to those in the NH case. But the heavy elements are less dependent on the MH. As already noted, the results from HKC18 are larger than those from KCK19.

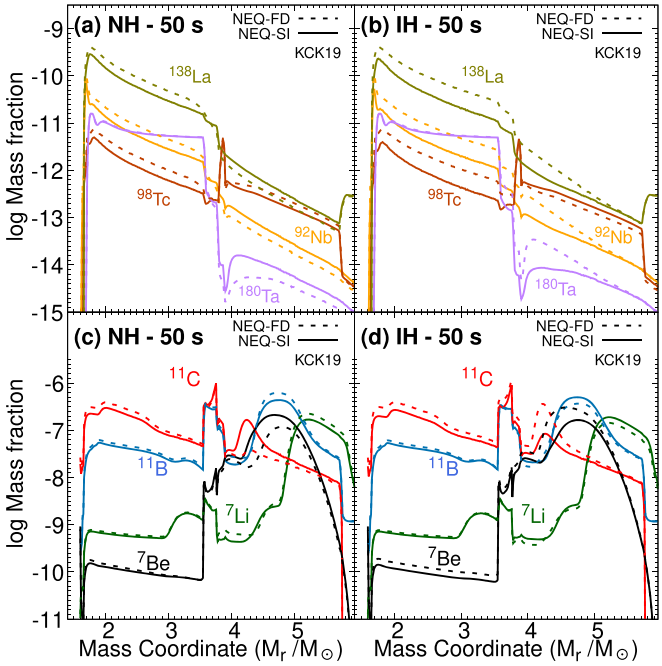

Figure 17. Panels (a) and (b) show the mass fractions of the heavy elements as a function of the mass coordinate at 50 s for NH and IH, respectively. Panels (c) and (d) denote the mass fractions of the light elements.

Second, the shock effect increases the ^{7}Be and ^{11}C in the NH case. This may indicate that the ν_e spectra are much more affected by the shock propagation than the $\bar{\nu}_e$ spectra.

Third, the SI effects show interesting features depending on the MH and the neutrino luminosity. For example, the results in the NEQ-FD case in the last row of Table 4 indicate the decrease (increase) of ^{7}Li and ^{11}B (^{7}Be and ^{11}C) in the IH case compared to the NH case, which is contrary to the KCK19 case with the EQ luminosity. In brief, the neutrino luminosity plays a vital role in the ν-process. However, if we include the ν-SI, the change of the light elements in the NEQ-SI case compensates for the differences, and the final abundances resemble the trend from KCK19. Therefore, the nuclear abundances sensitively depend not only on the MSW effect, but also on the ν-SI effect.

5.4. Yield Ratio of ^{7}Li to ^{11}B in Each Model

Here, we report the abundance ratios of some of the nuclei produced in the ν-process tabulated in the two rightmost columns of Table 4. The ratio might cancel the aforementioned model dependences in the respective nucleus yields.

Moreover, meteorite analysis data for the ratios provide important information about the ν-process abundances. In the following, we compare our results for the ratio with observational data from a Bayesian analysis of Silicon Carbide X (SiC X) grains. Here, we presumed that elements in the SiC X grains had been uniformly mixed, before condensing into the SN ejecta long before the solar system's formation. The

Table 4
Integrated Masses of the Nuclei after 50 s in the Mass Range M_r = 1.6–6 ($M_\odot$)

	MH	^{7}Li	^{7}Be	^{11}B	^{11}C	^{92}Nb	^{98}Tc	^{138}La	^{180}Ta	Yield Ratio	PF Ratio
			(10^{-7} $M_\odot$)			(10^{-12} $M_\odot$)		(10^{-11} $M_\odot$)		N(^{7}Li)/N(^{11}B)	^{138}La/^{11}B
FD EQ	NH	1.256	4.953	5.576	2.048	4.903	1.048	3.395	0.845	1.280	0.1288
(HKC18)	IH	1.496	1.461	7.141	1.218	4.760	1.112	3.267	0.843	0.556	0.1130
FD EQ	NH	0.861	2.428	2.480	2.139	4.551	1.180	3.760	1.016	1.119	0.2354
(KCK19)	IH	1.017	0.936	3.099	0.883	4.226	1.218	3.436	1.012	0.771	0.2495
FD EQ Shock	NH	0.861	1.904	2.546	1.701	4.973	1.271	4.164	1.017	1.023	0.2835
(KCK19)	IH	0.949	1.027	2.922	0.937	4.271	1.215	3.485	1.012	0.805	0.2611
SI EQ[a]	NH	0.861	2.428	2.480	2.139	4.551	1.180	3.760	1.016	1.119	0.2354
(KCK19)	IH	0.920	2.057	2.852	3.874	15.07	3.259	13.58	1.052	0.695	0.5838
SI NEQ	NH	1.132	1.601	4.276	4.920	16.44	3.559	15.19	1.295	0.467	0.4776
(KCK19)	IH	1.261	1.206	4.623	4.283	12.29	2.854	11.31	1.281	0.435	0.3672
FD NEQ	NH	1.483	0.841	5.407	5.258	25.44	5.367	23.14	1.323	0.342	0.6274
(KCK19)	IH	0.959	2.303	3.946	6.566	26.15	5.302	23.94	1.331	0.488	0.6585
SI NEQ Ko et al. (2020)	NH	1.643	3.347	9.332	6.138	17.92	3.511	14.29	1.363	0.507	0.2671
(HKC18)	IH	1.792	2.372	10.33	5.524	13.59	2.720	10.41	1.358	0.413	0.1899
FD NEQ Ko et al. (2020)	NH	2.400	1.860	12.46	7.080	27.56	5.361	22.62	1.349	0.343	0.335
(HKC18)	IH	1.640	5.270	8.382	7.804	27.83	5.318	22.94	1.353	0.671	0.410

Note. We use two hydrodynamics models (HKC18 and KCK19), two luminosity models (EQ and NEQ) and cases without the ν-SI (FD) and with the ν-SI (SI) for the NH and IH cases, meaning that the results for 12 different cases are tabulated. The last two results are quoted from our previous results. See the text for details.
[a] The same as the FD EQ (KCK19) NH result.

analysis of the SiC X grains constrains the ratio of ^{7}Li/^{11}B produced by the ν-process as -0.31 ± 0.42, and the upper limit is given by 0.53 under a 2σ error bar (Mathews et al. 2012). Based on the above assumption, we integrate the yields of ^{7}Li and ^{11}B over the whole mass region, after the decay of unstable nuclei, and present the yield ratio of ^{7}Li to ^{11}B, which is calculated as $N(\mathrm{Li})/N(\mathrm{B}) = (M_{^{7}\mathrm{Li}}/7)/(M_{^{11}\mathrm{B}}/11)$.

A previous study suggested that the abundance ratio ^{7}Li/^{11}B is sensitive to the MH (Yoshida et al. 2006). In our previous paper (Ko et al. 2020), the ^{7}Li/^{11}B ratio was changed as a result of the ν-SI effect from 0.671 to 0.413 in the IH case, and from 0.343 to 0.507 in the NH case. The ^{7}Li/^{11}B ratio in the NH case was larger than that in the IH case, by about 23%, which is shown in the last two rows of Table 4. However, when the KCK19 hydrodynamics model is adopted, the ratios are different from those of the HKC18 model. That is, the ratio is increased (decreased) in the NH (IH) case (see the results for SI NEQ and FD NEQ with KCK19 in Table 4). We note that the results for the HKC18 hydrodynamics in the last two rows (Ko et al. 2020) used an old pre-SN model (Blinnikov et al. 2000), while the others in the present work exploit the updated pre-SN model (Kikuchi et al. 2015), with KCK19 being explained in Figure 13.

On the other hand, when we adopt the EQ luminosity, the SI effect decreases the ratio from 0.771 to 0.695 in the IH case, while there is no change in the NH case. Therefore, the ν-SI turns out to depend on the luminosity and plays a vital role in understanding the light nuclear abundances. We note that the results using the EQ luminosity are not favorable for the meteorite data within the 2σ range (Mathews et al. 2012).

5.5. Production Factor Ratio of ^{138}La to ^{11}B for Each Model

Here, we discuss the production factor (PF) ratio of ^{138}La to ^{11}B (Heger & Woosley 2002), i.e., PF(^{138}La) to PF(^{11}B), where PF[A] $= X_A/X_{A\odot}$, with X_A and $X_{A\odot}$ defined as the mass fractions of A in the SN ejecta and in the solar system, respectively. The previous study of the ν-process without considering both the ν-SI and MSW effects (Heger et al. 2005) concluded that enough ^{138}La was produced by the ν-process, while the ^{11}B was overproduced. Our previous study showed that the ^{138}La abundance was decreased by a factor of about 2, whereas the ^{11}B abundance was nearly unaffected by the ν-SI (Ko et al. 2020). By using the KCK19 hydrodynamics, this trend is still apparent for ^{11}B and ^{138}La. We present the PF ratio for each case in the last column of Table 4. These results used a normalization to ^{16}O. (PF ratios normalized to other nuclei are also presented in Tables 11, 12, and 13 in Appendix E.)

In particular, for the two different hydrodynamics models with NEQ-SI, the ratio of the PF is approximately 0.2671 (NH) and 0.1899 (IH) for HCK18, and 0.4776 (NH) and 0.3672 (IH) for KCK19. The results indicate that the ratio for the NH case is larger than that for the IH case, by factors of about 1.4 and 1.3 for the respective models. This difference comes from the fact that ^{138}La is predominantly produced by ν_e, but ^{11}B production is less sensitive to the ν-SI, as discussed above.

The ratio can be compared with the expected value $\mathrm{R}_{ex} = f_{\mathrm{metal}} f_{La}^{SN}/f_{B}^{SN}$. Here, f_{metal} is the metallicity used in this work, which roughly scales as the abundance of ^{138}Ba, the seed of ^{138}La in the ν-process. The quantity $f_{La}^{SN} \sim 1$ is the fraction of the solar system abundance of ^{138}La originating from the SN, while f_{B}^{SN} is the fraction of ^{11}B originating from the SN, which is deduced to be $0.41^{+0.21}_{-0.42}$ from the observed isotopic ratio of $^{11}\mathrm{B}/^{10}\mathrm{B} = (0.7 \pm 0.1)/(0.3 \pm 0.1)$ for cosmic-ray yields (Silberberg & Tsao 1990), and $^{11}\mathrm{B}/^{10}\mathrm{B} = 3.98$ for the solar abundance ratio (Liu et al. 2010). From these values, the ratio is $\mathrm{R}_{ex} = 0.41\ ^{+\infty}_{-\infty}$. Our theoretical values are 0.2671–0.4776 for the NH and 0.1899–0.3672 for the IH cases, where the former values (0.2671 and 0.1899) come from

Table 5
Integrated Masses for the FDSI NEQ (KCK19) Case, Which is the Case of Complete Matter Suppression of the Collective Neutrino Oscillation During the Accretion Phase ($t_{pb} < 0.5s$), Represented by the FD Distribution and the Collective Oscillation during the Cooling Phase ($t_{pb} > 0.5s$), Whose Neutrino Distribution is Changed by the SI

Hierarchy	Mass	^{7}Li	^{7}Be	^{11}B	^{11}C	^{92}Nb	^{98}Tc	^{138}La
		($10^{-7}\,M_{\odot}$)			($10^{-12}\,M_{\odot}$)		($10^{-11}\,M_{\odot}$)	
FDSI NEQ	NH	1.131	1.601	4.275	4.887	16.73	3.600	15.47
(KCK19)	IH	1.261	1.206	4.622	4.242	12.80	2.927	11.89
Difference (%)	NH	0.09	0.00	0.02	0.67	1.76	1.15	1.84
	IH	0.00	0.00	0.02	0.96	4.15	2.56	5.13

Note. The difference is the change of the element abundances of the FDSI NEQ case compared to that of the SI NEQ (KCK19) case in Table 4. The others are the same as Table 4. See the text for details.

HKC18 and the latter from KCK19. Consequently, the ^{138}La/^{11}B ratio is more consistent with the NH case within 1σ.

This trend originates from the fact that the abundance change due to the ν-SI in the IH case is larger than that in the NH case. After the ν-SI, the ν_e-flux in the NH case is higher than that in the IH case by a factor of 2–3 (see Figures 12 and 11) in the energy range appropriate to ^{138}La production (10–20 MeV). As discussed previously, ^{138}La production depends strongly on the ν_e-flux. Thus, even if the initial neutrino energy spectra are changed from those assumed here, the trend is expected to be preserved, so that the PF(^{138}La)/PF(^{11}B) ratio including the ν-SI effect in the NH case is higher than that in the IH case. This implies that the NH scheme is favorable for explaining the empirical ratio. For comparison, we note that the results of the EQ luminosity case are 0.2354 (NH) and 0.5838 (IH).

6. Summary and Conclusion

6.1. Summary

In this work, we have investigated the multifaceted features of the ν-process of the CCSN resulting from the choice of various physics models. First, we updated the hydrodynamics model from HKC18 to KCK19. The density, temperature, and radius in the former case are a bit larger than those in the latter. Due to these differences, the MSW resonance region of HKC18 occurs around $M_r \sim 4M_{\odot}$, whereas that of KCK19 appears around $M_r \sim 3.7\,M_{\odot}$ for $E_{\nu} = 15$ MeV. In addition, the nuclear abundances in the HKC18 model were generally larger than those of KCK19. However, both models have similar production patterns to each other.

For the neutrino reactions, we have adopted the results from the SM and QRPA calculations tabulated in Appendix C.2, which have been shown to properly account for the available data related to the neutrino-induced reactions on the relevant nuclei. Other nuclear reaction rates are taken from the JINA REACLIB database (Cyburt et al. 2010). Since the (n, γ) reactions turn out to be important for the ν-process, we have also utilized recent (n, γ) reaction calculations developed via the Monte Carlo method (see Appendix C.1).

Second, we investigated the MSW effect in the outer region. The different hydrodynamics models show the shift of the MSW resonance region. As a result, the light element abundances are increased outside the MSW resonance region, while the heavy element abundances are less affected by the MSW resonance.

Third, we examined the shock propagation effect peculiar to the CCSN. We found a neutrino flavor change resonance around $M_r \sim 1.6M_{\odot}$ due to the shock effect. Most of the neutrino spectra go back to the initial neutrino flux at the resonance. But the neutrino luminosities are exponentially decreasing as a function of time. Thus, the nuclear abundances are less affected by the shock effect than by the SI effect. The heavy elements maximally increased by about 17% (1.1%) for the NH (IH) case, respectively. The light elements were further changed, by 32%(11%) maximally for the NH (IH) case, respectively.

Fourth, we analyzed the effects of the neutrino luminosity on the element abundances. The neutrino luminosity was deduced from recent simulations of the neutrino transport model for five post-bounce time intervals. We adopted the results in O'Connor et al. (2018), which compared six CCSN simulations and provided the luminosities and averaged energies of the neutrinos emitted from the neutrino sphere. In particular, the neutrino SI strongly hinges on the neutrino luminosity and the neutrino sphere radius, depending on the adopted SN simulation model. We termed this NEQ luminosity, and studied the SI effect in detail, in comparison to the results from the EQ luminosity model.

We used a multi-angle approach to derive the SI effect in the ν-oscillation. The spectra of the neutrinos emitted from the neutrino sphere are modified by the ν-SI. In this study, we investigated two different neutrino luminosities, EQ and NEQ. When we adopt the EQ luminosity, the ν-SI effect shows only in the IH case, where a neutrino splitting phenomenon occurs around $E_{\nu} \sim 10$ MeV. Below this energy, the neutrino spectra remain as the initial ν_e, and the ν_e spectra above the energy follow the initial ν_x spectra (Figure 9). As a result, inside the MSW resonance region, nuclear abundances are increased by the ν-process. In particular, heavy nuclear abundances display this trend.

On the other hand, the ν-SI effect with NEQ luminosity appears for both MHs. At the initial propagation, the ν-SI effect in the IH case is analogous to that in the EQ luminosity case. The difference is that the ν_x luminosity decreases faster than that of the ν_e with the time evolution. Therefore, the changed ν_e spectra have lower values above the splitting energy $E_{\nu} \sim 5$–7 MeV (Figure 12). These lead to the decrease of the neutrino CC reaction from the MSW effect, which affects the light element synthesis. In the NH case, the splitting phenomenon is less clear than in the IH case. But, for the same reason as before, the neutrino CC reactions are decreased by the SI effect.

Finally, we discussed the ratio of $N(^{7}\mathrm{Li})/N(^{11}\mathrm{B})$ and PF(^{138}La)/PF(^{11}B) by using the final abundance results tabulated in Table 4. The present results for both ratios imply that the NH

case is favored by more advanced models; that is, the NEQ-SI luminosity model using KCK19 hydrodynamics.

6.2. Conclusion

In conclusion, (1) the elemental abundances produced by the ν-process strongly depend on the hydrodynamics model and the pre-SN model. (2) The shock propagation effects are not as large as other effects, but they maximally give a 22% difference for a specific nucleus abundance. (3) MSW effects are still important for understanding the yield differences between the light and heavy element abundances. (4) The neutrino luminosity is more important than other factors in the ν-process, which are critically sensitive to the neutrino transport model and its simulation. (5) The ratio of some specific nuclei, like $N(^7\mathrm{Li})/\mathrm{N}(^{11}\mathrm{B})$ and $\mathrm{PF}(^{138}\mathrm{La})/\mathrm{PF}(^{11}\mathrm{B})$, could be valuable indicators of the ν-process, because they are less sensitive to the models exploited in the ν-process calculations. (6) Our systematic calculations support the nucleosynthesis results for the NH neutrino MH. (7) We remind the reader that the neutrino sphere radius $\sim$10 km and the power-law density profile could differ from the SN simulations. The increase of the neutrino sphere during the accretion phase may lead to the complete suppression of the collective neutrino oscillation. Therefore, we tested the case of complete matter suppression for the collective neutrino oscillation during the accretion phase and the collective oscillation during the cooling phase, termed FDSI NEQ. The results are presented in Table 5. The difference turns out to be less than 5% maximally. This means that the uncertainty from the neutrino sphere radius and the power-law density profile during the accretion phase can be retained within the 5% level.

Finally, we note that recent 3D hydrodynamical SN simulations predicted asymmetric radiations of ν_e and $\bar{\nu}_e$ (Nagakura et al. 2021). Subsequent studies, taking the neutrino angular distribution into account, suggest that the different angular distributions of ν_e and $\bar{\nu}_e$ cause a fast neutrino flavor transformation, due to the crossing of ν_e and $\bar{\nu}_e$. Other symmetry violations, due to the asymmetric flux and the convection layer, can cause a fast flavor conversion compared to the flavor change due to the matter effect (Abbar et al. 2019; Glas et al. 2020). It may occur in the CCSN, and affect the neutrino observation (Dasgupta et al. 2017; Tamborra et al. 2017) and the diffuse SN neutrino background (Mirizzi et al. 2016). In this case, the energy exchange may occur earlier and bring about the larger differences in the luminosities between ν_e and ν_x. A hypothetical sterile neutrino may also cause such a fast neutrino flavor change (Ko et al. 2020). This can enhance the MH dependence of the ν-process abundances. In other words, the constraints from the analysis of the elemental abundances for the ν-process can be a good test bed for evaluating the many interesting facets in the present neutrino physics model. However, for more definite conclusions, detailed ν-process calculations should involve realistic neutrino emission models in CCSNe, with more precise evaluations of the fast neutrino conversion effects, as well as advanced models beyond the standard model. We leave them for future works.

This work was supported by the National Research Foundation of Korea (grant Nos. NRF-2021R1A6A1A03043957, NRF-2020K1A3A7A09080134, and NRF-2020R1A2C3006177). This work was supported by grants-in-aid for Scientific Research from JSPS (17K05459 and 20K03958). The work of D.J. is supported by the Institute for Basic Science under IBS-R012-D1. M.K. was supported by the NSFC Research Fund (grant No. 11850410441). The work of G.J.M. was supported in part by DOE nuclear theory grant DE-FG02-95-ER40934 and in part by the visitor program at NAOJ.

Appendix A
The Neutrino Field and Total Hamiltonian for CC Interaction

We introduce the neutrino field, which can be expressed in a finite volume to describe one-particle states with appropriate normalization. In a box with width L and momentum $\boldsymbol{p} = (2\pi/L)\boldsymbol{n}$ (where n is an integer), continuum states can be discretized as $(Vd^3\boldsymbol{p})/(2\pi)^3 \rightarrow \sum_{\boldsymbol{p}}$ and $(2\pi)^3\delta^3(\boldsymbol{p}-\boldsymbol{p}') \rightarrow V\delta_{\Gamma\Gamma'}$, with the volume $V = L^3$ (Giunti & Chung 2007; Sigl 2017). Then, the field operator for the left-hand neutrino $\nu_\alpha(\alpha = e, \mu, \tau)$ is quantized as follows:

$$\nu_{\alpha L}(x) = \sum_{\boldsymbol{p}} \frac{1}{2E_p V}(\hat{a}_{\nu_\alpha}(\boldsymbol{p})u^{(-)}(p)e^{-ip\cdot x} + \hat{b}^\dagger_{\nu_\alpha}(\boldsymbol{p})v^{(+)}(p)e^{+ip\cdot x}), \tag{A1}$$

where $u^{(-)}(p)$ and $v^{(+)}(p)$ are spinors of the particle with negative helicity and the antiparticle with positive helicity. The operators $\hat{a}_{\nu_\alpha}(\boldsymbol{p})$ and $\hat{a}^\dagger_{\nu_\alpha}(\boldsymbol{p})$ are annihilation and creation operators, respectively, for ν_α, and $\hat{b}_{\nu_\alpha}(\boldsymbol{p})$ and $\hat{b}^\dagger_{\nu_\alpha}(\boldsymbol{p})$ for $\bar{\nu}_\alpha$. The dispersion relation for neutrinos in free space is given as $E_p = |\boldsymbol{p}|$. Here, we normalize the anticommutation relation of the operators as $\{a_{\nu_\alpha}(\boldsymbol{p}), a^\dagger_{\nu_\alpha}(\boldsymbol{p}')\} = \{b_{\nu_\alpha}(\boldsymbol{p}), b^\dagger_{\nu_\alpha}(\boldsymbol{p}')\} = 2E_pV\delta_{\Gamma\Gamma'}$. As a result, the neutrino and antineutrino states are expressed as $|\nu_\alpha(\boldsymbol{p})\rangle = 1/\sqrt{2E_pV}\,a^\dagger_{\nu_\alpha}(\boldsymbol{p})|0\rangle$ and $|\bar{\nu}_\alpha(\boldsymbol{p})\rangle = 1/\sqrt{2E_pV}\,b^\dagger_{\nu_\alpha}(\boldsymbol{p})$, where $|0\rangle$ is the vacuum for the neutrino field.

For the CC interaction, the Hamiltonian density $\mathcal{H}^{CC}$ between the neutrinos and the background leptons is written as follows:

$$\mathcal{H}^{CC}_{\nu_l l}(x) = 2\sqrt{2}\,G_F[\bar{\nu}_{lL}(x)\gamma^\lambda\nu_{lL}(x)] \times [\bar{l}_L(x)\gamma_\lambda l_L(x)], \tag{A2}$$

where G_F is the Fermi constant describing the effective interaction strength and l stands for the leptons, such as an electron, muon, and tau, respectively. The subscript L means the left-hand projection of the neutrino field defined by $\nu_{lL}(x) \equiv (1-\gamma^5)/2\,\nu_l(x)$, in which we follow the conventions of $\bar{\nu}_{lL}(x) \equiv \nu^\dagger_{lL}(x)\gamma^0$ and $\gamma_5 \equiv \gamma^5 \equiv i\gamma^0\gamma^1\gamma^2\gamma^3$.

By taking the thermal average to the electron background, the effective Hamiltonian density is reduced to $\mathcal{H}^{CC}_{\mathrm{eff}}(x) = \sqrt{2}\,G_F n_e \nu^\dagger_{eL}(x)\nu_{eL}(x)$ (Giunti & Chung 2007), and the effective potential for the CC interaction is given by

$$\hat{\mathcal{V}}_{\nu_e e} = \int \mathrm{d}^3x\ \mathcal{H}^{CC}_{\mathrm{eff}}(x) = \sqrt{2}\,G_F n_e \sum_{\boldsymbol{p}} \frac{[a^\dagger_{\nu_e}(\boldsymbol{p})a_{\nu_e}(\boldsymbol{p}) - b^\dagger_{\nu_e}(\boldsymbol{p})b_{\nu_e}(\boldsymbol{p})]}{2E_pV}, \tag{A3}$$

where $a_{\nu_e}(a^\dagger_{\nu_e})$ and $b_{\nu_e}(b^\dagger_{\nu_e})$ are annihilation (creation) operators of ν_e and $\bar{\nu}_e$. E_p and V denote the energy of the neutrinos and the volume with a factor of $(2\pi)^3$. These quantities come from the second quantization of $\nu_{eL}(x)$ in Equation (A1). Because of

the charge neutrality condition, the net electron density is given by $n_e = \rho_b N_A Y_e$, where ρ_b, N_A, and Y_e are the baryon density, Avogadro's number, and the electron fraction, respectively. The matrix components of the MSW matter potential are derived from $\langle\nu_\beta(\boldsymbol{p})|\hat{\mathcal{V}}_{\nu_e e}|\nu_\alpha(\boldsymbol{p})\rangle(\alpha, \beta = e, \mu, \tau)$ in Equation (A3).

Appendix B
Potential for the Neutrino SI

The Hamiltonian density for the neutrino SI is given as Equation (6). Similar to the derivation of the effective Hamiltonian in Equation (A3), the one-body effective Hamiltonian for the neutrino SI is given by the average of the neutrino background. We introduce the average of the neutrino operators (Sigl & Raffelt 1993; Volpe et al. 2013),

$$\langle a^\dagger_{\nu_\alpha}(\boldsymbol{p}')a_{\nu_\beta}(\boldsymbol{p})\rangle = 2E_p V\delta_{\Gamma\Gamma'} f_{\rm dist}(t, \boldsymbol{p})\rho_{\beta\alpha}(t, \boldsymbol{p}), \tag{B1}$$

$$\langle b^\dagger_{\nu_\alpha}(\boldsymbol{p}')b_{\nu_\beta}(\boldsymbol{p})\rangle = 2E_p V\delta_{\Gamma\Gamma'} \bar{f}_{\rm dist}(t, \boldsymbol{p})\bar{\rho}_{\alpha\beta}(t, \boldsymbol{p}), \tag{B2}$$

where $f_{\rm dist}$ ($\bar{f}_{\rm dist}$) and $\rho(\bar{\rho})$ are the normalized distribution and the density matrix of the neutrinos (antineutrinos), respectively. Here, we normalize the traces of the matrices, $\sum_\alpha \rho_{\alpha\alpha}(t, \boldsymbol{p}) = \sum_\alpha \bar{\rho}_{\alpha\alpha}(t, \boldsymbol{p}) = 1$, thus the average of the neutrino background is given by

$$\begin{aligned}
&\langle\bar{\nu}_{\alpha L}(x)\gamma^\mu\nu_{\beta L}(x)\rangle \\
&= \sum_{\boldsymbol{q}\boldsymbol{q}'} \frac{\bar{u}^{(-)}(q')\gamma^\mu u^{(-)}(q)\langle a^\dagger_{\nu_\alpha}(\boldsymbol{q}')a_{\nu_\beta}(\boldsymbol{q})\rangle e^{i(q'-q)\cdot x} - \bar{v}^{(+)}(q')\gamma^\mu v^{(+)}(p)e^{-i(q'-q)\cdot x}\langle b^\dagger_{\nu_\beta}(\boldsymbol{q})b_{\nu_\alpha}(\boldsymbol{q}')\rangle}{(2E_q V)(2E_{q'}V)} \\
&= \frac{1}{V}\sum_{\boldsymbol{q}} \frac{q^\mu}{E_q}[f_{\rm dist}(t, \boldsymbol{q})\rho_{\beta\alpha}(t, \boldsymbol{q}) - \bar{f}_{\rm dist}(t, \boldsymbol{q})\bar{\rho}_{\beta\alpha}(t, \boldsymbol{q})],
\end{aligned} \tag{B3}$$

where the averages of the expectation values of $\langle a^\dagger b^\dagger\rangle$ and $\langle ba\rangle$ are ignored. Without flavor mixing between neutrinos and antineutrinos, the diagonal term in Figure 7 does not contribute to the neutrino oscillations. Therefore, the effective Hamiltonian for the neutrino SI is written as

$$\begin{aligned}
\hat{\mathcal{V}}_{\nu\nu} = \frac{G_F}{\sqrt{2}}\int d^3x\ &[\bar{\nu}_{\beta L}(x)\gamma^\mu\nu_{\alpha L}(x)] \\
&\times 2\langle\bar{\nu}_{\alpha L}(x)\gamma^\mu\nu_{\beta L}(x)\rangle.
\end{aligned} \tag{B4}$$

Finally, Equation (7) is derived from Equations (B4), (B3), and (A1). The number density of the neutrino background term, $\frac{d^3\boldsymbol{q}}{(2\pi)^3} f_{\rm dist}(t, \boldsymbol{q}) = \sum_\eta dn_{\nu_\eta}$, depends on the angle between the neutrinos. We follow the uniform and isotropic neutrino emission model, which is called the bulb model, as described in Duan et al. (2006). The differential neutrino number density can be written as

$$\begin{aligned}
dn_{\nu_\eta} = &\frac{L_{\nu_\eta}}{\pi R_\nu^2}\frac{1}{\langle E_{\nu_\eta}\rangle}\frac{1}{(T_{\nu_\eta})^3 F_2(0)} \\
&\times \frac{E_q^2 dE_q}{\exp(E_q/T_{\nu_\eta}) + 1}\left(\frac{d\Omega_q}{\int d\Omega_q}\right),
\end{aligned} \tag{B5}$$

where $\left(\frac{d\Omega_q}{\int d\Omega_q}\right) = \frac{d(\cos\theta_q)d\phi_q}{4\pi}$. Here, we assume a cylindrical symmetry along the z-axis, so that the integration of only the ϕ_q direction is done as $\int_0^{2\pi}(1 - \hat{\boldsymbol{p}}\cdot\hat{\boldsymbol{q}})d\Omega_q = 2\pi(1 - \cos\theta_p\cos\theta_q)d(\cos\theta_q)$. Finally, the potential for the neutrino SI in the Schrödinger-like equation is described by

$$\begin{aligned}
\mathcal{V}_{\nu\nu} = \sqrt{2}G_F\int\Bigg[&\sum_{\eta=e,\mu,\tau}\frac{L_{\nu_\eta}}{2\pi R_\nu^2}\frac{1}{\langle E_{\nu_\eta}\rangle}\frac{1}{(T_{\nu_\eta})^3F_2(0)} \\
&\times\frac{E_q^2}{\exp(E_q/T_{\nu_\eta}) + 1}\rho(r, E_q, \theta_q) \\
&- \sum_{\eta=e,\mu,\tau}\frac{L_{\bar{\nu}_\eta}}{2\pi R_\nu^2}\frac{1}{\langle E_{\bar{\nu}_\eta}\rangle}\frac{1}{(T_{\bar{\nu}_\eta})^3F_2(0)} \\
&\times\frac{E_q^2}{\exp(E_q/T_{\bar{\nu}_\eta}) + 1}\bar{\rho}(r, E_q, \theta_q)\Bigg] \\
&\times(1 - \cos\theta_p\cos\theta_q)dE_q d(\cos\theta_q).
\end{aligned} \tag{B6}$$

In the case of single-angle approximation, the propagation angle θ_p is not considered, as a result of which the integration is given as:

$$\begin{aligned}
&\int_0^{\theta_{\rm max}}(1 - \cos\theta_q)\sin\theta_q d\theta_q \\
&= \frac{1}{2}(1 - \cos\theta_{\rm max})^2 = \frac{1}{2}\left(1 - \sqrt{1 - \left(\frac{R_\nu}{r}\right)^2}\right)^2,
\end{aligned} \tag{B7}$$

where the possible maximum angle of the emitted background neutrino is given as $\sin\theta_{\rm max} = \frac{R_\nu}{r}$, r is the radius from the center of the core, and the emission follows the tangential direction of the neutrino sphere. This single-angle approximation is appropriate when r is large enough.

Appendix C
Reaction Data

In the present calculation, we have exploited updated nuclear reaction rates related to the ν-process from the JINA database (Cyburt et al. 2010). But parts of them, such as the neutron capture, photonuclear reaction, and neutrino-induced reactions, are different from the JINA database. In the following, we present the numerical results of the updated nuclear reactions in detail.

Table 6
Forward (n, γ) Reactions and Temperature Parameters

Reaction	JINA Database Parameters						
	a_0	a_1	a_2	a_3	a_4	a_5	a_6
^{84}Sr (n, γ)^{85} Sr	1.248898E+01	2.370158E-02	−2.452547E+00	7.664219E+00	−4.995054E-01	2.502527E-02	−2.778081E+00
^{85}Sr (n, γ)^{86} Sr	1.608127E+01	5.866922E-04	1.163815E-01	−4.176012E-02	1.914001E-02	−5.292960E-03	−1.787551E-01
^{86}Sr (n, γ)^{87} Sr	1.005771E+01	2.481909E-02	−2.949004E+00	9.353030E+00	−5.609058E-01	2.291346E-02	−3.463590E+00
^{88}Y (n, γ)^{89}Y	1.673954E+01	3.646441E-03	−1.878931E-01	8.603386E-01	−1.382795E-01	8.356414E-03	−3.971826E-01
^{89}Y (n, γ)^{90}Y	9.051425E+00	1.395434E-02	−2.159787E+00	8.338274E+00	−5.464776E-01	2.700101E-02	−2.933181E+00
^{88}Zr (n, γ)^{89} Zr	7.946674E+00	2.684651E-02	−3.545765E+00	1.208552E+01	−7.999320E-01	3.881745E-02	−4.307062E+00
^{90}Zr (n, γ)^{91} Zr	1.260702E+01	−8.700704E-03	4.592438E-01	1.303912E+00	1.371825E-01	−2.291362E-02	−2.587433E-01
^{91}Nb (n, γ)^{92} Nb	1.590488E+01	1.147514E-02	−1.074272E+00	1.982728E+00	8.122271E-02	−1.900906E-02	−1.176654E+00
^{92}Nb (n, γ)^{93} Nb	1.452824E+01	9.406627E-03	−1.076378E+00	3.107980E+00	−2.343066E-01	1.445819E-02	−1.371316E+00
^{93}Nb (n, γ)^{94} Nb	1.345852E+01	2.241971E-02	−2.521347E+00	6.419594E+00	−3.573849E-01	9.647026E-03	−2.719755E+00
^{92}Mo (n, γ)^{93} Mo	1.057350E+01	1.980617E-02	−2.623842E+00	8.157561E+00	−3.182821E-01	1.101292E-03	−3.138314E+00
^{93}Mo (n, γ)^{94} Mo	1.694178E+01	1.375932E-02	−1.233149E+00	1.468402E+00	1.885581E-01	−3.051284E-02	−1.134859E+00
^{94}Mo (n, γ)^{95} Mo	7.382442E+00	3.701772E-02	−4.788892E+00	1.462631E+01	−1.019866E+00	5.446624E-02	−5.436827E+00
^{95}Tc (n, γ)^{96} Tc	1.472420E+01	1.699289E-02	−1.911592E+00	4.739958E+00	−3.251417E-01	1.411674E-02	−2.073607E+00
^{97}Tc (n, γ)^{98} Tc	1.521961E+01	1.513890E-02	−1.715202E+00	4.216543E+00	−3.616674E-01	1.916291E-02	−1.844236E+00
^{98}Tc (n, γ)^{99} Tc	2.171829E+01	5.139517E-03	8.927720E-02	−4.932672E+00	4.558193E-01	−3.258772E-02	7.150464E-01
^{99}Tc (n, γ)^{100} Tc	1.831816E+01	1.330489E-02	−1.174862E+00	1.101243E+00	−3.004754E-02	−2.700345E-03	−8.823261E-01
^{96}Ru (n, γ)^{97} Ru	9.533413E+00	4.251006E-02	−5.004759E+00	1.342078E+01	−8.266547E-01	3.943924E-02	−5.272868E+00
^{98}Ru (n, γ)^{99} Ru	8.495533E+00	3.960303E-02	−4.832171E+00	1.427723E+01	−1.056089E+00	5.999115E-02	−5.321814E+00

Table 7
Inverse (γ, n) Reactions and Temperature Parameters

Reaction	JINA Database Parameters						
	a_0	a_1	a_2	a_3	a_4	a_5	a_6
^{85}Sr (γ, n)^{84} Sr	2.941888E+01	−1.001321E+02	2.493498E+01	−1.485769E+01	2.750941E-01	−2.923625E-03	1.345984E+01
^{86}Sr (γ, n)^{85} Sr	4.323333E+01	−1.325321E+02	−2.101852E+01	1.989032E+01	−8.112554E-01	3.261639E-02	−1.076570E+01
^{87}Sr (γ, n)^{86} Sr	2.689858E+01	−9.802114E+01	−1.165699E+00	1.267696E+01	−9.167931E-01	4.833428E-02	−2.413698E+00
^{89}Y (γ, n)^{88}Y	4.151676E+01	−1.333624E+02	5.217288E+00	−4.102714E+00	5.340280E-02	6.013768E-04	4.170938E+00
^{90}Y (γ, n)^{89}Y	3.120161E+01	−1.339622E+02	1.720268E+01	−8.732321E+00	1.194352E-01	−1.559901E-03	9.271344E+00
^{89}Zr (γ, n)^{88} Zr	2.642602E+01	−8.007789E+01	7.131969E+00	5.421843E+00	−6.738864E-01	3.952511E-02	2.308722E+00
^{91}Zr (γ, n)^{90} Zr	4.201612E+01	−1.058214E+02	−5.260266E+01	4.610917E+01	−1.525340E+00	4.487688E-02	−2.750847E+01
^{92}Nb (γ, n)^{91} Nb	3.599003E+01	−9.091540E+01	−2.039827E+01	2.501031E+01	−1.094619E+00	4.416519E-02	−1.212790E+01
^{93}Nb (γ, n)^{92} Nb	4.245298E+01	−1.027860E+02	1.145714E+01	−1.381590E+01	6.881836E-01	−3.694381E-02	8.814094E+00
^{94}Nb (γ, n)^{93} Nb	3.064462E+01	−8.423374E+01	2.103344E+00	8.803124E+00	−7.872117E-01	4.469467E-02	−4.897477E-01
^{93}Mo (γ, n)^{92} Mo	3.213648E+01	−9.263918E+01	−2.984683E+01	3.589655E+01	−1.549057E+00	6.000635E-02	−1.784346E+01
^{94}Mo (γ, n)^{93} Mo	3.932353E+01	−1.110093E+02	−3.845938E+01	4.237102E+01	−1.777939E+00	7.074719E-02	−2.260765E+01
^{95}Mo (γ, n)^{94} Mo	2.555338E+01	−8.712851E+01	3.671438E+01	−2.290833E+01	4.379981E-01	−6.649467E-03	1.940762E+01
^{96}Tc (γ, n)^{95} Tc	3.595634E+01	−9.160394E+01	3.915321E+00	1.194696E+00	−2.927797E-01	1.865394E-02	2.242460E+00
^{98}Tc (γ, n)^{97} Tc	3.673426E+01	−8.480618E+01	6.191082E+00	−1.572013E+00	−2.188507E-01	1.784643E-02	3.732824E+00
^{99}Tc (γ, n)^{98} Tc	4.255113E+01	−1.040263E+02	−3.006118E+00	1.711734E+00	−3.671844E-02	1.554448E-03	−5.663074E-01
^{100}Tc (γ, n)^{99} Tc	3.943086E+01	−7.846703E+01	−4.985715E+00	9.194351E+00	−5.917306E-01	3.360030E-02	−2.833361E+00
^{97}Ru (γ, n)^{96} Ru	2.504405E+01	−9.585048E+01	3.673857E+01	−2.135974E+01	3.905580E-01	−5.503320E-03	1.882684E+01
^{99}Ru (γ, n)^{98} Ru	2.843891E+01	−8.875171E+01	5.316734E+01	−4.184288E+01	1.290534E+00	−4.610888E-02	2.988585E+01

C.1. (n, γ) and (γ, n) Reaction Rates in the A ∼100 Region

First, the neutron capture reactions turned out to play important roles around the MSW region. For example, the valley in the ^{98}Tc abundance is sensitive to the (n, γ) reactions. Therefore, we used the newly updated calculations by Kawano et al. (2010), in which the local systematics of the Hauser–Feshbach model parameters were carefully investigated to infer the theoretical predictions for nuclear reactions of the relevant unstable nuclei, to obtain realistic abundances after the weak s-process. The updated (n, γ) and (γ, n) reaction data and those from the JINA database are presented in Figures 18 and 19, respectively. The new parameters for the temperature dependence utilized in the JINA database (Cyburt et al. 2010) are obtained from the new reaction rate functions and tabulated in Tables 6 and 7, for (n, γ) and (γ, n) reactions, respectively.

C.2. Neutrino-induced Reaction Cross-sectional Data

We tabulate the neutrino-induced reactions for $A \sim 92$, 98, 138, and 180 nuclei via NC and CC currents in Tables 8 and 9. These are calculated from the QRPA, which includes all the pairing interactions through the Brückner G-matrix evaluated from the charge dependent Bonn potential (Cheoun et al. 2010).

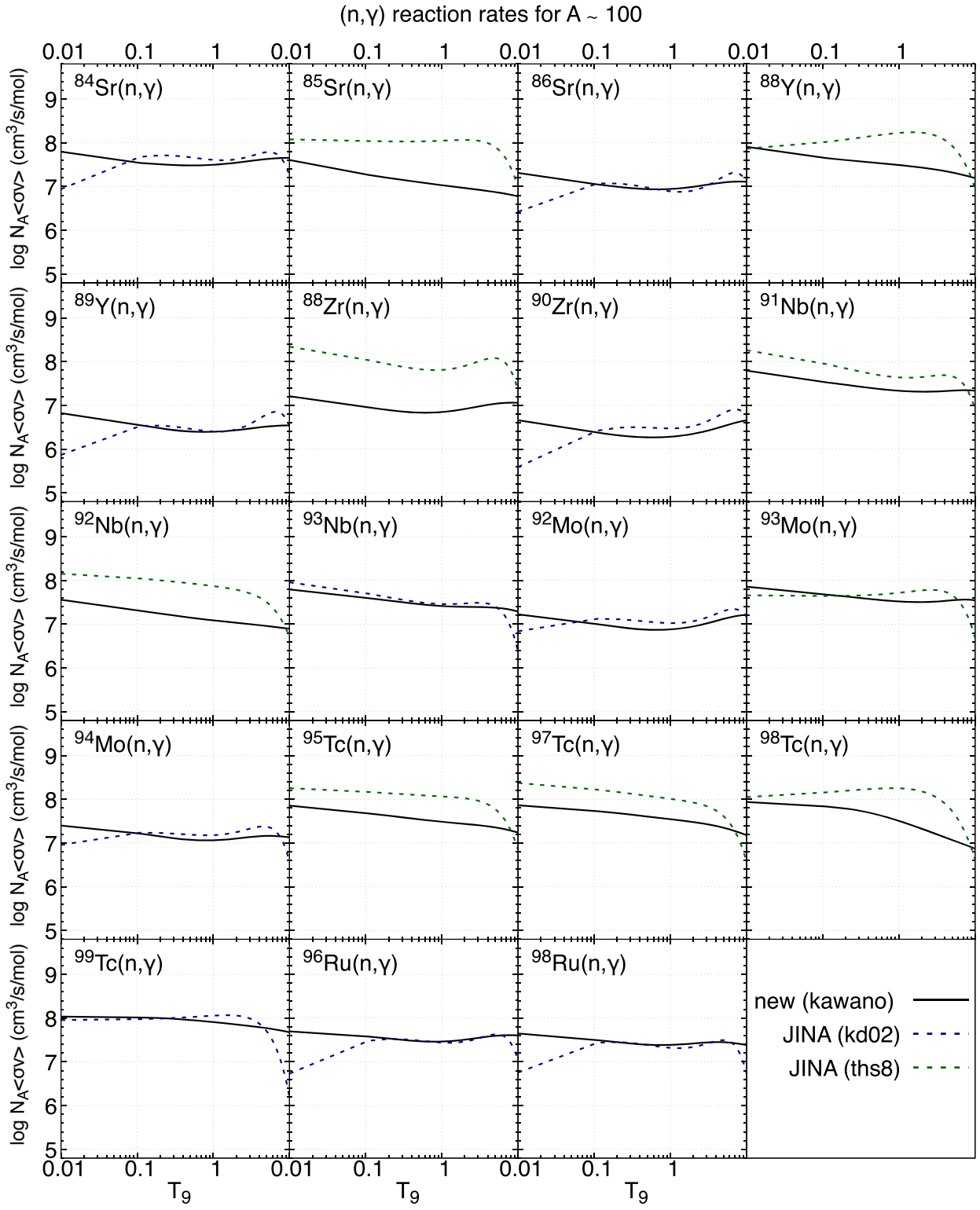

Figure 18. Forward (n, γ) reaction rates.

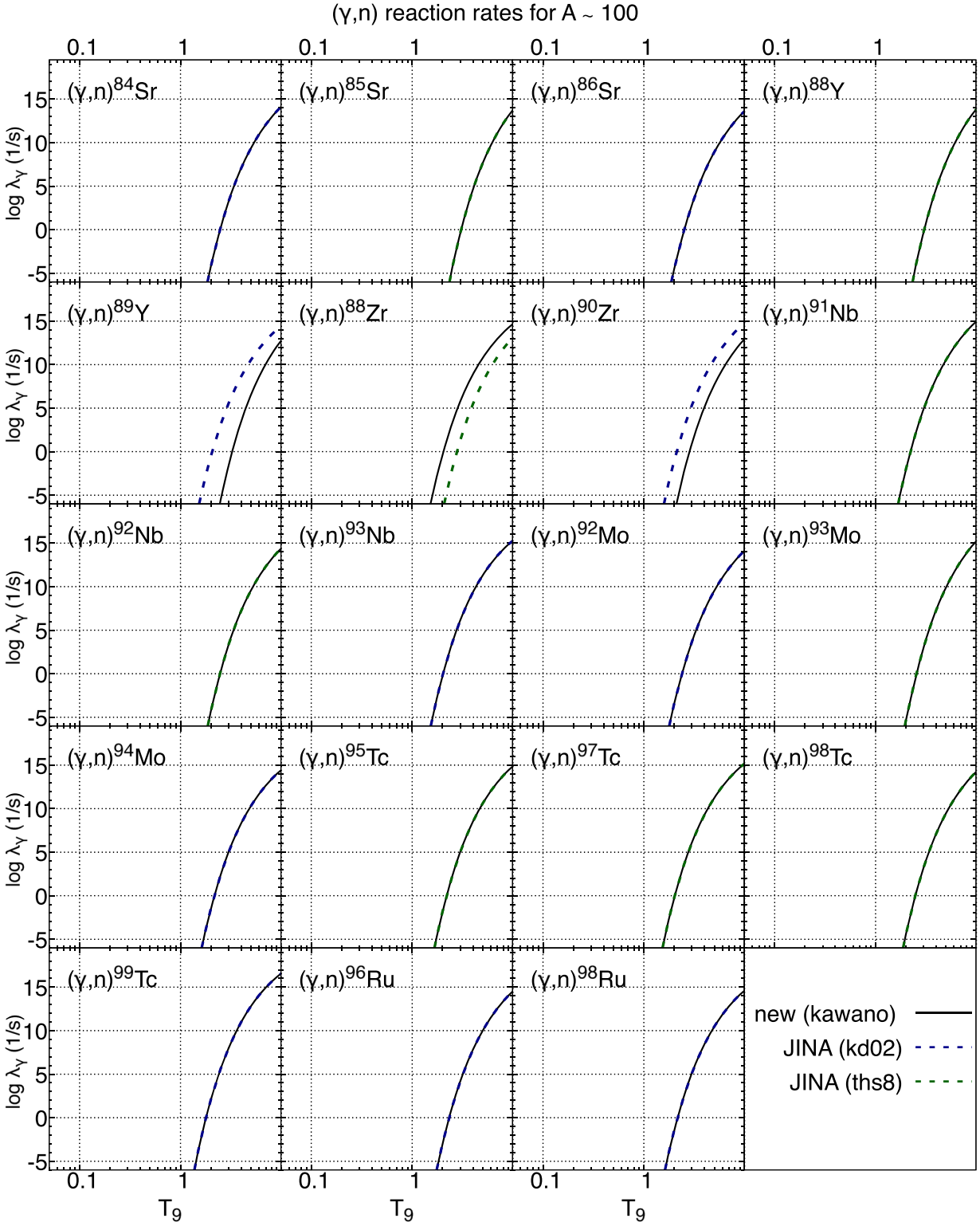

Figure 19. Inverse (γ, n) reaction rates.

Table 8
Cross Sections for the Main Neutrino-induced Reaction via NC for ^{93}Nb, ^{99}Ru, ^{139}La, and ^{181}Ta

E_ν	NC Cross Section, σ (cm^2)			
(MeV)	^{93}Nb (ν, $\nu'n$)^{92} Nb	^{93}Nb (ν, $\nu'p$)^{92} Zr	^{93}Nb ($\bar{\nu}$, $\bar{\nu}'n$)^{92} Nb	^{93}Nb ($\bar{\nu}$, $\bar{\nu}'p$)^{92} Zr
0	0.00000000E-00	0.00000000E-00	0.00000000E-00	0.00000000E-00
8	2.50713618E-50	4.36590897E-50	7.75514966E-50	1.35047621E-49
16	6.41702589E-42	1.42274917E-43	5.31736472E-42	1.18398366E-43
24	1.19460781E-41	2.61691966E-42	9.26003709E-42	2.02888823E-42
32	1.11618046E-41	4.05216387E-42	8.10204807E-42	2.94138929E-42
40	1.15439623E-41	4.77290399E-42	7.85088848E-42	3.24604476E-42
48	1.41992964E-41	6.22778850E-42	9.12788654E-42	4.00355303E-42
56	1.44336157E-41	6.65086093E-42	8.87325346E-42	4.08876745E-42
64	1.40070286E-41	6.61187328E-42	8.33028829E-42	3.93230587E-42
72	1.48701381E-41	7.07143664E-42	8.65991005E-42	4.11826341E-42
80	1.45054088E-41	7.02562041E-42	8.34253207E-42	4.04075106E-42
…	^{99}Ru (ν, $\nu'n$)^{98} Ru	^{99}Ru (ν, $\nu'p$)^{98} Tc	^{99}Ru ($\bar{\nu}$, $\bar{\nu}'n$)^{98} Ru	^{99}Ru ($\bar{\nu}$, $\bar{\nu}'p$)^{98} Tc
0	0.00000000E-00	0.00000000E-00	0.00000000E-00	0.00000000E-00
8	8.31938546E-48	3.44319491E-43	7.85612776E-48	0.00000000E+00
16	3.21807831E-41	3.62001976E-42	2.88619734E-41	5.68020612E-43
24	2.34930998E-41	6.96046308E-42	2.00095035E-41	2.93190765E-42
32	2.56998078E-41	5.52408294E-42	2.07665520E-41	5.41904121E-42
40	2.14218934E-41	2.84717287E-42	1.64510701E-41	5.27353169E-42
48	2.48543962E-41	1.94343549E-42	1.82246833E-41	5.98999512E-42
56	2.30132053E-41	1.20297515E-42	1.61746490E-41	5.75926394E-42
64	2.12816045E-41	7.36653543E-43	1.43831447E-41	5.24028336E-42
72	2.31177290E-41	5.51800694E-43	1.50636782E-41	5.64197366E-42
80	2.37025986E-41	3.87751776E-43	1.49177096E-41	5.54453176E-42
…	^{139}La (ν, $\nu'n$)^{138} La	^{139}La (ν, $\nu'p$)^{138} Ba	^{139}La ($\bar{\nu}$, $\bar{\nu}'n$)^{138} La	^{139}La ($\bar{\nu}$, $\bar{\nu}'p$)^{138} Ba
0	0.00000000E-00	0.00000000E-00	0.00000000E-00	0.00000000E-00
8	1.14328551E-58	0.00000000E+00	1.35047621E-49	7.75514966E-50
16	5.26640495E-44	2.40232318E-41	1.18398366E-43	5.31736472E-42
24	5.29198208E-42	9.23905206E-42	2.02888823E-42	9.26003709E-42
32	1.46484515E-41	1.22319044E-41	2.94138929E-42	8.10204807E-42
40	2.24460135E-41	1.55437490E-41	3.24604476E-42	7.85088848E-42
48	2.18293273E-41	1.26069097E-41	4.00355303E-42	9.12788654E-42
56	1.95624622E-41	1.06066696E-41	4.08876745E-42	8.87325346E-42
64	2.42966931E-41	1.31735886E-41	3.93230587E-42	8.33028829E-42
72	2.16489860E-41	1.11070692E-41	4.11826341E-42	8.65991005E-42
80	2.05087962E-41	1.03754018E-41	4.04075106E-42	8.34253207E-42
…	^{181}Ta (ν, $\nu'n$)^{180} Ta	^{181}Ta (ν, $\nu'p$)^{180} Hf	^{181}Ta ($\bar{\nu}$, $\bar{\nu}'n$)^{180} Ta	^{181}Ta ($\bar{\nu}$, $\bar{\nu}'p$)^{180} Hf
0	0.00000000E-00	0.00000000E-00	0.00000000E-00	0.00000000E-00
8	7.12415025E-50	8.74129047E-44	8.10389589E-50	8.17122116E-44
16	2.93958839E-45	2.68586946E-42	2.90647665E-45	2.65112708E-42
24	3.67968942E-43	4.51747170E-42	3.71060172E-43	4.56012162E-42
32	1.24984216E-42	6.89812693E-42	1.27083830E-42	7.01667485E-42
40	2.56869094E-42	1.11448222E-41	2.60570403E-42	1.13044001E-41
48	3.59301912E-42	1.31187144E-41	3.56647425E-42	1.30218781E-41
56	4.82760384E-42	1.67583423E-41	4.66951437E-42	1.62094060E-41
64	6.25367586E-42	2.06427678E-41	5.83161284E-42	1.92500015E-41
72	7.63247112E-42	2.47097518E-41	6.80911481E-42	2.20436351E-41
80	8.76210673E-42	2.85776514E-41	7.44981200E-42	2.42971224E-41

Table 9
Cross Sections for the Main Neutrino-induced Reaction via CC for ^{92}Nb, ^{98}Mo, ^{99}Ru, ^{100}Ru, ^{138}Ba, and ^{180}Hf

E_ν	CC Cross Section, σ (cm^2)				
(MeV)	^{92}Zr (ν_e, e^-)^{92} Nb	^{92}Zr (ν_e, e^-p)^{92} Zr	^{92}Zr (ν_e, e^-n)^{91} Nb		
0	0.00000000E+00	0.00000000E+00	0.00000000E+00		
8	1.09959219E-42	5.47587107E-43	5.20403126E-45		
16	2.25014331E-41	1.22824926E-41	1.25064181E-42		
24	1.08407931E-40	6.67298484E-42	5.58604016E-42		
32	2.78249619E-40	4.84525629E-42	5.62397084E-42		
40	5.38772348E-40	6.14584557E-42	7.85259869E-42		
48	8.21131516E-40	5.50500721E-42	7.89996859E-42		
56	9.73133433E-40	4.18051021E-42	6.48922060E-42		
64	1.18909971E-39	5.58049470E-42	8.66302950E-42		
72	1.51267048E-39	5.48536212E-42	8.56701524E-42		
80	1.85697485E-39	5.75426202E-42	9.00574682E-42		
…	^{98}Mo (ν_e, e^-)^{98} Tc	^{98}Mo (ν_e, e^-p)^{97} Mo	^{98}Mo (ν_e, e^-n)^{97} Tc	^{99}Ru ($\bar{\nu}_e$, e^+n)^{98} Tc	^{100}Ru ($\bar{\nu}_e$, e^+2n)^{98} Tc
0	0.00000000E+00	0.00000000E+00	0.00000000E+00	0.00000000E+00	0.00000000E+00
8	7.70989088E-43	7.70989088E-43	0.00000000E+00	2.22690899E-41	7.43796701E-52
16	1.73568589E-41	1.73568589E-41	1.27629938E-43	6.48833284E-40	2.09369501E-43
24	1.02710369E-40	1.02710369E-40	1.71459340E-42	1.21296066E-41	8.24406827E-41
32	2.85652085E-40	2.85652085E-40	2.37034880E-42	1.00332160E-42	1.13478523E-41
40	5.75412528E-40	5.75412528E-40	2.72131091E-42	3.49011336E-44	6.81952771E-43
48	9.10315416E-40	9.10315416E-40	4.04495970E-42	1.44088642E-45	4.85493147E-44
56	1.15041308E-39	1.15041308E-39	3.96748000E-42	6.64842557E-47	2.51775430E-45
64	1.30393579E-39	1.30393579E-39	3.67176526E-42	2.93322999E-48	1.42313551E-46
72	1.66758950E-39	1.66758950E-39	4.63981404E-42	1.77322096E-49	9.88014554E-48
80	2.05845775E-39	2.05845775E-39	5.32473753E-42	1.06916477E-49	7.77608897E-49
…	^{138}Ba (ν_e, e^-)^{138} La	^{138}Ba (ν_e, e^-p)^{137} Ba	^{138}Ba (ν_e, e^-n)^{137} La		
0	0.00000000E+00	0.00000000E+00	0.00000000E+00		
8	7.35496305E-42	1.94262799E-42	6.62576330E-51		
16	9.87540687E-41	9.53163886E-41	3.97731716E-43		
24	3.98835084E-40	2.27041114E-41	1.53258451E-41		
32	1.01378882E-39	1.66143076E-41	1.92037893E-41		
40	1.89565025E-39	2.11978177E-41	2.56088381E-41		
48	2.99592402E-39	1.83284468E-41	2.56488809E-41		
56	4.27490906E-39	1.73415784E-41	2.45188862E-41		
64	5.70163925E-39	2.50252082E-41	3.53790143E-41		
72	7.25025285E-39	2.42380089E-41	3.52754018E-41		
80	8.89389789E-39	2.57475634E-41	3.75243103E-41		
…	^{180}Hf (ν_e, e^-)^{180} Ta	^{180}Hf (ν_e, e^-p)^{179} Hf	^{180}Hf (ν_e, e^-n)^{179} Ta		
0	0.00000000E+00	0.00000000E+00	0.00000000E+00		
8	7.75463639E-42	7.44290806E-42	1.84915780E-51		
16	8.82760000E-41	5.14914969E-41	3.63902374E-44		
24	4.13377695E-40	4.43942334E-41	2.95886195E-42		
32	1.31540943E-39	5.11056133E-41	8.45900752E-42		
40	2.63588344E-39	6.00408430E-41	1.18186695E-41		
48	4.22215839E-39	6.19622075E-41	1.41993471E-41		
56	5.96889593E-39	8.04424856E-41	1.88733180E-41		
64	7.81247822E-39	9.66390861E-41	2.26243506E-41		
72	9.71554309E-39	1.09833483E-40	2.61080109E-41		
80	1.16463985E-38	1.29155821E-40	3.11110419E-41		

Appendix D
Main Reactions of Nuclei in the ν-process

We tabulate the main reactions for the production of the nuclides ^{7}Be, ^{7}Li, ^{11}B, ^{11}C, ^{92}Nb, ^{98}Tc, ^{138}La, and ^{180}Ta at Table 10, where the results are obtained for NH using the KCK19 hydrodynamics at $M_r = 2.63$, 3.25, 3.98, and 4.93 $M_\odot$, respectively. The reactions shown in this table contribute to the final yields by more than about 3% of their main production reactions.

Also, we visualize all the main reactions relevant to these elements as histograms in Figures 20, 21, 22, 23, 24, 25, 26, and 27, respectively. The left and right sides of the figures are the production and destruction reactions, respectively, for the element synthesis. These histograms could be very useful for grasping the contributions of the main nuclear reactions, as well as those of the neutrino-induced reactions.

Table 10
Main Nuclear Reactions at Each Mass Coordinate for the Nuclei Considered in This Work

	The Main Production Reactions in the NH Case			
$M_r/M_\odot$	2.63	3.25	3.98	4.93
^{7}Li	^{12}C + $\bar{\nu}_e$ ^{12}C + ν	^{12}C + $\bar{\nu}_e$ ^{12}C + ν	^{4}He (t, γ)^{7} Li ^{7}Be (n, p)^{7} Li	^{4}He (t, γ)^{7} Li
^{7}Be	^{12}C + ν ^{12}C + ν_e ^{10}B (p, α)^{7} Be	^{12}C + ν ^{12}C + ν_e ^{10}B (p, α) Be	^{3}He (α, γ)^{7} Be	^{3}He (α, γ)^{7} Be
^{11}B	^{12}C + ν ^{12}C + $\bar{\nu}_e$	^{12}C + ν ^{12}C + $\bar{\nu}_e$	^{7}Li (α, γ)^{11} B ^{11}C (n, p)^{11} B ^{12}C + ν	^{7}Li (α, γ)^{11} B ^{12}C + ν
^{11}C	^{12}C + ν ^{12}N (γ, p)^{11} C ^{12}C + ν_e	^{12}C + ν ^{12}N (γ, p)^{11} C ^{12}C + ν_e	^{7}Be (α, γ)^{11} C ^{12}C + ν_e ^{12}C + ν	^{12}C + ν_e ^{12}C + ν
^{92}Nb	^{92}Zr (ν_e, e^-)^{92} Nb	^{92}Zr (ν_e, e^-)^{92} Nb	^{92}Zr (ν_e, e^-)^{92} Nb	^{92}Zr (ν_e, e^-)^{92} Nb
^{98}Tc	^{98}Mo (ν_e, e^-)^{98} Tc ^{100}Ru ($\bar{\nu}_e$, e^+2n)^{98} Tc	^{98}Mo (ν_e, e^-)^{98} Tc ^{100}Ru ($\bar{\nu}_e$, e^+2n)^{98} Tc	^{97}Tc (n, γ)^{98} Tc ^{98}Mo (ν_e, e^-)^{98} Tc ^{99}Ru ($\bar{\nu}_e$, e^+n)^{98} Tc	^{97}Tc (n, γ)^{98} Tc ^{98}Mo (ν_e, e^-)^{98} Tc ^{99}Ru ($\bar{\nu}_e$, e^+n)^{98} Tc
^{138}La	^{138}Ba (ν_e, e^-)^{138} La	^{138}Ba (ν_e, e^-)^{138} La	^{138}Ba (ν_e, e^-)^{138} La	^{138}Ba (ν_e, e^-)^{138} La
^{180}Ta	^{179}Ta (n, γ)^{180} Ta ^{180}Hf (ν_e, e^-)^{180} Ta	^{179}Ta (n, γ)^{180} Ta ^{180}Hf (ν_e, e^-)^{180} Ta	^{180}Hf (ν_e, e^-)^{180} Ta	^{180}Hf (ν_e, e^-)^{180} Ta

Note. These are deduced from the integration of the respective reaction rates over time to $t \sim 50$ s. The detailed reactions of ^{12}C + ν_e for ^{11}C and ^{7}Be are shown in Table 3.

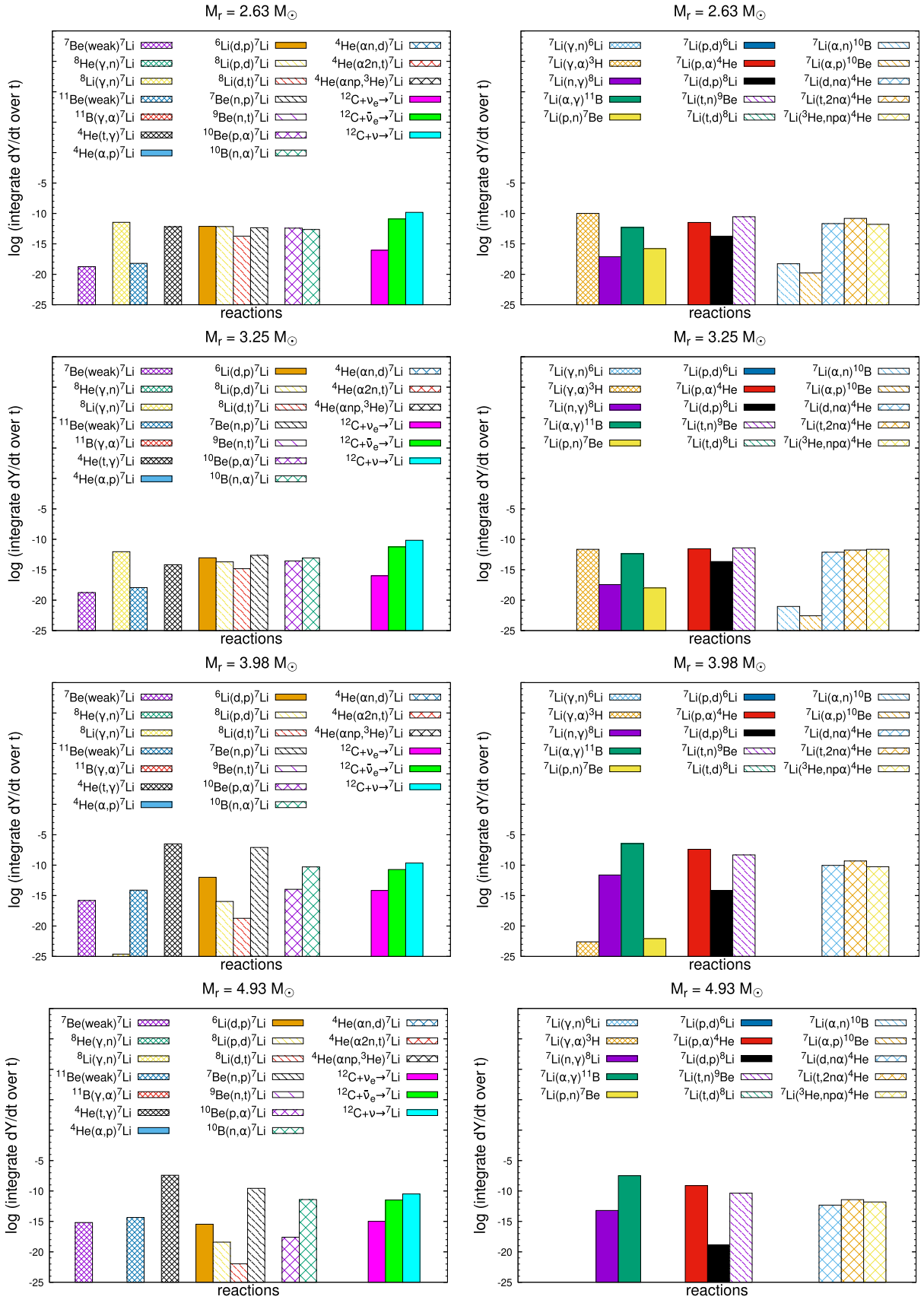

Figure 20. The main nuclear reactions for ^{7}Li. "Weak" means the channels of the weak interaction, such as beta decays and electron captures. The histograms of some nuclear reactions below a limit are not shown.

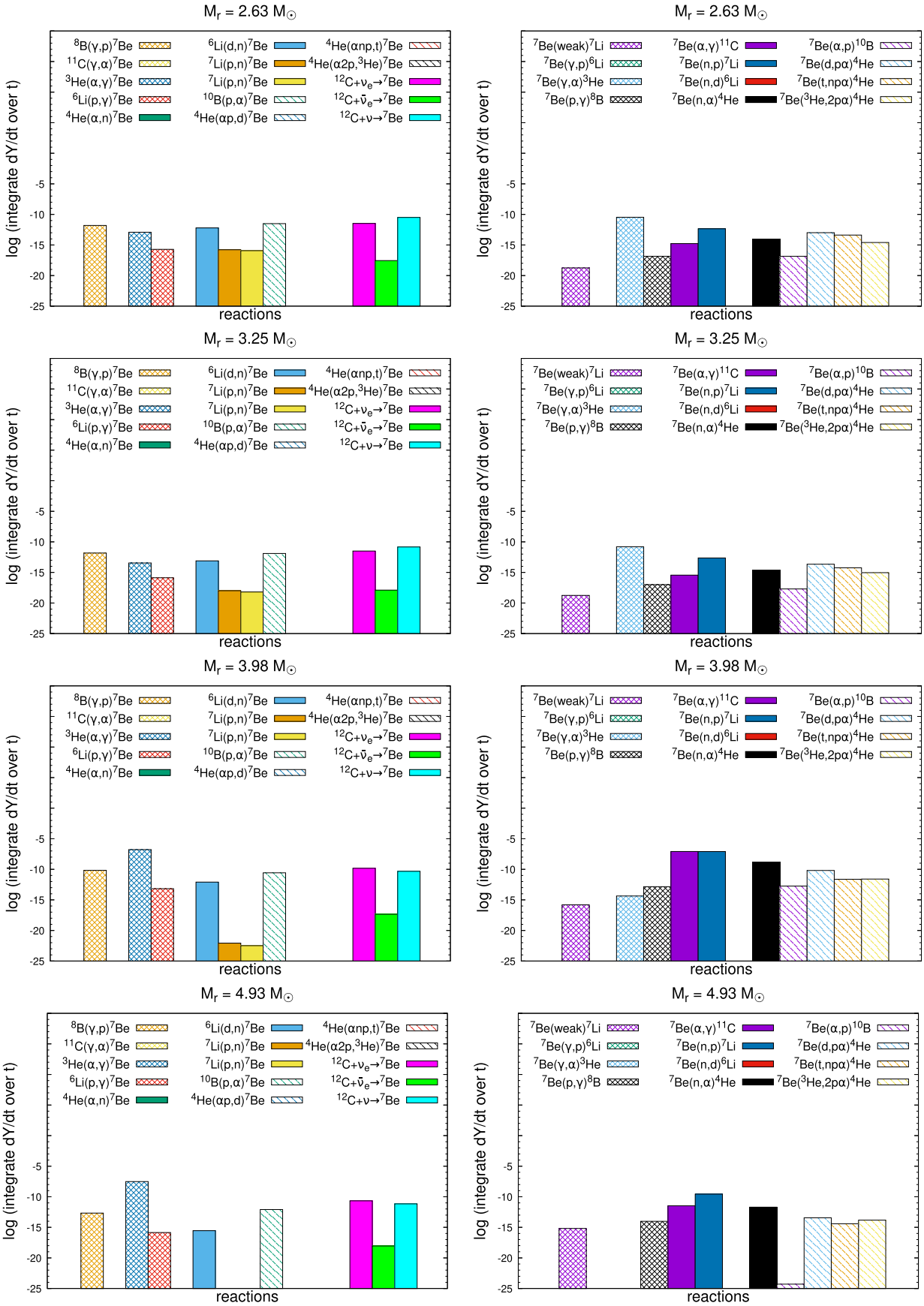

Figure 21. The same as Figure 20, but for ^{7}Be.

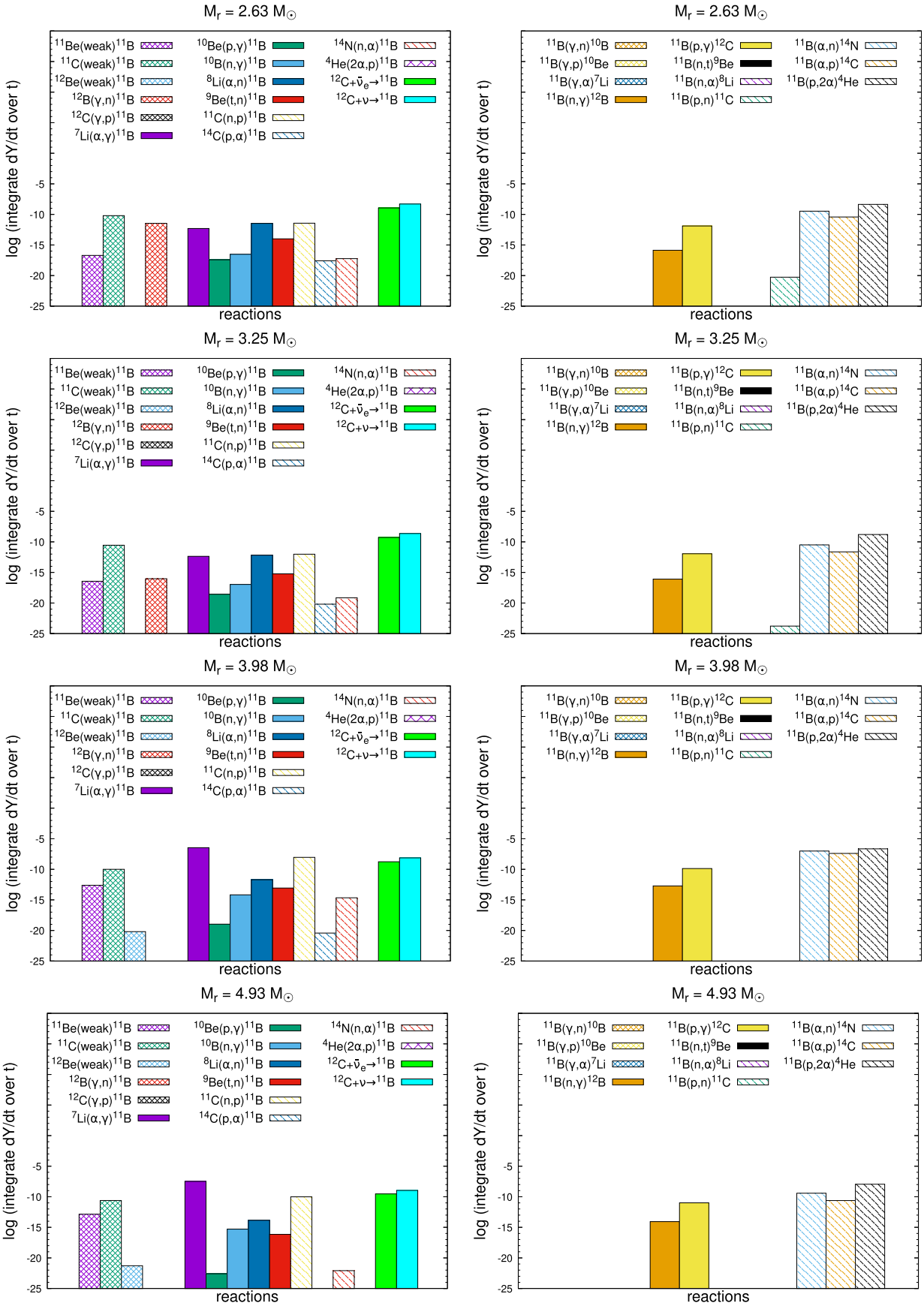

Figure 22. The same as Figure 20, but for ^{11}B.

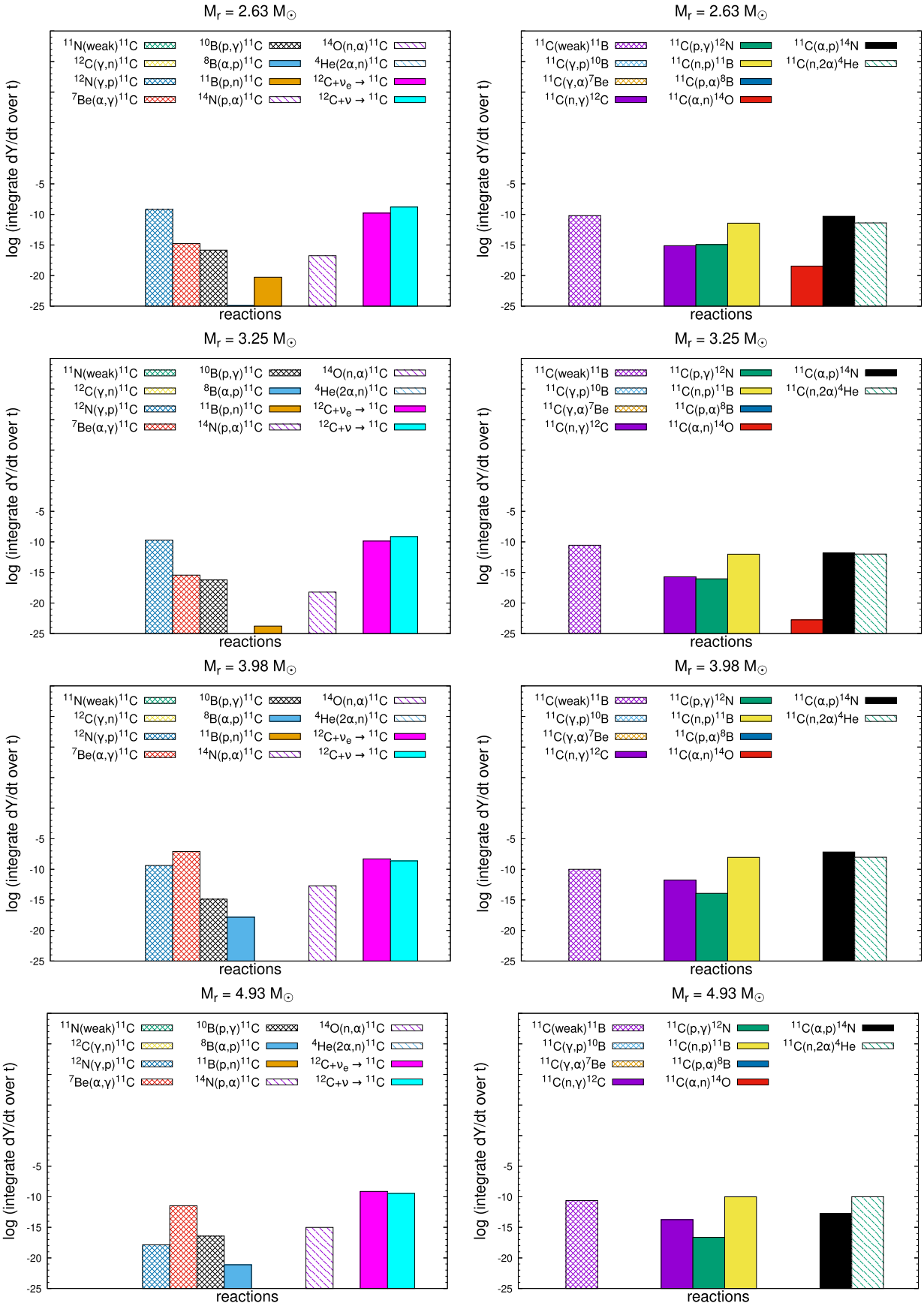

Figure 23. The same as Figure 20, but for ^{11}C.

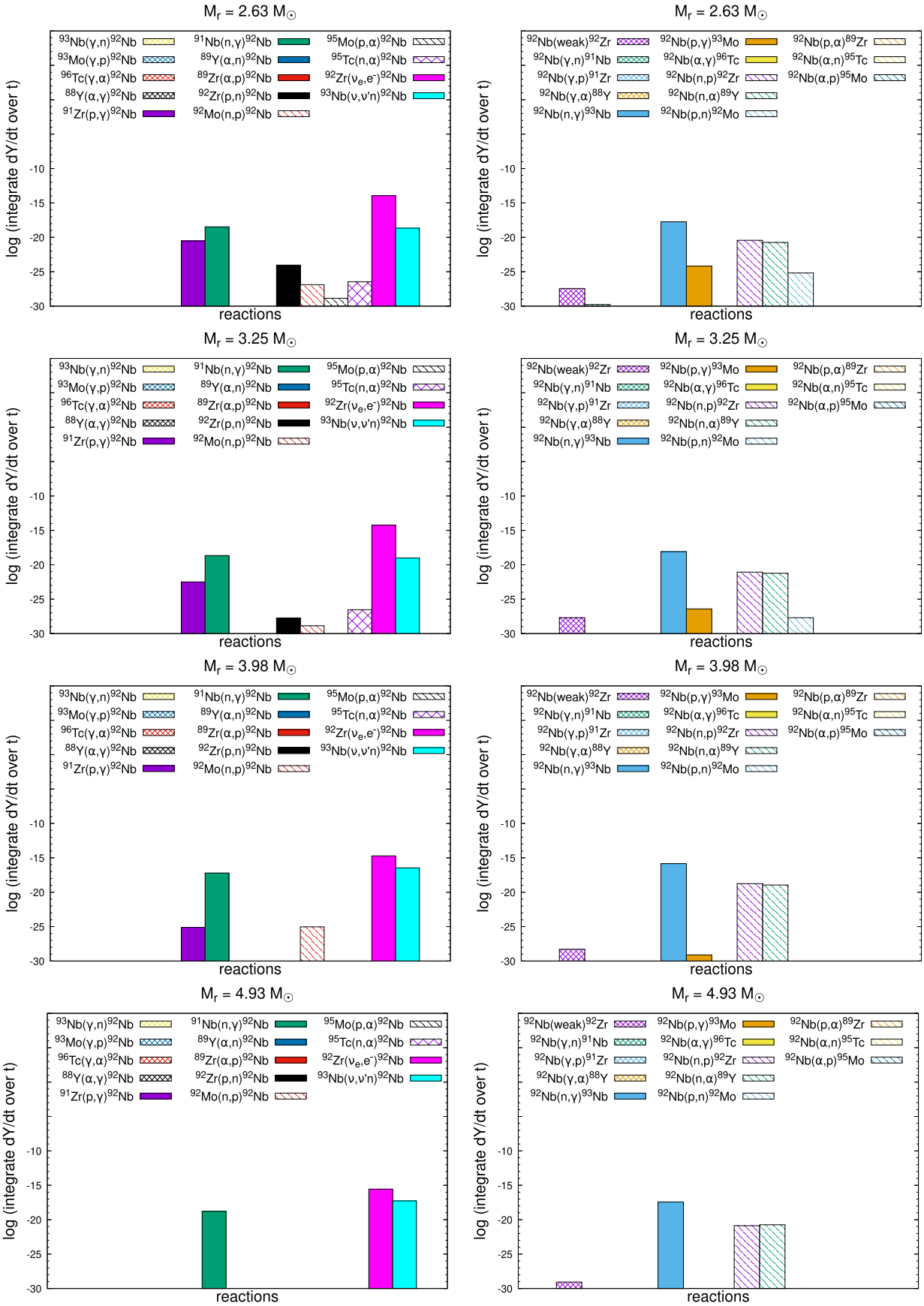

Figure 24. The same as Figure 20, but for ^{92}Nb.

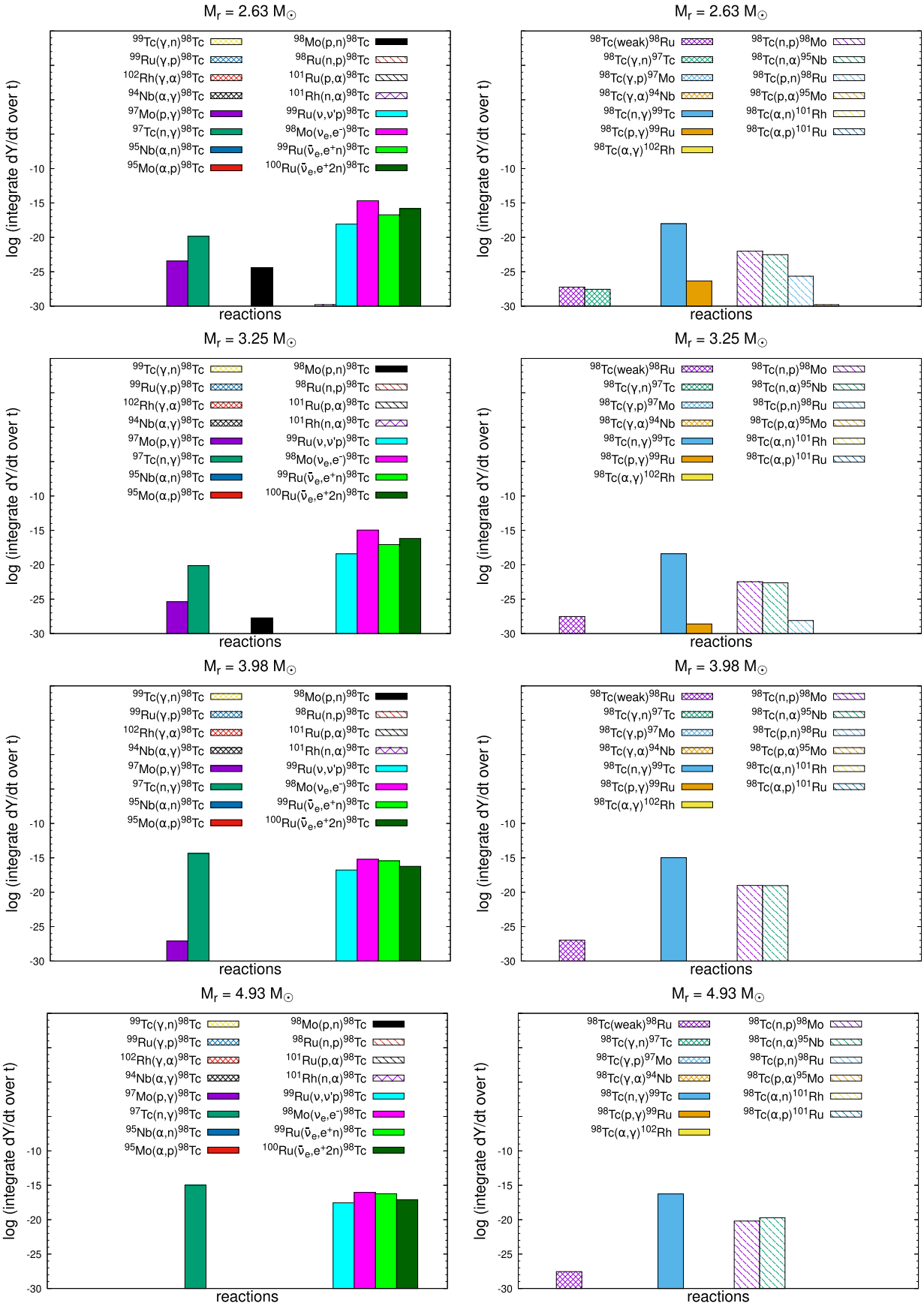

Figure 25. The same as Figure 20, but for ^{98}Tc.

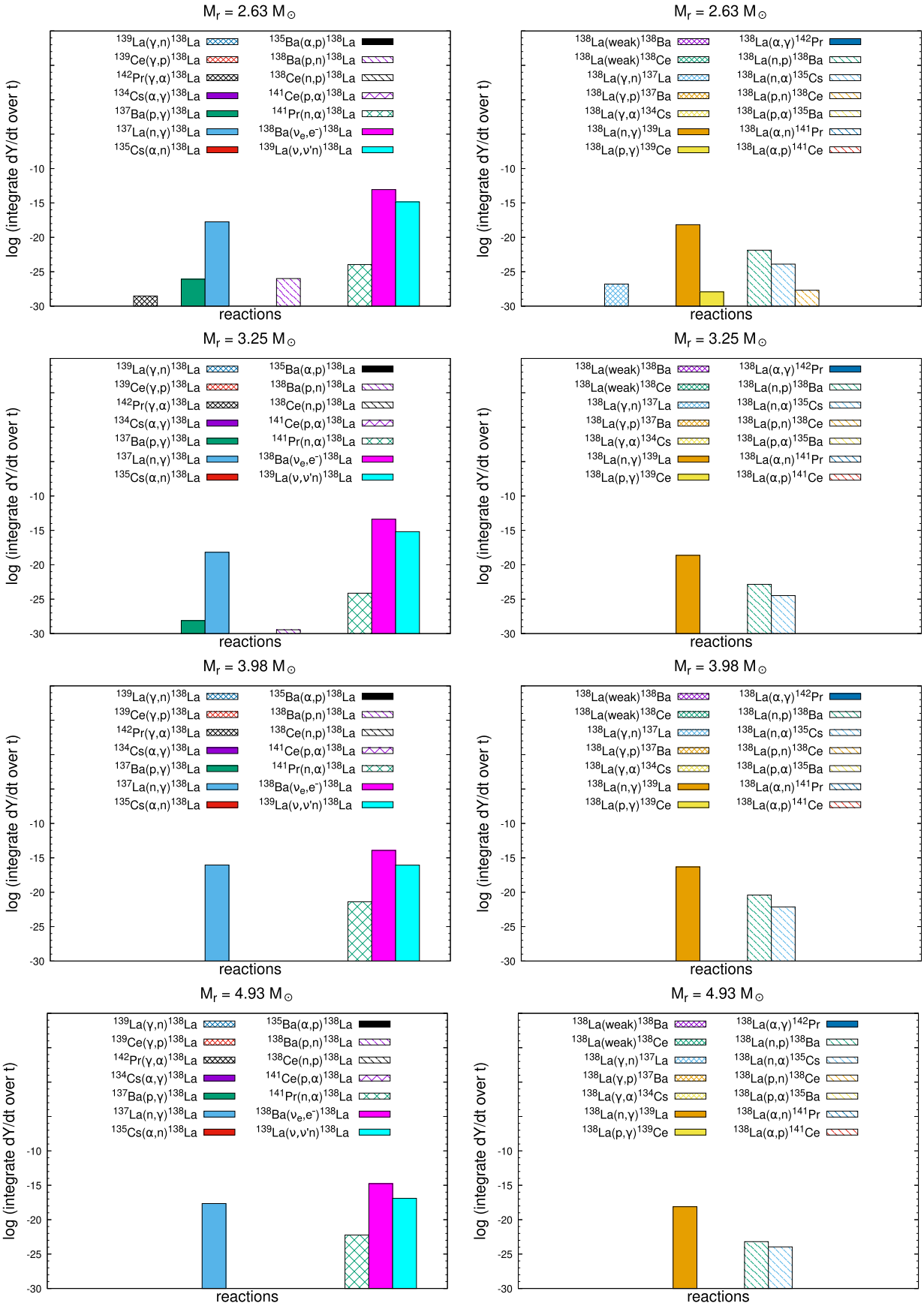

Figure 26. The same as Figure 20, but for ^{138}La.

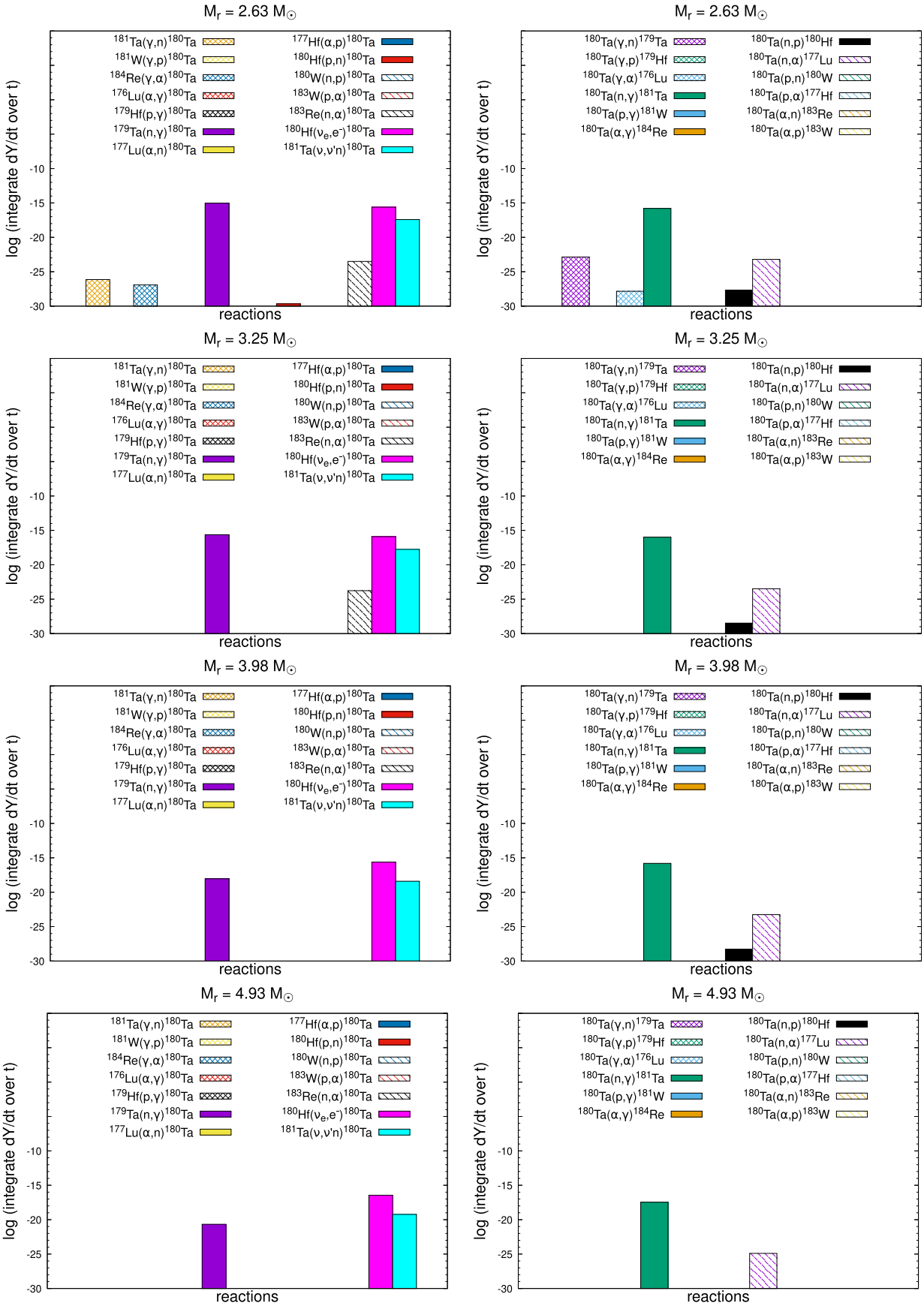

Figure 27. The same as Figure 20, but for ^{180}Ta.

Appendix E
PFs Normalized by Different Stable Nuclei

Here, we present the PFs of ^{7}Li, ^{11}B, ^{138}La, and ^{180}Ta, normalized to ^{16}O, ^{24}Mg, and ^{28}Si, respectively. See the details in Section 5.5.

Table 11
The PF Normalized to ^{16}O

		The PF $10^{[i/^{16}O]}$ in the Region M_r = 1.6–6 $M_\odot$			
	MH	i = ^{7}Li	^{11}B	^{138}La	^{180}Ta
FD EQ	NH	2.90×10^{-1}	7.72×10^{-1}	9.9×10^{-2}	3.037
(HKC18)	IH	1.38×10^{-1}	8.46×10^{-1}	9.6×10^{-2}	3.028
FD EQ	NH	1.42×10^{-1}	4.33×10^{-1}	1.02×10^{-1}	3.379
(KCK19)	IH	8.4×10^{-2}	3.73×10^{-1}	0.93×10^{-1}	3.366
FD EQ Shock	NH	1.20×10^{-1}	3.98×10^{-1}	1.13×10^{-1}	3.382
(KCK19)	IH	8.5×10^{-2}	3.62×10^{-1}	9.4×10^{-2}	3.366
SI EQ[a]	NH	1.42×10^{-1}	4.33×10^{-1}	1.02×10^{-1}	3.379
(KCK19)	IH	1.28×10^{-1}	6.29×10^{-1}	3.67×10^{-1}	3.493
SI NEQ	NH	1.18×10^{-1}	8.60×10^{-1}	4.11×10^{-1}	4.293
(KCK19)	IH	1.06×10^{-1}	8.32×10^{-1}	3.06×10^{-1}	4.250
FD NEQ	NH	1.00×10^{-1}	9.97×10^{-1}	6.25×10^{-1}	4.386
(KCK19)	IH	1.41×10^{-1}	9.83×10^{-1}	6.47×10^{-1}	4.412
SI NEQ Ko et al. (2020)	NH	2.33×10^{-1}	1.564	4.18×10^{-1}	4.890
(HKC18)	IH	1.94×10^{-1}	1.603	3.04×10^{-1}	4.872
FD NEQ Ko et al. (2020)	NH	1.99×10^{-1}	1.975	6.61×10^{-1}	4.840
(HKC18)	IH	3.22×10^{-1}	1.636	6.71×10^{-1}	4.854

Note.
[a] The same as the FD EQ (KCK19) NH result.

Table 12
The PF Normalized to ^{24}Mg

		The PF $10^{[i/^{24}Mg]}$ in the Region M_r = 1.6–6 $M_\odot$			
	MH	i = ^{7}Li	^{11}B	^{138}La	^{180}Ta
FD EQ	NH	4.20×10^{-1}	1.116	1.44×10^{-1}	4.392
(HKC18)	IH	2.00×10^{-1}	1.224	1.38×10^{-1}	4.379
FD EQ	NH	1.92×10^{-1}	5.84×10^{-1}	1.37×10^{-1}	4.560
(KCK19)	IH	1.14×10^{-1}	5.04×10^{-1}	1.26×10^{-1}	4.542
FD EQ Shock	NH	1.61×10^{-1}	5.37×10^{-1}	1.52×10^{-1}	4.565
(KCK19)	IH	1.15×10^{-1}	4.88×10^{-1}	1.27×10^{-1}	4.542
SI EQ[a]	NH	1.92×10^{-1}	5.84×10^{-1}	1.37×10^{-1}	4.560
(KCK19)	IH	1.74×10^{-1}	8.51×10^{-1}	4.97×10^{-1}	4.726
SI NEQ	NH	1.60×10^{-1}	1.163	5.56×10^{-1}	5.810
(KCK19)	IH	1.44×10^{-1}	1.127	4.14×10^{-1}	5.751
FD NEQ	NH	1.36×10^{-1}	1.349	8.46×10^{-1}	5.935
(KCK19)	IH	1.91×10^{-1}	1.330	8.76×10^{-1}	5.971
SI NEQ Ko et al. (2020)	NH	3.54×10^{-1}	2.378	6.35×10^{-1}	7.437
(HKC18)	IH	2.96×10^{-1}	2.437	4.63×10^{-1}	7.410
	NH	3.02×10^{-1}	3.004	1.006	7.361

Table 12
(Continued)

		The PF $10^{[i/^{24}Mg]}$ in the Region M_r = 1.6–6 $M_\odot$			
	MH	i = ^{7}Li	^{11}B	^{138}La	^{180}Ta
FD NEQ Ko et al. (2020)					
(HKC18)	IH	0.49×10^{-1}	2.489	1.020	7.383

Note.
[a] The same as the FD EQ (KCK19) NH result.

Table 13
The PF Normalized to ^{28}Si

		The PF $10^{[i/^{28}Si]}$ in the Region M_r = 1.6–6 $M_\odot$			
	MH	i = ^{7}Li	^{11}B	^{138}La	^{180}Ta
FD EQ	NH	3.49×10^{-1}	0.929×10^{-1}	1.20×10^{-1}	3.657
(HKC18)	IH	1.66×10^{-1}	1.019	1.15×10^{-1}	3.647
FD EQ	NH	5.53×10^{-1}	1.681	3.96×10^{-1}	13.125
(KCK19)	IH	3.28×10^{-1}	1.449	3.62×10^{-1}	13.074
FD EQ Shock	NH	4.65×10^{-1}	1.546	4.38×10^{-1}	13.138
(KCK19)	IH	3.32×10^{-1}	1.405	3.67×10^{-1}	13.074
SI EQ[a]	NH	5.53×10^{-1}	1.681	3.96×10^{-1}	13.125
(KCK19)	IH	5.00×10^{-1}	2.448	1.429	13.603
SI NEQ	NH	4.59×10^{-1}	3.348	1.599	16.721
(KCK19)	IH	4.15×10^{-1}	3.242	1.191	16.553
FD NEQ	NH	3.91×10^{-1}	3.883	2.436	17.082
(KCK19)	IH	5.48×10^{-1}	3.827	2.520	17.186
SI NEQ Ko et al. (2020)	NH	2.91×10^{-1}	1.952	5.21×10^{-1}	6.103
(HKC18)	IH	2.43×10^{-1}	2.000	3.80×10^{-1}	6.080
FD NEQ Ko et al. (2020)	NH	2.48×10^{-1}	2.465	8.25×10^{-1}	6.404
(HKC18)	IH	4.02×10^{-1}	2.042	8.37×10^{-1}	6.058

Note.
[a] The same as the FD EQ (KCK19) NH result.

ORCID iDs

Dukjae Jang https://orcid.org/0000-0001-7684-9519
Myung-Ki Cheoun https://orcid.org/0000-0001-7810-5134
Motohiko Kusakabe https://orcid.org/0000-0003-3083-6565
Toshitaka Kajino https://orcid.org/0000-0002-8619-359X
Masaomi Ono https://orcid.org/0000-0002-0603-918X
Grant J. Mathews https://orcid.org/0000-0002-2663-0540

References

Abbar, S., Duan, H., Sumiyoshi, K., et al. 2019, PhRvD, 100, 043004
Aglietta, M., Badino, G., Bologna, G., et al. 1987, EL, 3, 1315
Angulo, C., Arnould, M., Rayet, M., et al. 1999, NuPhA, 656, 3
Austin, S. M., Heger, A., & Tur, C. 2011, PhRvL, 106, 152501

Banerjee, A., Dighe, A., & Raffelt, G. 2011, PhRvD, 84, 053013
Bionta, R. M., Blewitt, G., Bratton, C. B., et al. 1987, PhRvL, 58, 1494
Blinnikov, S., Lundqvist, P., Bartunov, O., et al. 2000, ApJ, 532, 1132
Burbidge, E. M., Burbidge, G. R., Fowler, W. A., et al. 1957, RvMP, 29, 547
Byelikov, A., Adachi, T., Fujita, H., et al. 2007, PhRvL, 98, 082501
Chakraborty, S., Fischer, T., Mirizzi, A., et al. 2011, PhRvL, 107, 151101
Chakraborty, S., Fischer, T., Mirizzi, A., et al. 2011, PhRvD, 84, 025002
Chakraborty, S., & Mirizzi, A. 2014, PhRvD, 90, 033004
Cheoun, M.-K., Ha, E., Lee, S. Y., et al. 2010, PhRvC, 81, 028501
Cheoun, M.-K., Ha, E., Hayakawa, T., et al. 2010, PhRvC, 82, 035504
Cheoun, M.-K., Ha, E., Hayakawa, T., et al. 2012, PhRvC, 85, 065807
Cheoun, M.-K., Ha, E., Kim, K. S., et al. 2010, JPhG, 37, 055101
Cyburt, R. H., Amthor, A. M., Ferguson, R., et al. 2010, ApJS, 189, 240
Dasgupta, B., Dighe, A., Mirizzi, A., et al. 2008, PhRvD, 78, 033014
Dasgupta, B., Mirizzi, A., Tamborra, I., et al. 2010, PhRvD, 81, 093008
Dasgupta, B., Mirizzi, A., & Sen, M. 2017, JCAP, 2017, 019
Dighe, A. S., & Smirnov, A. Y. 2000, PhRvD, 62, 033007
Duan, H., Friedland, A., McLaughlin, G. C., et al. 2011, JPhG, 38, 035201
Duan, H., Fuller, G. M., Carlson, J., et al. 2006, PhRvD, 74, 105014
Duan, H., & Friedland, A. 2011, PhRvL, 106, 091101
Fields, B. D., Olive, K. A., Vangioni-Flam, E., et al. 2000, ApJ, 540, 930
Fischer, T., Whitehouse, S. C., Mezzacappa, A., et al. 2010, A&A, 517, A80
Fogli, G. L., Lisi, E., Mirizzi, A., et al. 2003, PhRvD, 68, 033005
Fuller, G. M., & Qian, Y.-Z. 2006, PhRvD, 73, 023004
Glas, R., Janka, H.-T., Capozzi, F., et al. 2020, PhRvD, 101, 063001
Giunti, C., & Chung, W. K. 2007, in Fundamentals of Neutrino Physics and Astrophysics, ed. C. Giunti & W. K. Chung (Oxford: Oxford Univ. Press), 2007
Haba, M. K., Lai, Y.-J., Wotzlaw, J.-F., et al. 2021, PNAS, 118, 2017750118
Harper, C. L. 1996, ApJ, 466, 437
Hashimoto, M. 1995, PThPh, 94, 663
Hayakawa, T., Kajino, T., Chiba, S., et al. 2010, PhRvC, 81, 052801
Hayakawa, T., Ko, H., Cheoun, M.-K., et al. 2018, PhRvL, 121, 102701
Hayakawa, T., Nakamura, K., Kajino, T., et al. 2013, ApJL, 779, L9
Hayakawa, T., Shizuma, T., Kajino, T., et al. 2008, PhRvC, 77, 065802
Heger, A., Kolbe, E., Haxton, W. C., et al. 2005, PhLB, 606, 258
Heger, A., & Woosley, S. E. 2002, ApJ, 567, 532
Hirata, K., Kajita, T., Koshiba, M., et al. 1987, PhRvL, 58, 1490
Hoffmann, R. D., & Woosley, S. E. 1992, Stellar Nucleosynthesis Data, v92.1, http://dbserv.pnpi.spb.ru/elbib/tablisot/toi98/www/astro/hw92_1.htm
Janka, H.-T. 2012, ARNPS, 62, 407
Janka, H.-T., Langanke, K., Marek, A., et al. 2007, PhR, 442, 38
Janka, H.-T. 2017, Handbook of Supernovae, 1575 (Berlin: Springer)
Kajino, T., Mathews, G. J., & Hayakawa, T. 2014, JPhG, 41, 044007
Kawano, T., Talou, P., Chadwick, M. B., & Watanabe, T. 2010, JNST, 47, 462
Keil, M. T., Raffelt, G. G., & Janka, H.-T. 2003, ApJ, 590, 971
Kheswa, B. V., Wiedeking, M., Giacoppo, F., et al. 2015, PhLB, 744, 268
Kikuchi, Y., Hashimoto, M.- A., Ono, M., et al. 2015, PTEP, 2015, 063E01
Ko, H., Cheoun, M.-K., Ha, E., et al. 2020, ApJL, 891, L24
Ko, H., Cheoun, M.-K., Kusakabe, M., et al. 2019, AcPPB, 50, 385
Ko, H., Jang, D., Kusakabe, M., et al. 2020, ApJ, 894, 99
Kostelecký, V. A., & Samuel, S. 1994, PhRvD, 49, 1740
Kuo, T. K., & Pantaleone, J. 1989, PhRvD, 39, 1930
Kusakabe, M., Cheoun, M.-K., Kim, K. S., et al. 2019, ApJ, 872, 164
Lahkar, N., Kalita, S., Duorah, H. L., et al. 2017, JApA, 38, 8
Liu, M.-C., Nittler, L. R., Alexander, C. M. O., et al. 2010, ApJL, 719, L99
Lodders, K., Palme, H., & Gail, H.-P. 2009, Landolt Börnstein, 4B, 712
Malatji, K. L., Wiedeking, M., Goriely, S., et al. 2019, PhLB, 791, 403
Mathews, G. J., Kajino, T., Aoki, W., et al. 2012, PhRvD, 85, 105023
Mikheev, S. P., & Smirnov, A. I. 1986, NCimC, 9, 17
Mirizzi, A., Tamborra, I., Janka, H.-T., et al. 2016, NCimR, 39, 1
Münker, C., Weyer, S., Mezger, K., et al. 2000, Sci, 289, 1538
Nagakura, H., Burrows, A., & Vartanyan, D. 2021, MNRAS, 506, 1462
Nakamura, K., Yoshida, T., Shigeyama, T., et al. 2010, ApJL, 718, L137
NOνA Collaboration, Adamson, P., Aliaga, L., et al. 2017, PhRvL, 118, 231801
Nötzold, D., & Raffelt, G. 1988, NuPhB, 307, 924
O'Connor, E., Bollig, R., Burrows, A., et al. 2018, JPhG, 45, 104001
Olive, K. A. & Particle Data Group 2014, ChPhC, 38, 090001
Olive, K. A., & Vangioni, E. 2019, MNRAS, 490, 4307
Pantaleone, J. 1992, PhLB, 287, 128
Pehlivan, Y., Balantekin, A. B., Kajino, T., et al. 2011, PhRvD, 84, 065008
Qian, Y.-Z., & Fuller, G. M. 1995, PhRvD, 51, 1479
Raffelt, G. G. 2001, ApJ, 561, 890
Raffelt, G. 2012, arXiv:1201.1637
Raffelt, G., Sarikas, S., Seixas, D., & de, S. 2013, PhRvL, 111, 091101
Rauscher, T., Dauphas, N., Dillmann, I., et al. 2013, RPPh, 76, 066201
Samuel, S. 1993, PhRvD, 48, 1462
Sanloup, C., Blichert-Toft, J., Télouk, P., et al. 2000, E&PSL, 184, 75
Sasaki, H., Kajino, T., Takiwaki, T., et al. 2017, PhRvD, 96, 043013
Schaeffer, R., Declais, Y., & Jullian, S. 1987, Natur, 330, 142
Shigeyama, T., & Nomoto, K. 1990, ApJ, 360, 242
Sieverding, A., Martínez-Pinedo, G., Huther, L., et al. 2018, ApJ, 865, 143
Sieverding, A., Langanke, K., Martínez-Pinedo, G., et al. 2019, ApJ, 876, 151
Sigl, G. 2017, Astroparticle Physics: Theory and Phenomenology (Reading, MA: Atlantis Press)
Sigl, G., & Raffelt, G. 1993, NuPhB, 406, 423
Silberberg, R., & Tsao, C. H. 1990, PhR, 191, 351
Suzuki, T., & Kajino, T. 2013, JPhG, 40, 083101
Tamborra, I., Hüdepohl, L., Raffelt, G. G., et al. 2017, ApJ, 839, 132
Volpe, C., Väänänen, D., & Espinoza, C. 2013, PhRvD, 87, 113010
Woosley, S. E. 1988, ApJ, 330, 218
Woosley, S. E., Hartmann, D. H., Hoffman, R. D., et al. 1990, ApJ, 356, 272
Wu, M.-R., Qian, Y.-Z., Martínez-Pinedo, G., et al. 2015, PhRvD, 91, 065016
Yoshida, T., Kajino, T., & Hartmann, D. H. 2005, PhRvL, 94, 231101
Yoshida, T., Kajino, T., Yokomakura, H., et al. 2006, PhRvL, 96, 091101
Yoshida, T., Suzuki, T., Chiba, S., et al. 2008, ApJ, 686, 448
Yoshida, T., Terasawa, M., Kajino, T., et al. 2004, ApJ, 600, 204